UNIVERSITY OF CALIFORNIA

RIVERSIDE

Posterior Visual Pathway Dysfunction in Two Animal Models of Multiple Sclerosis: Understanding Pathology for Regeneration and Repair

A Dissertation submitted in partial satisfaction
of the requirements for the degree of

Doctor of Philosophy

in

Bioengineering

by

Maria Sekyi

September 2019

Dissertation Committee:

Dr. Seema Tiwari-Woodruff, Chairperson
Dr. B. Hyle Park
Dr. Victor G. Rodgers

The Dissertation of Maria Sekyi is approved:

_____

_____

_____

Committee Chairperson

University of California, Riverside

Acknowledgements

I am immensely grateful to my supervisor Dr. Tiwari-Woodruff, for her guidance and support throughout my work and growth into a professional scientist. I am also grateful to my labmates: Kelley Atkinson, Hawra Karim, Andrew Lapato, Hana Yamate-Morgan, and Dr. Kelli Lauderdale as well as numerous undergraduate students for their scientific input, and significant experimental assistance throughout my PhD. I would also like to thank my committee members for their important insight to the research project as well as the guidance they have given me. Special thanks also, to my friends and family who have supported me throughout this journey.

This work was supported by the National Institutes of Health Grants NIH R01 NS081141-01A1 to STW, and NIH R01 DK015556 to JAK, National Multiple Sclerosis Society Grant NMSS RG 4853A3/2 and the NSF graduate research fellowship to MS under Grant No. DGE-1326120.

ABSTRACT OF THE DISSERTATION

Posterior Visual Pathway Dysfunction in Two Animal Models of Multiple Sclerosis: Understanding Pathology for Regeneration and Repair

by

Maria Sekyi

Doctor of Philosophy, Graduate Program in Bioengineering
University of California, Riverside, September 2019
Dr. Seema Tiwari-Woodruff, Chairperson

Visual dysfunction is pronounced in multiple sclerosis (MS) an autoimmune, demyelinating, neurodegenerative disease. To understand deficits in the visual pathway during MS a broader understanding of pathology and function across the visual system is needed. Here, afferent visual pathway pathology is first assessed in the most commonly used animal model of MS, experimental autoimmune encephalomyelitis (EAE). A remyelinating agent is then assessed for its therapeutic efficacy in attenuating visual pathway dysfunction. Although treatment results in robust remyelination across the visual pathway, severe axon damage remains and functional loss is not attenuated possibly due to treatment timing. The time course of posterior visual pathway pathology is then assessed in EAE in order to identify an ideal therapeutic window for remyelination, prior to irreversible axon damage and functional loss. The therapeutic window, corresponding to a period of significant demyelination but minimal axon damage, is found to occur after EAE onset, but prior to peak clinical disease. Visual pathway pathology is then assayed in

another animal model for MS, the cuprizone (CPZ) demyelination model, which induces CNS demyelination absent of a peripherally mediated immune response. Similar to EAE, visual pathway demyelination is a prominent feature of CPZ pathology, however axon damage and severe functional deficits are not. These results reveal a significant role of inflammatory demyelination in causing visual pathway neurodegeneration in EAE as compared to minimal axon damage with CPZ demyelination, mimicking diverse pathology observed in MS patients.

Table of Contents

List of Figures

List of Tables

Chapter 1: Introduction

1.1 Visual impairment and multiple sclerosis (MS)

Multiple sclerosis (MS) is an autoimmune demyelinating and neurodegenerative disease of the central nervous system (CNS) which affects 2-2.5 million people in the world, making it one of the world's most prevalent non-traumatic debilitating neurological disorders (Browne et al., 2014). During disease progression, MS patients exhibit visual, motor, and cognitive impairments, which severely detract from quality of life (Chiaravalloti and DeLuca, 2008; Dobson and Giovannoni, 2019; Hunter, 2016; Jasse et al., 2013). Furthermore, MS most frequently affects middle-aged adults often within the prime of their lives.

Visual disabilities associated with MS can have significant impacts, not only for patients, but also for their caretakers and society as a whole. The highly myelinated nature of the visual pathway makes it particularly susceptible to MS-induced inflammatory demyelination. Visual deficits are often the initial presenting sign of MS and persist in almost all patients throughout the progression of the disease (Costello, 2016; Roodhooft, 2009). Symptoms including visual field impairment, ocular motor disorders, and decreased contrast sensitivity often result in acute or progressive vision loss (Nerrant and Tilikete, 2017; Ortiz-Perez et al., 2016). In cases of severe vision loss, patients experience difficulties in performing basic tasks and impaired mobility, which lead to increased risk of injury, dependence on others, and reduced quality of life (National Academies of Sciences et al., 2016). Individuals with visual impairment also exhibit higher rates of

depression, anxiety and other psychological problems (Kempen et al., 2012). Additionally, the severity visual field impairment in MS is correlated to the extent of neuroaxonal injury within the CNS, and associated with a higher risk of MS disability progression(Ortiz-Perez et al., 2016).

Visual dysfunction has been a well-known aspect of MS pathology since the 19th century. At that time another disorder, optic neuritis (ON), had been well characterized and found to be frequently associated with MS (Buzzard, 1893; Volpe, 2008). ON is an inflammatory pathology which damages the optic nerve resulting in sudden onset of vision loss in one or both eyes. It is an acute disorder, with partial vision returning to the patient within one to three months. ON quite frequently results in demyelinating lesions within the optic nerve, similar to those observed in other areas of the CNS in MS (Toosy et al., 2014). In the late 19th century and first half of the 20th century, a subset of medical research was focused on finding a cure for ON although with limited success. In the 1950's, development of corticosteroids led to their frequent prescription for ON treatment, even though corticosteroid treatment had been reported to be ineffective in improving optic neuritis outcomes (Volpe, 2008).

This discrepancy, and the association between MS and ON, led to the seminal ON treatment trial, the goals of which were to evaluate the effectiveness of corticosteroid treatment for ON and to determine the risk of developing MS after ON episodes. The results of the trial confirmed the lack of efficacy of corticosteroids for treating ON, and that a significant number patients who had ON would go on to develop MS within two years (Beck et al., 1992). The results of the ON treatment trial spurred a wealth of research into

visual dysfunction in MS and the potential of using visual outcomes as a biomarker for disease progression, and efficacy of therapeutic intervention.

It has been difficult to study MS-induced visual pathology in human patients, due to limitations associated with *in vivo* access to the CNS. Most pathological investigations to date have employed optical coherence tomography (OCT) and magnetic resonance imaging (MRI) to evaluate structural changes within the retina and visual pathway respectively, as well as diffusion tensor imaging (DTI) to investigate diffusional abnormalities in MS(Andersen et al., 2018; Graham and Klistorner, 2017; Manogaran et al., 2016). To assess functional deficits in the visual pathway, techniques such as electroretinograms (ERGs) which assess retinal function, visual evoked potentials (VEPs) which assess visual pathway function as a whole, and neurological assessments of visual function, can also be performed in living patients(Balcer et al., 2017; Graham and Klistorner, 2017; Janaky et al., 2017). Although these have provided a wealth of information about the progression of visual pathology in MS, the underlying cellular and molecular changes precipitating macroscopic structural changes and functional loss are not accessible without post mortem histology. As a result, post-mortem analyses are frequently employed to study MS pathology in other brain regions, however only a few studies have investigated visual pathway structures(Evangelou et al., 2001; Kerrison et al., 1994). A significant drawback of post-mortem assessments in humans is their inability to provide information about disease onset and progression, making it difficult to gain etiological insights.

To approach these challenges primate and rodent animal models of MS can be used to study the functional and pathological progression of disease at individual histological timepoints. Primate models are particularly useful due to the close similarities between primate and human visual systems. However, research in primates presents significant institutional and ethical difficulties, making such studies relatively difficult to complete. The rodent visual system is comprised of many of the same structures present in the human visual system, however the cellular organization and circuitry within those structures are distinctly different. Still, the accessibility of rodents in research studies and the similarities which do exist between rodent and human visual systems, make them useful for studying progression of visual pathway pathology. To this end, translationally relevant *in vivo* assessments such as OCT, MRI, DTI, ERGs, and VEPs can be performed in conjunction with timed histological assessments which cannot be completed in humans.

Most studies in rodent models for MS have primarily focused on the anterior portions of the visual system, as they are the historical target of ON. However, visual pathology in MS has been reported to affect not only the retina and optic nerve, but also more posterior visual pathway structures such as the optic tract, lateral geniculate nucleus (LGN), and visual cortex (Balk et al., 2015; Gabilondo et al., 2014; Gabilondo et al., 2017; Papadopoulou et al., 2019; Shen et al., 2019). Thus, investigations into posterior visual pathway pathology are needed. The following work evaluates the rodent visual system as a screening tool for preclinical therapeutics, and provides the first cohesive assessment of posterior visual pathway pathology in two animal models of MS. Because visual deterioration is particularly devastating to MS patients, who consider it the second most

valuable bodily function at risk after motor function (Heesen et al., 2008; Mowry et al., 2009), such studies focused on understanding visual pathway pathology and developing therapies which can improve visual function are of dire need.

1.2 An overview of the afferent visual system

The visual system can be segregated into the afferent and efferent pathways, both of which are affected in MS. The afferent system is the primary route by which visual stimuli are received and processed by the eye and brain. In contrast, the efferent system is comprised of a series of CNS circuits which modulate and employ input from the afferent system to control secondary events such as oculomotor function and circadian responses.

In primates, the afferent visual system is composed of the retina, optic nerve, optic tracts, lateral geniculate nucleus (LGN), optic radiations, and the primary visual cortex (V1) (**Figure 1.1A**). Among many other cell types, the retina contains retinal ganglion cells

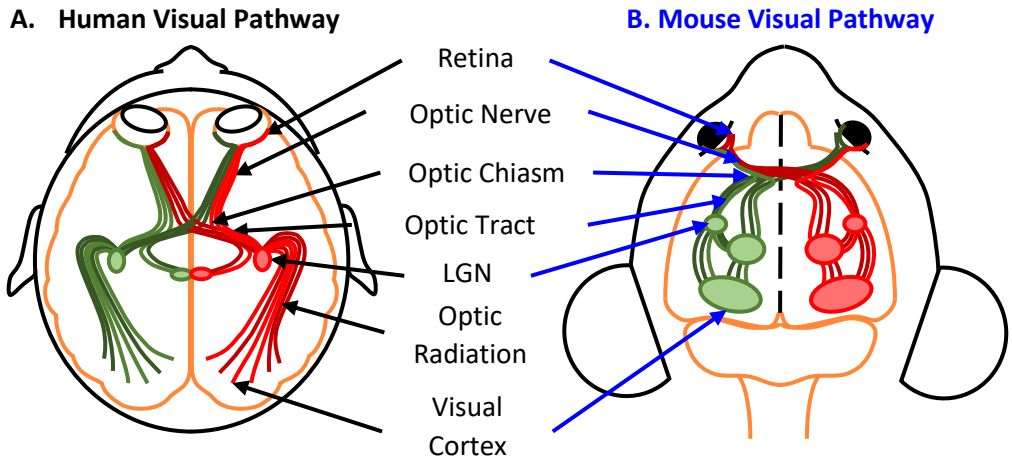

Figure 1.1 Line diagram of human and mouse visual pathway.

(RGCs), the axons of which leave the retina and form the optic nerve. At the optic chiasm, axons of the optic nerve decussate: some axons cross to the contralateral hemisphere of the brain and others remaining ipsilateral to the originating eye. The axons then enter the brain via the ipsilateral or contralateral optic tract, then travel to distinct synaptic targets in the visual system. Many RGC axons synapse on the LGN while other axons or collaterals synapse on various efferent visual pathway targets such as the superior colliculus, suprachiasmatic nucleus, olivary pretectal nucleus, and accessory optic system. Rodents have similar nuclei and tracts; however, mice and rats do not have prominent optic radiations (**Figure 1.1B)**.

Other major differences between primate and rodent visual systems include the degree of overlap between the visual field of the left and right eyes, the position of the eyes in the head, the extent of axon crossover from the eye to the contralateral side of the brain via the optic chiasm, and visual acuity. In humans and many primates, the eyes are situated just lateral to the nose and facing directly forward. As a result, the visual field of each eye extends about 95 degrees temporal from center and 60 degrees nasal, with a binocular overlap of approximately 120 degrees, or 63% (Spector, 1990). Almost all fibers from the nasal half of the retina cross to the contralateral hemisphere of the brain, while fibers from the temporal region remain on the ipsilateral side, resulting in approximately 55% crossover (Creel, 1995b). With these traits, integration of information from both eyes in downstream synaptic targets is possible and allows for clear depth perception and visual isolation of camouflaged entities. Primates also tend to have much higher visual acuities

than rodents. These physiological attributes are common features in animals which need to hunt for prey or search for small vegetation (Mazade and Alonso, 2017).

In contrast, prey animals such as rodents primarily have eyes on opposing sides of the head resulting in large horizontal visual fields, but narrow binocular overlap (Mazade and Alonso, 2017). For instance, the mouse visual field encompasses 320 degrees, 13% of which is binocular vision. This configuration is especially useful for scanning the surroundings for potential predators. It is not surprising then that, only 3% of RGC axons remain on an ipsilateral trajectory as, minimal binocular integration is necessary (Wilks et al., 2013).

1.2.1 The retina

Light information first enters the visual system in the retina. The retina is positioned in the posterior of the eye and rests upon the pigment epithelium and choroid (Kels et al., 2015). Axons from RGCs across the retina comprise the intraocular optic nerve. These axons accumulate at the optic nerve head, traverse the retina and exit the posterior region of the eye to form the extraocular portion of the optic nerve, which then travels to the brain.

The retinal nerve fiber layer, the most anterior layer of the retina, is composed of intraocular RGC axons. More posterior regions include an inner limiting membrane which forms a diffusion barrier between the retina and the vitreous humor, three distinct nuclear layers containing cell bodies, two fibrous plexiform layers which contain dendritic arborizations and are the primary location for synaptic transmission, the photoreceptor layer (PL), and the aneural pigment epithelium (RPE) (Kolb, 1995). Retinal layers posterior to the RNFL in sequence include the ganglion cell layer (GCL) inner plexiform layer (IPL),

inner nuclear layer (INL), outer plexiform layer (OPL), outer nuclear layer (ONL), PL, and RPE (Kolb, 1995; Masland, 2012).

The neural portion of the retina is home to numerous neuronal cell types including RGCs, amacrine cells, bipolar cells, horizontal cells, and photoreceptors. The cell bodies of RGCs and some displaced amacrine cells are located in the GCL, those of bipolar cells, horizontal cells, and most amacrine cells in the INL, and those of photoreceptors in the ONL. The IPL contains neuropil from RGCs, amacrine cells, and apical dendrites of bipolar cells, whereas the OPL is composed of dendritic arborizations from photoreceptors, horizontal cells, and basal dendrites of bipolar cells. The transmission of visual information within the retina can be described as such:

1. Light casts an image on the eye, passing through most layers to reach the PL.
2. Photoreceptors process the light stimulus and transfer information to bipolar cells.
3. Horizontal cells, connected to large numbers of bipolar cells and to some photoreceptors, as well as amacrine cells, connected to multiple bipolar cells modulate the final bipolar cell output.
4. The final bipolar cell output is transmitted to RGCs which relay visual information to nuclei in the brain.

1.2.1.1 Glial cells of the retina

Glial cells of the retina including astrocytes, Muller glia, and microglia maintain retinal homeostasis by providing structural support, assisting in metabolic processes, phagocytosis of neuronal debris, selective release of some neurotransmitters, potassium

buffering, and maintenance of the blood-retinal barrier (BRB) (Vecino et al., 2016). Muller cells constitute 90% of all glia in the retina and traverse the entire retina from the inner limiting membrane bordering the vitreous, to the external limiting membrane between the PL and ONL. The radial morphology characteristic of Muller glia allows for interaction with cell bodies and processes of all retinal neurons. Functions include the promotion of synapse formation during development, maintenance of synaptic function and supply of neurotransmitter precursors and energy substrates to neuronal synapses (Pfrieger and Barres, 1996). In contrast, astrocytes in the retina are primarily associated with retinal blood vessels, thus astrocyte distribution varies significantly between species (Vecino et al., 2016). Astrocytes have been implicated in retinal blood vessel formation both in normal developmental and pathological conditions due to their primary role in the production of vascular endothelial growth factor (Ozaki et al., 2000; Stone et al., 1995). Astrocytes also provide neurotrophic support, structural support for degenerating axons, and contribute to the preservation of the BRB (Vecino et al., 2016). However, in disease conditions, astrocytes produce various cytokines, chemokines, and complement proteins promoting retinal pathological degradation (Kim et al., 2006). And upregulate matrix metalloproteinase 9, a neutrophil chemoattractant which is also involved in extracellular matrix breakdown, leading to BRB compromise (Delclaux et al., 1996; Zhang et al., 2004). Microglia are tissue macrophages within the CNS which not only play an important role in innate immune responses, but like astrocytes and Muller glia are important for maintaining retinal homeostasis, and neural networks (Hanisch and Gertig, 2014; Ransohoff and Brown, 2012).

In some vertebrate species such as rabbits and dogs, there is a fourth type of retinal glial cell: the oligodendrocyte (OL). Primary functions of OLs in the CNS include myelination of axons, trophic support, and maintenance of saltatory conduction. Unlike primates, rodents and cats in which RGC axons do not become myelinated until exiting the optic nerve head and traversing the lamina cribrosa, species with OLs in the retina have myelinated RGC axons within the RNFL(Miyake et al., 2004; Reichenbach et al., 1988). Furthermore, in about 1% of the human population, intraretinal myelination of ganglion cell axons does occur (FitzGibbon and Nestorovski, 2013). However most vertebrate species do not exhibit this trait.

1.2.1.2 Retinal processing

The human retina has four major types of photoreceptors: rods which respond to low light conditions, long-wavelength cones (l-cones) which respond maximally to red light, medium wavelength cones which respond primarily to green light, and short wavelength cones which respond to blue light(Ebrey and Koutalos, 2001). In contrast, the rodent retina has three photoreceptor types: rods, s-cones, and l-cones. Photoreceptors convert visual stimuli to electrochemical impulses through the use of opsins: G-protein coupled receptors which contain the chromophore 11-*cis* retinal.

Under dark conditions, photoreceptors are depolarized and constitutively release glutamate. A photon of light impinging on a photoreceptor induces a conversion of 11-*cis* retinal to all-*trans* retinal, resulting in a conformational change of the opsin to metarhodopsin II. Metarhodopsin II activates the transducin G-protein causing a signaling cascade which results in the hydrolysis of cyclic guanosine monophosphate (cGMP) by phosphodiesterase (PDE), lowering the intracellular concentration of cGMP. cGMP gated sodium channels close, however continuing potassium efflux results in hyperpolarization of the photoreceptor, and closure of voltage gated calcium channels(Arshavsky et al., 2002; V. Kolesnikov et al., 2014). Decreased intracellular calcium inhibits glutamate release to bipolar cell targets.

Bipolar cells can be categorized in numerous ways based on morphology, chemical attributes, synaptic inputs, and electrophysiological responses to differing stimulus types. Although as many as 13 distinct types of bipolar cells have been characterized(Masland, 2011), bipolar cells can be classified into three overarching categories depending on

photoreceptor input and the bipolar cell response: Rod ON bipolar cells, Cone ON bipolar cells, and Cone OFF bipolar cells. As the names indicate, rod and cone bipolar cells receive their primary synaptic input from rod and cone photoreceptors respectively. The ON or OFF designation indicates the response of the bipolar cell to a photoreceptor which has been stimulated by light. ON bipolar cells increase activity in response to light stimulus in the center of their receptive field whereas OFF bipolar cells undergo inhibition.

Horizontal cells receive synaptic inputs from photoreceptors, as well as gap-junction mediated inputs from neighboring cells, and thus transmit surrounding neuronal signals to bipolar cells(Jeon et al., 1998; Kolb, 2003; Masland, 2012). Thus, the receptive field of bipolar cells can be characterized into the center: photoreceptor direct input, and the surround: horizontal cell inputs comprising responses from neighboring photoreceptors, horizontal cells, and other bipolar cells. Stimulus of the surround results in reversal of the bipolar cell output: ON bipolar cells are inhibited, and OFF bipolar cells excited(Fahey and Burkhardt, 2003). These modulations are especially important in the edge detection and contrast sensitivity required in the vertebrate visual system.

Amacrine cells receive inputs from bipolar and other amacrine cells and provide synaptic input to RGCs. There are around 30 different known types of amacrine cells with many specialized functions, however the overarching role of the amacrine cell within the vertebrate retina is to modulate the RGC output(Gollisch and Meister, 2010; Masland, 2012).

RGCs, are the sole output neuron of the retina. RGC dendritic arborizations reside in the IPL and receive direct inputs from bipolar cells and amacrine cells. As a result, RGC

receptive fields exhibit a similar center-surround morphology with on-center RGCs increasing activity in response to center-oriented stimuli and decreasing activity in response to surround oriented stimuli(Kuffler, 1953). Other designations for RGCs include parasol, which constitute approximately 10% of RGCs, and midget constituting 80% of the population. While parasol RGCs primarily detect the orientation, position, and motion of objects in space, midget RGCs respond to fine detail, and color(Kolb, 2003). RGC axons transmit the final visual output to afferent and efferent visual areas by way of the optic nerve.

1.2.2 The Optic Nerve, Optic Chiasm, and Optic Tracts

The optic nerve, optic chiasm, and optic tracts are highly myelinated structures within the visual system comprised of RGC axons, OLs, microglia and astrocytes. In rodents, the optic nerve is unmyelinated for approximately 120-170μm after exiting the eye and lacks OLs in this region (Sun et al., 2009). The unmyelinated region exhibits densely packed astrocytes which, constitute the glial lamina border located at the junction between the retina and the optic nerve. This region is especially susceptible to blood-brain barrier disruption and is the point of origin of myelin loss and/or axonal degeneration in many visual system pathologies including glaucoma and optic neuritis(Jakobs et al., 2005; Soto et al., 2008; Stojic et al., 2019). Damage to one optic nerve results in monocular visual field deficits ipsilateral to the damaged nerve.

In human development, fibers from the optic nerve reach the chiasm between 4 and 6 weeks, with crossing fibers observable at 11 weeks, and decussation and maturation at

15 weeks(Barber et al., 1954). In the mouse, RGC axons arrive at the midline around embryonic day 14, pause in order to recognize inhibitory cues such as ephrinb2 and slit proteins which are repulsive to RGCs expressing the EphB1 and Robo2 receptor respectively, then revert to the ipsilateral path or continue to the contralateral hemisphere from embryonic day 15 to 16 (Drager, 1985; Erskine and Herrera, 2014; Herrera and Garcia-Frigola, 2008; Herrera et al., 2019; Lambot et al., 2005). This decussation occurs primarily in fibers arising from RGCs located in the nasal hemiretina which receive information from the temporal visual field. As a result, in animal species which have an optic chiasm exhibiting partial axonal crossover such as primates, central chiasmatic lesions can cause temporal visual field deficits in both eyes. Central chiasmatic lesions in rodent species like mice which have approximately 95 percent axonal crossover result in significant deficits across most of the visual field.

As axons leave the optic chiasm, they associate to form the optic tracts. The optic tracts contain axons projecting from the contralateral nasal retina, and the ipsilateral temporal retina. This allows for visual information impinging on corresponding points on the left and right retinas to be processed at approximately the same retrochiasmatic sites in each hemisphere(Fitzpatrick, 2004). Lesions in this region result in temporal visual field deficiencies in the contralateral eye and nasal impairments in the ipsilateral eye.

1.2.3 The LGN and Optic Radiations

Axons from the optic chiasm travel to various synaptic targets within the afferent and efferent pathway, however the major RGC target in the afferent pathway is the dorsal

LGN (dLGN). Though only 5-10% of inputs to the LGN come from the retina, it is the main driver of activity in the LGN(Fisher et al., 2017; Hamos et al., 1987; Kerschensteiner and Guido, 2017). The neurons within the human LGN are arranged in a distinct laminar pattern which incorporates two magnocellular layers, four parvocellular layers, and six koniocellular layers interleaved between magnocellular and parvocellular regions. Large parasol and small midget RGCs, project to similarly large magnocellular and small parvocellular thalamocortical projection neurons in the LGN which have similarly shaped and sized center-surround receptive fields(Kolb, 2003; Usrey and Alitto, 2015). Akin to parasol RGCs, magnocellular cells exhibit fast response times and excel in the detection of swift movement across a stationary background. Parvocellular cells respond to stimuli with high spatial frequencies, allowing for the resolution of fine detail. LGN neurons also include local inhibitory interneurons which similarly receive retinogeniculate excitatory input. In fact, the tight retinotopic mapping between the retinal mosaic and the LGN led to the initially prevalent characterization of the dLGN as a simple relay station incapable of complex visual processing(Kerschensteiner and Guido, 2017). However, individual LGN neurons have been shown to receive monocular input from 1-5 RGCs of the same type indicating the accepted relay function, but also to receive monocular input from 6-36 different types of RGCs indicating a newly described combinatorial function(Kerschensteiner and Guido, 2017). Furthermore, a third category of convergence of up to 90 retinal inputs from both eyes indicated a binocular combinatorial function, a significant requirement for binocular vision processing and depth perception(Rompani et al., 2017).

The mouse and rat LGN exhibit some similarities to the human LGN but also many distinct differences. The mouse LGN includes three distinct structures: the dLGN, the intergeniculate nucleus, and the ventral LGN. RGCs primarily project to the dLGN which also provides the primary thalamocortical afferents. In contrast the intergeniculate leaflet and the vLGN are important structures in the circadian system and thus are components of the efferent visual system.

The well-defined laminar structure of the human LGN is absent in the rodent and replaced by two visually indistinct but neuronally unique areas: a central core whose primary inputs are provided by large-fast spiking RGCs analogous to parasol cells in the human retina, an outer dorsal shell primarily driven by inputs from small slowly conducting RGCs similar to midget ganglia, and a ventral region characterized by another even smaller subtype of RGCs(Martin, 1986; Reese and Jeffery, 1983). Projections from the ipsilateral eye synapse in the center of the dorsal core(Kerschensteiner and Guido, 2017). Similar to humans and other primates, the rodent retina incorporates many types of direction sensitive RGCs, as well as spatially responsive RGCs. These primarily project to the shell and core respectively(Dhande and Huberman, 2014). Interestingly the shell also receives significant excitatory input from the superficial layers of the superior colliculus, an efferent pathway structure involved in visually mediated eye, head and body movements (Bickford et al., 2015; Cruz-Martin et al., 2014). Thus, it is thought be important for transmitting stimulus motion and eye position information to the visual cortex, a feature important for the optokinetic response.

1.2.4 The Visual Cortex

The visual cortex is the primary locus for the formation of the visual image. Thalamocortical projection neurons of the LGN primarily send afferents to layer 4 granule cells of V1. Through the use of intracellular recordings and reconstructions of horse-radish peroxidase filled cells within V1, Gilbert and Wiesel proposed the first theoretical model of V1 microcircuitry in 1983. Specifically, layer 4 granule cells engage in pre-processing then send axonal projections to pyramidal neurons of layer 2/3 in which recurrent networks allow for the bulk of visual processing in V1. The major outputs of layer 2/3 neurons are layer 5 neurons, which project to layer 6 neurons and drive subcortical efferent visual structures such as the superior colliculus, thalamic reticular nucleus, pulvinar nucleus, as well as cortical feedback to the LGN(Douglas and Martin, 2004; Gilbert and Wiesel, 1979; Gilbert and Wiesel, 1983) and higher order visual areas (Glickfeld and Olsen, 2017). This canonical circuit has primarily stood the test of time, with some revisions: thalamocortical projections also innervate deep layers of the cortex (Bureau et al., 2006; Freund et al., 1985; Humphrey et al., 1985) which can be activated independent of Layer 2/3 activity(Constantinople and Bruno, 2013; Huang et al., 1998; Schwark et al., 1986). Furthermore, layer 2/3 has been elucidated as a locus for gain control modulation (Quiquempoix et al., 2018).

The macroscopic organization, and the projection of the retinotopic map to V1 is also well defined. The left visual field is mapped to the half of the occipital lobe located right of the midline, and the right visual field to the opposite side. Visual stimuli in the upper portion of the visual field generate responses in the lower half of the occipital

lobe(Ahlfors et al., 1992). The cortex is organized into ocular dominance columns, which receive input either from the contralateral or ipsilateral eye. Pairs of ocular dominance columns are described as hypercolumns in which one ocular dominance column receives input from one eye, while the other receives input from the contralateral eye(Hubel and Wiesel, 1974; Ts'o et al., 2009). Within the ocular dominance column are multiple orientation columns interspersed with blobs. Orientation columns have neurons which are primarily responsive to stimuli of a particular orientation, whereas blobs are responsive to stimuli of particular colors(Livingstone and Hubel, 1988; Livingstone and Hubel, 1984). Selectivity to individual orientations changes along horizontal and vertical planes of the cortex, with adjacent orientation columns expressing selectivity to stimuli rotated by a few degrees.

As discussed, the cortex contains pyramidal cells and inhibitory interneurons responsible for visual processing. In orientation selective columns, pyramidal cells can be divided into simple and complex cells. Simple cells have rectangular receptive fields which receive inputs from multiple cells within the LGN. If stimuli from the LGN fits the rectangular receptive field the simple cell fires in response(Georgiev, 2011; Hubel and Wiesel, 1962). In contrast, complex cells similarly have varying shapes of receptive fields and receive inputs from multiple simple cells(Hubel and Wiesel, 1962; Martinez and Alonso, 2003).

1.3 Pathologies associated with the visual system in MS

Manifestations of MS pathology related to the afferent visual pathway can include visual blurring as a result of increased body temperature or Uhthoff's phenomenon, as well as impairments in motion perception, contrast sensitivity, low-contrast letter acuity, and color discrimination (Bock et al., 2012; Costello, 2016; Mowry et al., 2009; Villoslada et al., 2012). Other important pathologies of the afferent visual system include uveitis, and ON (Balcer et al., 2015; Beck et al., 1992; Costello, 2016). Approximately 50% of MS patients experience ON prior to exhibiting initial symptoms, while 70% develop the disorder at some point during disease progression (Toosy et al., 2014). ON-associated visual deficits include retinal nerve fiber layer (RNFL) thinning, loss of RGCs, and increased latency in VEPs (Balk et al., 2015; Bock et al., 2012; Fisher et al., 2006; Gabilondo et al., 2014; Villoslada et al., 2012). In contrast, efferent visual pathway dysfunction in MS can include ocular motility disorders, diplopia (double vision) and/or oscillopsia (perceived oscillation of objects in the visual field)(Costello, 2016; Pula and Reder, 2009; Subei and Eggenberger, 2012).

Of the numerous visual disorders associated with MS, ON is the most prominent and well-studied. Significant progress has been made in understanding the relationship between MS and ON partially because inflammation and demyelination of the optic nerve has been represented in various animal models of MS. However, a rigorous pathological and functional analysis of both anterior *and* posterior portions of the afferent visual system in animal models is currently lacking. This is especially crucial because posterior visual

pathway structures such as the LGN, optic radiations, and visual cortex are significantly affected in MS, with or without a history of ON. Specifically, MRI of the visual pathway in MS patients shows decreases in the volume of the LGN, lesions in the optic radiations (OR) and atrophy of the visual cortex (Balk et al., 2015; Gabilondo et al., 2014; Gabilondo et al., 2017; Papadopoulou et al., 2019; Shen et al., 2019). Even in the absence of OR lesions, significant increases in OR axial diffusivity (thought to be indicative of myelin damage), are often evident in MS patients compared to non-MS controls (You et al., 2019). Functional assessment of the visual pathway in MS using VEPs reveal latency changes indicative of myelin loss, and amplitude deficits related to axonal damage(Blanco et al., 2014; Laron et al., 2010; Pakrou et al., 2006; Rodriguez-Mena et al., 2013). Although there are a few histological studies on the retina, optic nerve, optic tract, and LGN in MS(Evangelou et al., 2001; Kerrison et al., 1994), these are limited in that they only provide a snapshot of pathology at death, and cannot easily be correlated to progressive functional deficits. Such assays of the time course of myelin changes and axonal damage in animal models, for which histological studies are significantly more accessible than human tissues, are especially crucial. Because all afferent visual nuclei and tracts contribute to the final visual output in normal conditions, all visual system components including the retina, optic nerve, optic tract, dLGN and visual cortex require investigation in animal models. However, studies have primarily focused on the retina and optic nerve anterior regions. Thus, in the following work, we:

a. Investigate posterior visual pathway pathology in the Experimental autoimmune encephalomyelitis (EAE) mouse model for MS.

b. Evaluate the efficacy of therapeutic remyelination on attenuating visual pathway pathology in EAE.
c. Determine a critical therapeutic window for remyelination in EAE.
d. Investigate posterior visual pathway pathology in the cuprizone (CPZ) demyelination mouse model for MS with longitudinal studies.

Chapter 2: Experimental Methods

2.1 Animals

All procedures were conducted in accordance with the National Institutes of Health guidelines and approved by the Institutional Care and Use of Laboratory Animals Committee at the University of California, Riverside (UCR) and the University of California, Los Angeles (UCLA). To understand the extent of EAE effects in OLs and neurons, we made use of PLP_EGFP and Thy1-YFP mice respectively, in addition to C57Bl/6 wild-type mice. Thy1-YFP transgenic mice were purchased from the Jackson Laboratory. B6.Cg-Tg(Thy1- YFP)16Jrs/J mice (JAX #003709, Bar Harbor ME) were backcrossed to wild type C57BL/6 mice for more than five generations(Feng et al., 2000). PLP-EGFP breeding pairs backcrossed to C57BL/6 mice, a kind gift provided by Dr. Wendy Macklin (University of Colorado, Denver CO, USA), were bred and housed in UCLA and UCR vivarium facilities. The generation, characterization, and genotyping of these mice has previously been reported (Mallon et al., 2002). Mice were all kept on a 12 hr light/dark cycle with unrestricted access to food and water.

2.2 EAE induction

EAE was induced in eight- to twelve-week-old male wildtype Thy1-YFP, PLP-EGFP and C57Bl/6 mice (**Figure 2.1A**) as previously described (Hasselmann et al., 2017b; Mangiardi et al., 2011). In brief, one-part lyophilized myelin oligodendrocyte protein

peptide 35-55 (MOG_{35-55}) (Mimotopes, San Diego, CA) in Dulbecco's phosphate buffered saline without calcium or magnesium (DPBS) and 1.3 parts heat killed *Mycobacterium tuberculosis* H37 Ra (Beckton Dickinson, Franklin Lakes NJ) in complete Freund's adjuvant (CFA; Becton Dickinson, Franklin Lakes NJ) were emulsified, resulting in a final concentration for both MOG_{35-55} peptide and *M. tuberculosis* of 2 mg/mL. Mice were anesthetized with 2% isoflurane gas in oxygen at a flow rate of 2 L/min.

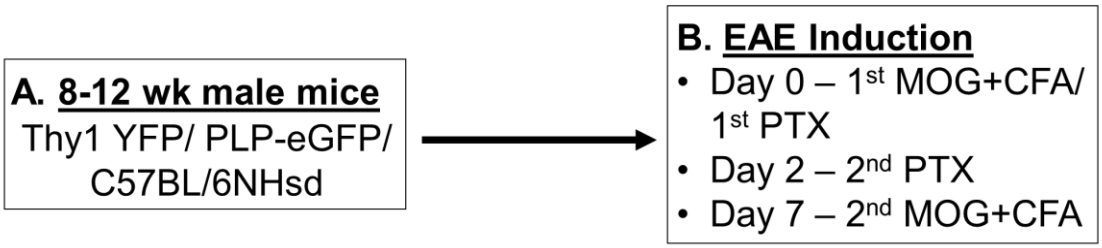

Figure 2.1: EAE induction protocol. A. Eight- to twelve-week-old male Thy1-YFP, PLP-eGFP, and C57Bl/6 mice were induced with EAE. **B**. EAE induction protocol involved initial MOG+CFA immunization and PTX injection on day 0, second PTX injection on day 2, and second MOG+CFA immunization on day 7.

On the first day of induction (Day 0), 0.05 mL of the emulsion was injected subcutaneously into the backs of the animals between the cervical vertebrae and left shoulder and another 0.05 mL between the lumbar vertebrae and left thigh. Injections were placed as such to maximize proximity to axillary and inguinal lymph nodes. Each mouse was then injected intraperitoneally (IP) with 0.3 mL of Pertussis toxin (PTx; List Biological Laboratories, Campbell CA) in DPBS at 1.667 µg/mL, returned to its home cage with free access to water and food and monitored until recovered. Two days after induction (day 2), the mice were given booster IP injections of PTx at the same concentration. Five days later (day 7), motor function was assessed using clinical scores, then mice were injected with a freshly made MOG_{35-55} /*M. tuberculosis* emulsion at the same ratios and concentrations

used on Day 0 (**Figure 2.1B**). Day 7 MOG_{35-55} injections at 0.05 mL each were placed between the cervical vertebrae and right shoulder, and the lumbar vertebrae and right thigh.

2.3 EAE clinical scoring

Starting 7 days post induction (dpi), mice were scored daily for clinical disease severity. The clinical scoring protocol was defined as: 0, unaffected; 1, complete tail limpness; 2 failure to right upon attempt to roll over; 3, partial hind limb paralysis; 4, complete hind limb paralysis; and 5, moribund (Hasselmann et al., 2017a). Mice reaching clinical scores of 4.5 or higher were euthanized humanely with isoflurane anesthesia followed by cervical dislocation.

2.4 OCT

OCT data plots of mouse retinas were acquired with spectral domain-OCT (R2200 840 nm HHP; Leica, Buffalo Grove IL) in tangent with Bioptigen InvivoVue software (Leica, Buffalo Grove IL). Animals were anesthetized with IP injections of 100 mg/kg body weight ketamine (Putney Veterinary Generics, Portland OR) and 10 mg/kg bodyweight xylazine (Lloyd Laboratories, Marikina Phillipines) resulting in 1 to 1.5 hours of sedation. After animal was fully sedated, eyes were dilated with 1% tropicamide (Alcon Laboratories, Fort Worth TX) for 10 minutes. The animal was then placed on the OCT system and arranged such that the temporal field of the retina was in full view. Systane

ultra-lubricant eye drops were applied to eye spears (Novartis, Basel Switzerland) and applied intermittently throughout the procedure to prevent dehydration of the eye and cataract formation. One thousand A-scans and one hundred B-scans were taken to generate each OCT image. Each image was taken 3 times and averaged. After imaging, the eye was lubricated with ophthalmic ointment (Dechra Veterinary Products, Northwich UK) to prevent cataract formation during the remaining anesthesia period (You et al., 2015). Post-experiment care included animals being placed in a large open-air container with a heating pad set to 40˚C and monitored. Once awake, animals were returned to respective home cages.

OCT data plots were analyzed just lateral to the optic nerve in order to minimize fluctuations in layer thickness observed near the optic nerve. Automatic segmentation with Bioptigen Diver 3.0 software (Leica Microsystems, Buffalo Grove IL) measured, then averaged individual retinal layer thicknesses based on the optical elements of the system. Software segmented individual retina images and avoided inclusion of blood vessel diameter in RNFL calculations.

2.5 ERGs and VEPs

Ocuscience Handheld Multi-species ElectroRetinograph (Occuscience Henderson NV) was used to measure changes in retinal and visual function by recording ERGs and VEPs respectively before midday (00:00-12:00). Before recording mice were dark adapted for at least five hours.

Animals were anesthetized with 2% isoflurane (Piramal Healthcare, Mumbai India), in sterile medical grade oxygen delivered through an isoflurane/oxygen induction chamber and/or face mask. Body temperature was maintained at 37°C. Eyes were dilated with 1% tropicamide for 10 minutes before recording and visine dry eye drops were applied every 2-3 minutes to hydrate eyes and prevent cataract formation (You et al., 2015).

Stainless steel subdermal electrodes (F-Needle Electrode (F-E2); OcuScience, Henderson NV) were inserted on either side of the snout (reference electrodes). For ERG recordings silver-embedded thread electrodes (1.5" Filament (2); OcuScience, Henderson NV) were placed over the cornea and held in place with mini contact lenses filled with a saline solution to optimize conductivity between the electrode and the cornea. During VEP recordings subdermal electrodes were inserted 2-3 mm lateral to the midline above the visual cortex on the left and right side (Hegedus et al., 2009; Yu et al., 2011). Mini contact lenses filled with saline solution were placed over the eyes during VEP recordings to prevent dehydration.

ERG and VEP traces were averaged using Occuscience ERG viewer. A minimum of 5 traces for ERGs, and 25 traces for VEPs were averaged per mouse. The traces were then filtered for 60 Hz noise, along with a low pass filter of 150 Hz with MATLAB. Trace baselines were adjusted to 0 at the onset of the light stimulus. Only VEP traces were smoothed (3rd order Savitzky-Golay, 50 points per window (Schulz et al., 2009)). MATLAB was used to identify and measure ERG and VEP peak amplitudes and latencies.

2.6 Perfusions and tissue preparation

Mice were deeply anesthetized with isoflurane and intracardially perfused with ice cold phosphate buffered saline (PBS) then 10% formalin in PBS (Fisher Scientific, Waltham MA). Eyes, optic nerves, and brain were dissected and post-fixed in 10% formalin for immunohistochemistry (IHC). After 24 hours, tissue excluding eyes was transferred to 30% sucrose with 0.2% sodium azide for 2 days (Fisher Scientific, Waltham MA) for cryoprotection. Tissue was embedded in a gelatin/sucrose solution (7.5% w/v gelatin (Becton Dickinson, Franklin Lakes NJ) +15% w/v sucrose (Fisher Scientific, Waltham MA) in Milli-Q water). Gelatin tissue blocks were placed in 10% formalin overnight, followed by 30% sucrose+0.2% sodium azide solution until ready for sectioning. Retina processing was initiated by removing cornea and lens from eyes. Retina attached to sclera were transferred to 10% formalin for 24 hrs followed by 30% sucrose. Retinas were embedded in optimal cutting temperature compound, then placed in 2-methylbutane (EMD Millipore, Burlington MA) on dry ice to allow for uniform freezing. Embedded retinas and optic nerve gelatin blocks were cut to 10 µm thick sagittal sections using a cryostat and affixed directly to warm slides. Brain gelatin blocks were flash frozen on dry ice, and cut to 40 µm thick coronal sections, then placed in PBS with 0.2% sodium azide.

2.7 IHC

Prior to antibody application, tissue sections were thoroughly washed with PBS to remove residual sodium azide, permeabilized with 0.3% Triton-X (Electron Microscopy Sciences, Hatfield PA) and blocked in 20% normal goat serum (NGS) (Sigma-Aldrich, St. Louis MO). Sections were incubated in 1:500 dilutions of primary antibodies (**Table 1**) for 2 hours at room temperature followed by overnight at 4^{o}C. The following day, the sections were washed with PBS and then tris buffered saline (TBS). The sections were incubated with the corresponding secondary antibodies in TBS: Goat anti-rabbit IgG Cy3 (EMD Millipore, Burlington MA), Goat anti-Rat IgG Cy5 (Invitrogen, Carlsbad CA), Goat anti-mouse Cy5 IgG (Invitrogen Carlsbad, CA). Sections were co-stained with 4',6-Diamidino-2-Phenylindole (DAPI; EMD Millipore, Burlington MA) to quantify cell numbers. Finally, the sections were washed again with TBS, mounted, and cover-slipped.

Antibody	Target	Vendor	Catalog #
MBP	Myelin basic protein	Abcam	ab40390
CD45	Cluster of differentiation 45; Pan leukocytic antigen (clone 30-F11)	Becton Dickinson	550539
GFAP	Glial fibrillary acidic protein	Invitrogen	180063
Iba-1	Ionized calcium binding adaptor molecule 1	Wako	019-19741
PV	Parvalbumin (clone PARV-19)	EMD Millipore	MAB1572
RBPMS	RNA binding protein with multiple splicing	PhosphoSolutions	1830
Casp-3	Caspase-3 (clone AM1.31-11)	EMD Millipore	AM65
ERβ	Estrogen Receptor β	EMD Millipore	05-824
CC1 (APC)	Adenomatous polyposis coli (mature myelinating OLs)	GeneTex	GTX16794
Olig2	OL transcription factor 2	ThermoFisher	P21954
NeuN	Neuronal nuclei	EMD Millipore	ABN78

Table 1. Primary antibodies used for examining myelin, leukocytes, astrocytes, parvalbumin positive interneurons, RGCs, apoptosis and ERβ reactivity. Antibodies were paired with either Cy5 or Cy3 secondary antibodies for IHC.

2.8 Microscopy

Sections were imaged at similar light exposures using an Olympus BX61 spinning disc confocal microscope equipped with 10x and 40x Super Apochromat objectives (Olympus America Inc., Cypress CA) connected to a camera (Hamamatsu Photonics Orca-R^2, Hamamatsu Japan). Z-stack images were acquired, and projection images compiled using Slidebook 6 software (Intelligent Imaging Innovations Inc, Denver CO).

Immunofluorescence intensity and cell numbers was assessed with NIH ImageJ software (v1.50i http://rsb.info.nih.gov/ij/) and quantified for CD45, MBP, and GFAP immunofluorescence, or cell counts for $RBPMS^+$, casp-3^+, $ER\beta^+$, PV^+, Thy1-YFP^+ and PLP-$EGFP^+$ cells. Histograms were adjusted evenly to match those of control images and saved. Files were then converted to RGB tagged image format (.tif) files and transferred to ImageJ where individual color channels were converted to gray scale. Brightness and contrast were automatically adjusted using the to limit experimenter bias and a region of interest was traced around an area encompassing the retina, optic nerve, optic tract, LGN, or visual cortex. The threshold of staining for each image and thus the percentage of fluorescent pixels in each area of interest was computed by the software and reported in a table, which was transferred to Prism® (Graphpad, La Jolla CA) for statistical analysis. For cell counts in the retina, images were taken at 40x and all relevant cells in the GCL were counted, corresponding to a length of 0.25 mm. In the optic nerve, PLP images were taken at 10x, GFAP and MBP and 20x, and Thy1 at 40x. For PLP images, PLP^+ cells were counted across the region of interest. Brain sections containing the optic tract, LGN, or visual cortex were imaged at 10x, 20x, or 40x magnification depending on the stain. For Thy1 and PV cell counts, an overlay grid with bin dimensions of 316.23 x 316.23 pixels was placed over images and cells were counted in two or three of the grid areas respectively, depending on the density of cells in the image. For axon swelling counts in white matter tracts, single-channel images from Thy1 sections were thresholded in the region of interest corresponding to the optic nerve or optic tract. The ImageJ analyze particles function was used to count the number of axonal blebs (particles) present in the

thresholded image, within the region of interest. Results from all counts were analyzed in GraphPad Prism as well.

2.9 Electron microscopy

Optic nerves dissected from paraformaldehyde perfused mice were post-fixed in 2% glutaraldehyde (Electron Microscopy Sciences, Hatfield PA) and 5% formalin (Fisher Scientific, Waltham MA). Optic nerves were Epon embedded and stained with uranyl acetate-lead citrate. Number of myelinated and unmyelinated axons and the g- ratio (the ratio of the axon diameter to the total myelinated fiber diameter), was quantified as in previous studies for at least 300 axons per group (Crawford et al., 2009a). For each axon, two measurements for axon diameter were made.

2.10 Statistics

For IHC, two sections per mouse were taken for each area of interest in the brain and three sections per mouse for retina and optic nerve tissues. There were 4-10 mice per treatment group. For ERG, VEP and OCT *in vivo* studies n=4-8 mice per group were used. Both eyes were assessed in all *in vivo* studies resulting in a minimum of n=8 eyes per group.

Statistics were performed using Prism® (GraphPad, La Jolla) program for Windows. Graph values are expressed as mean $\pm$ standard error of the mean. For histology, EM, and *in vivo* studies statistical analysis of mean values was carried out using one-way

ANOVA if mean values passed a normality test, or Kruskal Wallis multiple comparison test if they did not. For EAE clinical scores, statistics were performed using an ordinary two-way ANOVA with Bonferroni post-hoc test as previously described (Hasselmann et al., 2017a). Differences were considered significant at the *$p<0.05$, **$p<0.01$, ***$p<0.001$, and ****$p<0.0001$ level.

Chapter 3: Axon damage in the visual pathway interferes with remyelination induced functional recovery in a mouse model of MS

3.1 Introduction

The EAE model is a commonly used model for MS which exhibits neurological deficits similar to those seen in MS including ON (Bettelli et al., 2003; Shao et al., 2004). As such it is used to understand these neurodegenerative events in the context of immune mediated demyelination and is the most commonly used animal model for ON. Furthermore, it has been invaluable in mechanistic studies of currently approved MS drugs and in screening various therapeutic agents including neuroprotective estrogens, prior to clinical trials(Tiwari-Woodruff and Voskuhl, 2009). In the following studies transgenic mice, Thy1-YFP, which express green fluorescent protein under a neuron-specific promoter of the Thy1 gene, are used to investigate EAE-induced effects on RGCs, optic nerve, optic tract axons, and visual cortex pyramidal neurons (Feng et al., 2000; Porrero et al., 2010). Whereas, PLP-EGFP transgenic mice, which express green fluorescent protein under the OL specific proteolipid protein (PLP) promoter are used to assay changes in the number of white matter OLs and myelin (Mallon et al., 2002). Imaging OCT analysis of the retina, and IHC across the visual system is employed to assess structural changes in all afferent visual pathway nuclei and tracts. Functional modalities, ERGs and VEPs are used to evaluate EAE-induced functional changes to the retina and the afferent visual system.

OCT, ERG, and VEP analysis of the visual pathway are then evaluated as translationally relevant tools for assessment of promising preclinical therapeutic agents.

ERbeta Ligands

It has long been observed that MS has a marked sex difference with up to three times more incidence in women than in men (Whitacre, 2001) although paradoxically, female sex hormones appear to confer a degree of protection from MS incidence and symptoms(Gomez et al., 2013). In fact, pregnant women have fewer relapses during second and third pregnancy trimesters concurrent with higher estrogen levels(Confavreux et al., 1998; Vukusic et al., 2004), while menopausal female patients have aggravated symptoms, matching a period of lower estrogen levels(Bove et al., 2014; Smith and Studd, 1992). This incidence led to the investigation of estrogens in ameliorating MS pathology

Several studies have demonstrated the neuroprotective and therapeutic benefit of estrogen-based treatments, which have been shown to reduce clinical signs and inflammatory lesions in EAE (Ito et al., 2001; Matejuk et al., 2001). However, there are significant side effects associated with estrogen treatment including feminizing effects in males and increased risk for breast and uterine endometrial cancer (Thomas, 1984). These deleterious effects appear to be mediated primarily through estrogen receptor α (ERα) while estrogen receptor β (ERβ) is associated with tumor suppression and reduced cell proliferation (Nilsson and Gustafsson, 2011). The ERβ agonist 3-Chloro-2-(4-hydroxyphenyl)-2H-indazol-5-ol (IndCl) developed by Katzenellenbogen group (De Angelis et al., 2005) has a >100 fold selectivity for ERβ over ERα (De Angelis et al., 2005)

and has demonstrated immunomodulatory, remyelinating, and neuroprotective effects in spinal cord and callosal axons (Karim et al., 2018b; Moore et al., 2014b; Saijo et al., 2011). Because remyelinating therapies are being rigorously investigated in pre-clinical and clinical trials as the next wave of MS therapeutics, we evaluate the efficacy of IndCl, in alleviating visual pathway pathology and dysfunction (Karim et al., 2018a; Moore et al., 2014a). In addition, we assess its potential for improving functional deficits in the afferent visual system, by way of ERGs and VEPs.

Our initial results indicate: i) Chronic EAE induced significant RGC death, inflammation, demyelination, and axon damage throughout the visual pathway, as well as functional deficits as assessed by ERG and VEP. ii) Therapeutic treatment with IndCl during EAE significantly increased the number of myelinated axons in almost all major white matter tracts within the visual pathway, and attenuated RGC loss in the retina. However, these near global improvements in axon myelination were not sufficient to attenuate axon degeneration nor recover functional deficits in the visual pathway of EAE mice. Thus, to obtain meaningful functional recovery in demyelinating diseases, potential therapeutics must not only target remyelination, but must also prevent further axonal degeneration and neuron loss.

3.2 Methods

Eight- to twelve-week-old male Thy1-YFP, PLP-EGFP, and C57Bl/6 mice were induced with EAE for two individual experiments: experiment (expt) “a” and expt “b”. EAE disease onset occurred 10 to 13 dpi, reached peak disease severity between 15 and 21 dpi, and maintained severity through late EAE and euthanasia at 60 dpi (**Figure 3.1**). Mice received daily drug or vehicle subcutaneous injections starting at peak disease, which occurred 15 dpi for expt “a”, and 21 dpi for experiment expt “b” (**Figure 3.1Aii, 3.1B**). Expt “a” mice underwent ERGs and VEP visual function assessments at 40dpi, OCT retinal assessment at 45dpi, and were euthanized at 50dpi. Expt “b” mice were euthanized at 60 dpi for IHC. For treatment injections, mice were separated into vehicle and IndCl treatment groups such that an even representation of clinical scores was evident in both groups. Average mouse bodyweights were used to calculate drug dosage. IndCl at 5 mg/kg body weight was dissolved in vehicle (10% ethyl alcohol; Electron Microscopy Sciences, Hatfield PA and 90% Miglyol 812N; Cremer, Hamburg Germany). Vehicle and IndCl syringes and mouse cages were color coded for blinded treatment effects. Naïve normal controls did not develop clinical disease. Wild-type C57Bl/6 and these transgenic lines undergo a similar EAE clinical disease course(Bannerman et al., 2005; Crawford et al., 2010; Mangiardi et al., 2011). Treatment with IndCl at peak disease decreased clinical disease severity over time, an effect that reached significance at 32 dpi and persisted through experiment end similar to previously published results (**Figure 3.1B**)(Karim et al., 2018b; Karim et al., 2019a; Moore et al., 2014a).

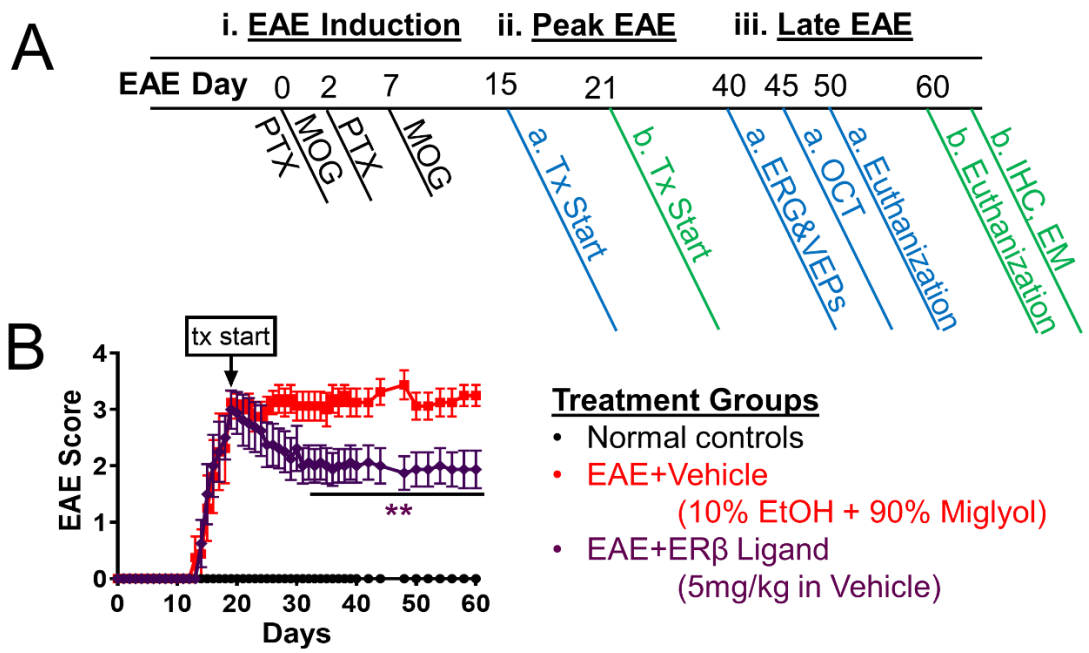

Figure 3.1: Experimental design for assessment of IndCl therapeutic effects in visual pathway of EAE mice. A. EAE was induced in male Thy1-YFP, PLP-eGFP and C57Bl/6 mice in two experiments: expt. "a" (blue) and expt "b" (green). Mice received daily therapeutic treatment, beginning during peak EAE at 15dpi (expt "a") or 21dpi (expt "b") through experiment end. Expt "a" mice received ERG and VEP visual function assessments at 40dpi, and retinal imaging with OCT at 45dpi. During late EAE, expt "a" mice were euthanized 50dpi, and expt b mice at 60dpi. Tissue from expt "b" mice was processed for IHC or electron microscopy. **B.** Representative clinical scores for Thy1-YFP and PLP-EGFP age-matched mice induced with EAE (from expt "a"). One representative EAE experiment of two is shown. Disease onset occurred around 12 dpi with peak disease from 16 to 20 dpi. IndCl was given daily at 5mg/kg via subcutaneous injection beginning 21 dpi. Treatment groups included normal controls (black), EAE + vehicle (10% ethanol, 90% miglyol) (red), and EAE + IndCl (5mg/kg in vehicle) (purple). Normal controls do not show any changes in clinical score from baseline. IndCl treated mice show decreased clinical scores over time, becoming significantly lower than vehicle from 32 to 60 dpi. Statistical differences between groups were determined using two-way unbalanced ANOVA with Dunnett's multiple comparisons test n= 8 mice per group; $^{**}P$ <0.01.

3.3 Results

The MOG_{35-55} EAE model leads to significant demyelination, inflammation, and neurodegeneration along with motor deficits (Hasselmann et al., 2017a; Karim et al., 2019b; Mangiardi et al., 2011). Pathology and functional deficits have been assessed in the spinal cord, corpus callosum, cortex, hippocampus, and cerebellum (Crawford et al., 2010; Kumar et al., 2013; Mangiardi et al., 2011; Ziehn et al., 2010). With respect to the visual system pathological studies have primarily focused on the anterior portion of the visual pathway, specifically the retina and optic nerve (Horstmann et al., 2016; Lin et al., 2017; Nishioka et al., 2019; Stojic et al., 2019). In the current work, we assayed EAE-induced visual pathway demyelination, inflammation, and neurodegeneration along with functional outcomes (VEP and ERGs). In addition, the effect of treatment with a known remyelinating ERβ ligand, IndCl was evaluated. As anterior and posterior visual pathway dysfunction are both key aspects of MS pathology, the results presented here investigate nuclei and tracts of the afferent visual pathway from the retina to the visual cortex.

The retina is a highly organized structure responsible for the initial conversion of the visual image into nerve impulses and subsequent transmission to central visual nuclei. This is achieved by photoreceptors which pass the visual information to interneurons, that pass it to RGCs. Axons of RGCs travel through the optic nerve. RGCs have been shown to be susceptible to damage during demyelinating disease. MS patients show significant thinning of the RNFL, GCL and IPL, indicating loss of RGCs (Graham et al., 2016).

Rodent models of MS have also shown significant retinal pathology along with loss of RGCs (Hobom et al., 2004; Shindler et al., 2006; Shindler et al., 2008).

Retina was isolated from normal, EAE+ vehicle, and EAE + IndCl groups of mice and sectioned along the horizontal plane**.** Shown is a retina section containing the optic nerve from a normal Thy1-YFP mouse (**Figure 3.2A-i)**. In retina sections from normal mice, Thy1 expression was evident in the GCL, IPL, INL, OPL and PL. This was slightly different from another Thy-1 transgenic mouse (B6.Cg-Tg(Thy1-CFP)23Jrs/J reported by Brecha lab) that showed CFP expression in the inner retina, GCL, RNFL and the optic nerve (Raymond et al., 2008). Horizontal midline retinal sections were used for immunostaining and imaged at 20X or 40X magnification lateral to the optic nerve (white dashed box in A) (**Figure 3.2A-ii**).

Decreased retinal expression of ERβ in EAE mice is attenuated by IndCl treatment

Estrogen receptors are expressed in different cell types within the CNS (Mhyre and Dorsa, 2006; Shughrue et al., 1997). The presence of ERβ has previously been confirmed in the human (Munaut et al., 2001) but not in mouse retina. To assess ERβ expression, retinal sections from Thy1-YFP normal, EAE + vehicle and EAE + IndCl groups was immunostained with ERβ. ERβ expression was evident in almost all normal retinal nuclear layers (**Figure 3.2B**). Retinal sections from vehicle-treated EAE mice showed decreased ERβ immunoreactivity in the GCL as compared to normal. Retinas from IndCl treated mice exhibited increased ERβ immunoreactivity in all retinal nuclear layers compared to vehicle. Quantification of $ERβ^+$ $Thy1^+$ neurons in the GCL revealed, a significant decrease in the

number of ERβ^{+} Thy1^{+} cells in in GCL of EAE+vehicle groups as compared to normal. This decrease in ERβ^{+} Thy1^{+} cells in in GCL was attenuated in sections from IndCl treated mice (**Figure 3.2E**).

Increased RGC apoptosis with EAE is attenuated by, IndCl treatment.

RGC numbers were quantified by immunostaining for RBPMS, a selective marker for RGCs (Kwong et al., 2010; Rodriguez et al., 2014). Robust immunostaining with RBPMS was observed in normal retinal sections (**Figure 3.2C, F**). However, retinal sections from EAE+vehicle group exhibited a significant decrease in RBPMS^{+} RGCs. Treatment with IndCl mitigated the loss of RBPMS^{+} RGCs seen in EAE + vehicle group with a return of robust RBPMS staining.

The decrease in ERβ+ Thy1+ and RBPMS+ immunoreactivity in the GCL was investigated for potential EAE-induced GCL cell death. Immunostaining of retinal sections with cell apoptosis marker, casp-3 revealed negligible activity in normal retinal sections (**Figure 3.2D**). However, retinal sections of EAE+vehicle group revealed an increase in EAE-induced cell apoptosis in the RGC and INL (**Figure 3.2D**). Similar EAE-induced cell apoptosis in other CNS regions and RGCs have been previously reported (Al-Shamsi et al., 2015; Duarte-Silva et al., 2018; Kim and Sung, 2017; Meyer et al., 2001). Retinal sections from IndCl treated EAE group showed a significant decrease in casp-3 staining in GCL as compared to vehicle (**Figure 3.2D, G**).

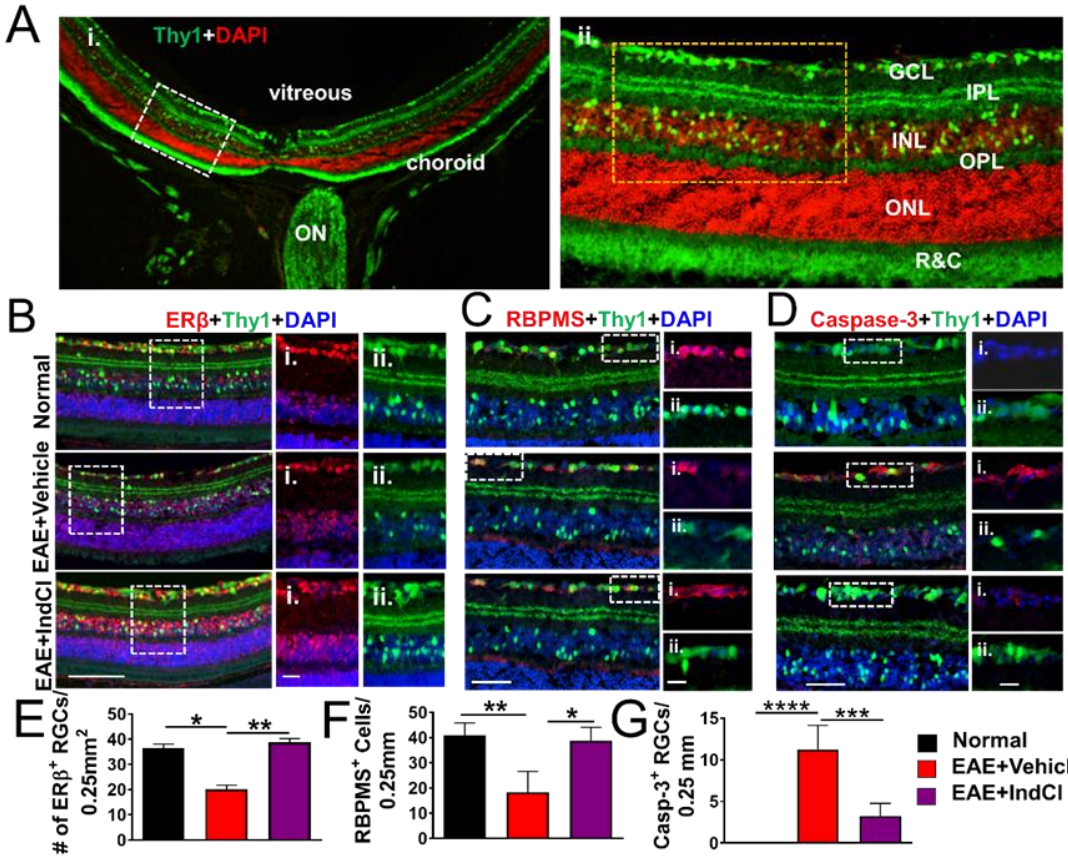

Figure 3.2: Therapeutic treatment with ERβ ligand IndCl improves RGC survival during EAE. A. Representative 10x magnification image of retinas collected from normal Thy1-YFP (green) mice and stained with DAPI (red). Vitreous, choroid and optic nerve structures are identified for orientation. A magnified 20x image of the region indicated by the dashed rectangle in (A) located lateral to the optic nerve, reveals individual retina layers including GCL, IPL, INL, ONL, and layer of rods and cones (R&C) (ii). **B.** Thy1-YFP mouse retina sections collected 60 dpi from treatment groups shown in Figure 1A were immunostained for ERβ (red) and DAPI (blue). Twenty times magnified representative images show fewer neurons in the GCL of vehicle, compared to normal and IndCl sections. Regions denoted by the dashed box were imaged at 40x magnification and show ERβ (i) and Thy1 (ii) for all groups. Thy1$^+$ neurons in the GCL were also positive for ERβ. **C.** Retina sections were immunostained with RBPMS (red), and DAPI (blue). Sections were imaged at 40x magnification and analyzed in the region of interest indicated by the dashed box in (Aii) to generate cell counts. Split images showing RBPMS (i), and Thy1 (ii) for all treatment groups, display a marked decrease in RBPMS$^+$ RGCs in vehicle-treated mice compared to normal controls. IndCl-treated mice show increased RBPMS$^+$ RGCs compared to vehicle. **D.** Retina sections were immunostained with casp-3 (red). Split images show casp-3 (i) and Thy1 (ii) for all groups. High levels of casp-3 immunoreactivity in vehicle sections are attenuated in IndCl sections. **E.** Quantified cell counts show decreased numbers of ERβ$^+$ GCL neurons, (**F.**) RGCs, and (**G.**) increased numbers of apoptotic RGCs with IndCl treatment in vehicle treated mice compared to normal and IndCl groups. n=8 mice per group. *P<0.05, **P<0.01, ***P>0.001, ****P>0.0001 ordinary one-way ANOVA with Dunnett's multiple comparison test. Scale bar is 100µm for 20x image in (B), 50µm for (C) and (D), and 25µm for all zoomed in images.

Microglia and Astrocyte Changes in Retina during EAE

The extent of microglia activation in the retina was examined by immunostaining with calcium binding protein Iba-1 that is highly expressed in microglia. Retinal sections from normal, EAE+vehicle and EAE+IndCl mice were investigated (**Figure 3.3A, B**). EAE+vehicle retinal sections showed activated microglia with no significant increase in Iba-1 cells as compared to normal. Similarly, retinal sections from EAE+IndCl showed a decrease in activated microglial presence, with no significant increase in Iba-1 immunoreactivity as compared to EAE+vehicle.

To investigate the extent of gliosis in the retina, astrocytes were immunolabeled with GFAP antibody. A significant increase in reactivity of astrocytes was observed in EAE+vehicle retinal slices especially in the RGC layer as compared to normal slices (**Figure 3.3A, C**). This indicates an increased expression of fibrillary acidic protein accompanied with an activation of astrocytes triggered by inflammation and apoptosis of RGCs. IndCl treatment decreased the number and reactivity of astrocytes in EAE+IndCl groups as compared to EAE+vehicle groups (**Figure 3.3A, C**).

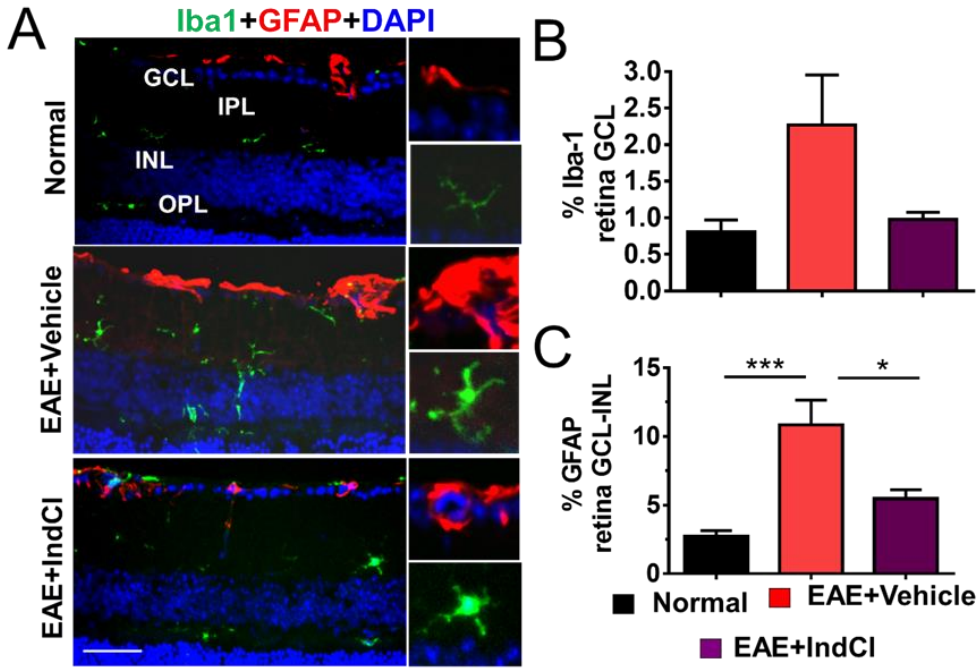

Figure 3.3: EAE retinas exhibit increased microglial and astrocytic activation which is attenuated with IndCl treatment. A. Retina sections from groups shown in Figure 1A were collected 60dpi and immunostained for Iba1 (green) and GFAP (red). Sections were imaged at 20x magnification with representative images shown. Iba1 immunoreactivity is increased in the GCL, and GFAP immunoreactivity in the GCL, IPL, INL, and OPL in EAE+vehicle sections compared to normal and EAE+IndCl sections. **B.** Percent area quantification shows increased Iba1 and significantly increased GFAP (**C.**) immunoreactivity in retina sections from vehicle groups compared to normal and IndCl groups.

EAE-induced leukocytic infiltration and demyelination, astrocytic activation and axon damage in the optic nerve.

The optic nerve is a bundle of axons that originate from ganglion cells and enter the brain. The optic nerve in humans and mice is initially unmyelinated inside the retina and is heavily myelinated thereafter (De Moraes, 2013). Thus, the optic nerve represents a model system to assess effects of inflammation and demyelination on myelinated and unmyelinated axon health. Imaging studies in MS and pathology assessment in EAE have

revealed that optic nerve axons are susceptible to demyelination, leukocytic infiltration, and axonal degeneration (Garcia-Martin et al., 2017; Hayreh et al., 1981; Soares et al., 2013). EAE induced by our lab has shown significant pathology of the spinal cord and brain (Hasselmann et al., 2017b; Mangiardi et al., 2011; Moore et al., 2014a). To assess changes in demyelination, inflammation and neurodegeneration in the optic nerve, longitudinal optic nerve sections from PLP-EGFP and Thy1-YFP normal, EAE+vehicle and EAE+IndCl mice were subjected to IHC (**Figure 3.4**).

Axon myelination in longitudinal optic nerve sections was evaluated for MBP immunoreactivity. Normal optic nerve sections were highly myelinated with a relatively consistent distribution of $DAPI^+$ cells (**Figure 3.4A**). In contrast, EAE sections showed significant decreases in myelin intensity, as well as lesions containing increased numbers of DAPI+ cells and decreased MBP intensity indicated by white arrows (**Figure 3.4A, E**). Sections from IndCl-treated mice showed significant increases in myelination compared to vehicle, as well as fewer demyelinated lesions, although regions containing high numbers of $DAPI^+$ cells, indicated by dashed arrows, were not demyelinated (**Figure 3.4A, E**).

To assess leukocytes and astrocytes, PLP-EGFP optic nerve sections were immunostained for CD45, a pan leukocyte marker, and GFAP (**Figure 3.4B**). Normal sections showed a robust population of PLP^+ OLs as compared to EAE+vehicle treated mice where a significant reduction of PLP+ OLs was observed (**Figure 3.4F**). IndCl treatment in EAE mice showed a significant recovery in the number of PLP_EGFP OLs as compared to vehicle treated EAE animals (**Figure 3.4B, F)**. Normal optic nerve sections

showed a negligible number of CD45+ leukocytes, and a baseline level of $GFAP^+$ astrocytes. Vehicle treated EAE mice exhibited extensive $CD45^+$ leukocyte immunoreactivity and astrogliosis compared to normal (**Figure 3.4B-C, G-H**). Sections from IndCl treated mice showed a significant decrease in $CD45^+$ leukocytic immunoreactivity but not astrogliosis, and an increase in PLP^+ cells compared to vehicle.

Onset of demyelination in the optic nerve is associated with axon damage(Hobom et al., 2004). To assess optic nerve axon health, optic nerve sections from normal, EAE + vehicle and EAE + IndCl Thy1-YFP mice were imaged at 40x magnification. Normal optic nerve sections showed coherent and linear Thy1-YFP^+ axons (**Figure 3.4D**). However, in vehicle-treated EAE mice a decrease in Thy1-YFP intensity along with a significant increase in punctate, fragmented "axonal blebs" was observed (**Figure 3.4D, I**). IndCl treatment, showed a modest recovery in Thy1-YFP intensity but showed similar number of axon blebs as compared to EAE+vehicle group.

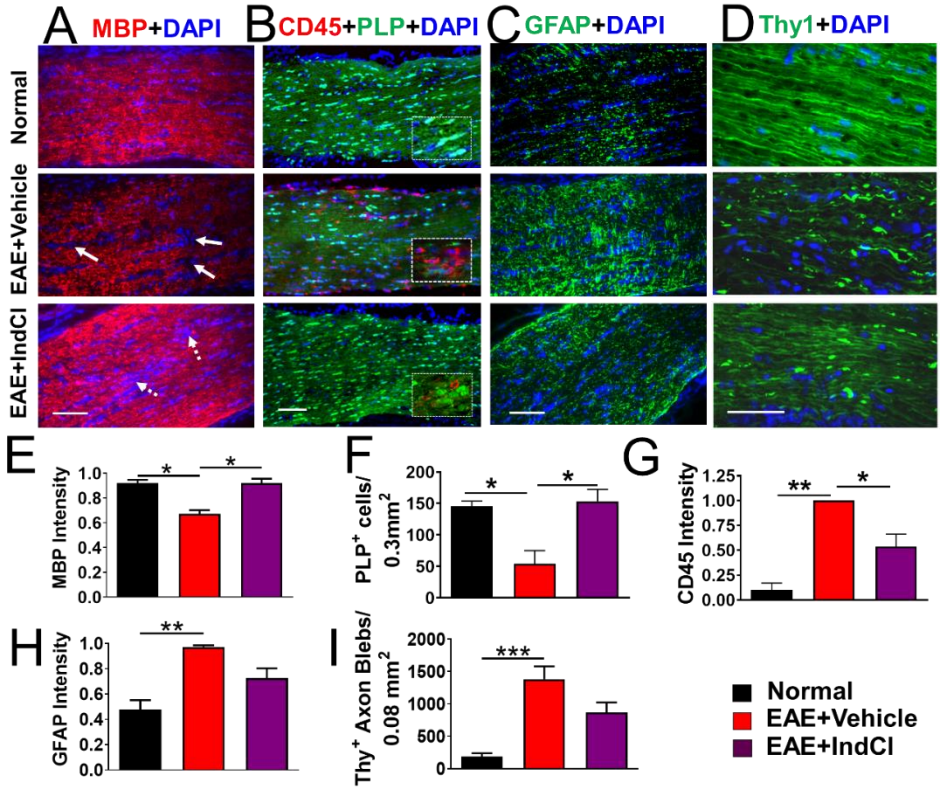

Figure 3.4: IndCl treatment attenuates demyelination, OL loss, and leukocytic infiltration but not axonal degeneration in the optic nerve of EAE mice. A. Optic nerve sections from groups shown in Figure 3.1A, were collected 60 dpi immunostained for MBP (red) and DAPI (blue), and imaged at 20x. Normal sections are highly myelinated. Sections from vehicle-treated mice exhibit less myelination overall as well as regions completely absent of myelination and populated with clusters of DAPI positive cells (identified by white arrows) indicative of lesions. IndCl treated sections show significant increases in myelination compared to vehicle and very few unmyelinated regions, however clusters of DAPI positive cells (identified by dashed white arrows) remain. **B.** PLP-EGFP (green) optic nerve sections were immunostained for CD45 (red) and DAPI. Sections were imaged at 20x magnification with representative images shown. $CD45^+$ leukocytes are not evident in normal, however are abundant in vehicle, and minimally present in IndCl sections. PLP^+ OLs are abundant in normal, and depleted in vehicle but not IndCl sections. Insets show magnified $CD45^+$ and PLP^+ cells in normal, vehicle, and IndCl sections. **C.** Optic nerve sections were immunostained for GFAP (green) and DAPI. Sections from normal mice show some GFAP immunoreactivity with astrocytes aligned along the horizontal axis of the optic nerve. Sections from vehicle- and IndCl-treated mice have increased GFAP immunoreactivity with disruptions in the linear organization of astrocytes. **D.** Thy1-YFP (green) optic nerve sections from groups shown in Figure 1A, were collected 60 dpi and stained with DAPI. Sections were imaged at 40x magnification with representative images shown. Thy1-YFP axons show increased blebbing, swelling and transections in vehicle as compared to normal optic nerve sections. IndCl sections exhibit blebbing and swollen axons as well, but more coherent axons than vehicle. **E.** Quantification of all treatment groups shows significant decreases in MBP intensity, and numbers of PLP^+ OLs (**F.**) in the vehicle group compared to normal which is increased to baseline levels with IndCl treatment. **G.** Vehicle sections show significantly increased CD45 intensity, GFAP intensity (**H.**), and $Thy1^+$ axon blebs (**I.**) compared to normal. IndCl-treated sections show significantly decreased CD45 immunoreactivity, but not GFAP intensity or number of axon blebs compared to vehicle. $*P<0.05$, $**P<0.01$, $***P<0.001$ ordinary one-way ANOVA with Kruskal-Wallis multiple comparison test. Scale bar is 100 µm.

Ultrastructure analysis of optic nerve axons in normal, vehicle-treated and IndCl treated EAE groups.

To assess axon myelination integrity, ultrastructure EM analysis of the optic nerves was performed. All myelinated and nonmyelinated axons within a given field were used to assess mean ratio of inner axonal diameter to total outer diameter (g-ratio) (**Figure 3.5A-C**) was calculated. Out of all the optic nerve axons measured by EM, vehicle-treated mice showed increased numbers of nonmyelinated, 25 ± 4.6%, and thinly myelinated callosal fibers compared with only 3 ± 0.78% nonmyelinated axons in normal mice. Nonmyelinated axon numbers were decreased in Ind-Cl-treated mouse optic nerve sections to 13 ± 6%. The mean g-ratio of vehicle-treated mice (0.90 ± 0.12) was higher than in normal mice (0.86 ± 0.12), whereas g-ratios of Ind-Cl-treated groups (EAE+Ind-Cl, 0.87 ± 0.09 were lower than in the vehicle-treated group (**Figure 3.5A-C**).

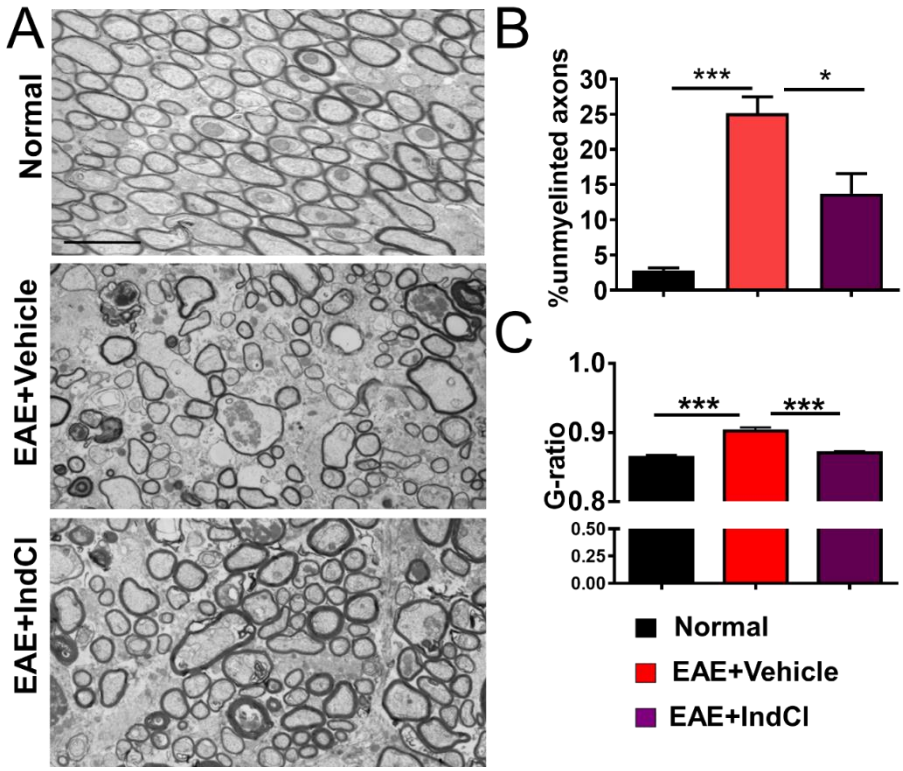

Figure 3.5: IndCl treatment improves myelination in the optic nerve of EAE mice. A. Electron micrographs of optic nerve from normal, vehicle and IndCl treatment groups collected 60 dpi are shown. Axon damage and demyelinated axons are present in EAE + vehicle sections. IndCl treated groups show increased numbers of myelinated axons and overall improvement of axon morphology compared to vehicle. **B**. Quantification of the number of unmyelinated axons reveals an 8-fold increase in vehicle compared to normal. Optic nerves from IndCl-treated mice show an approximately 45% decrease in the number of unmyelinated axons compared to vehicle. **C.** Calculated g-ratios are significantly increased in the vehicle group compared to normal. This effect is attenuated in the IndCl group, representative of increased axon myelination in the optic nerve. n=6 mice per group. *P<0.05, **P<0.01, ordinary one-way ANOVA with Kruskal-Wallis multiple comparison test. Scale bar is 2.5 µm.

EAE-induced increases in optic tract leukocytes, astrocytes and axon demyelination, but not axonal damage are attenuated by IndCl treatment.

Optic nerves from each eye leave the retina and travel toward the brain decussating at the optic chiasm. RGC axons within the optic nerve remain in the ipsilateral region of the chiasm and enter the brain via the ipsilateral optic tract or cross the chiasm and enter

on the contralateral side. In humans an estimated 53% of fibers cross to the contralateral hemisphere whereas in rodents, approximately 97% crossover is evident (Herrera et al., 2019; Kupfer et al., 1967). In the optic tract RGC axons remain heavily myelinated and are susceptible to EAE-induced inflammation, demyelination, and axon damage.

To assay EAE effects on axon myelination in the optic tract, brain sections corresponding to plates 43-45 of the Paxinos and Franklin brain atlas (**Figure 3.6A-i)** from Thy1-YFP mice were immunostained for MBP and imaged in the dorsal region of the optic tract (**Figure 3.6A-ii**) (Paxinos and Franklin, 2013). Optic tract sections showed significant decreases in MBP immunoreactivity as compared to normal control optic tract section. IndCl treatment attenuated the decrease in myelin intensity seen in EAE+vehicle groups (**Figure 3.6B, E**).

EAE effects on inflammation and astrocytic activation in the optic tract were assessed by immunostaining sections from Thy1-YFP mice for CD45 and GFAP, and imaged in the dorsal region of the optic tract. CD45 and GFAP staining intensities were significantly increased in vehicle groups compared to normal controls (**Figure 3.6B, E**). IndCl treatment during EAE decreased GFAP intensity with no change in CD45 intensity as compared to vehicle-treated mice.

To determine if RGC axonal degradation seen in optic nerve sections extended to the optic tract, sections from Thy1-YFP mice were imaged in the dorsal region of the optic tract. Axon fragmentation and blebbing was ubiquitous in sections from vehicle-treated

optic tract exons as compared to normal sections with coherent and intact $Thy1^+$ axons. Treatment with IndCl during showed increased axonal pathology similar to EAE+vehicle groups (**Figure 3.6D**). Quantification of the punctate "axon blebs" showed significant increases in vehicle-treated EAE groups which were not attenuated by IndCl treatmeent (**Figure 3.6H**).

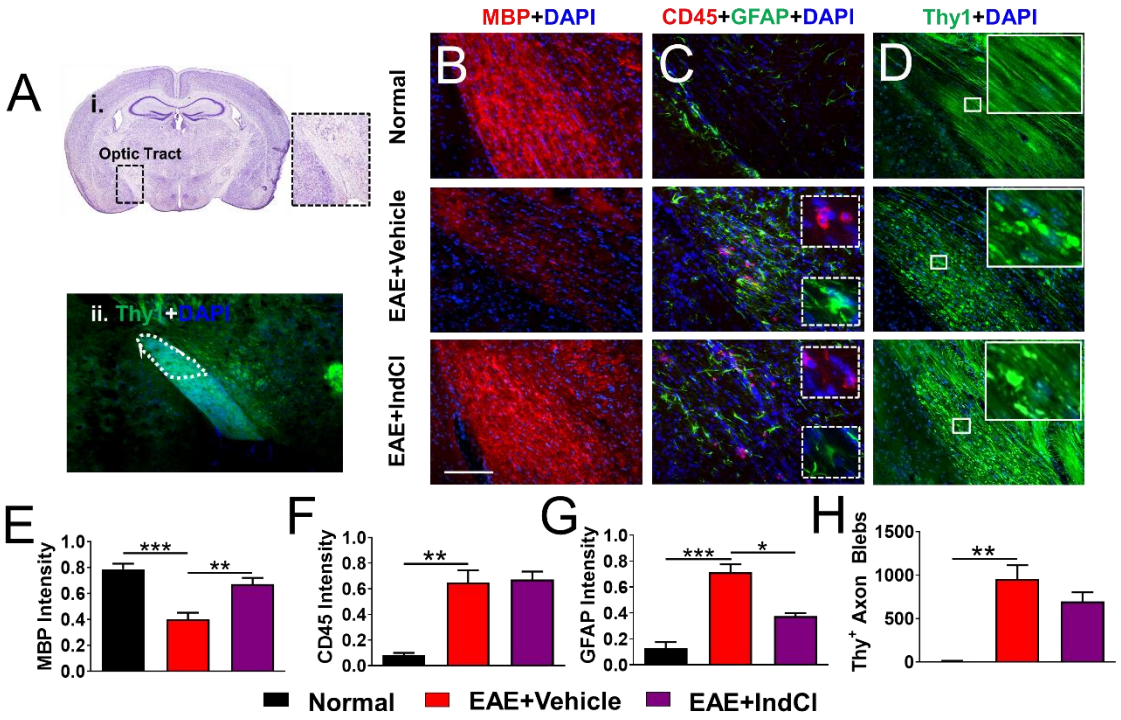

Figure 3.6: IndCl treatment ameliorates myelin loss and astrogliosis but not leukocytic infiltration in the optic tract of EAE mice. A. Reference image of Paxinos plate 43 depicting a Nissl-stained mouse coronal section(Paxinos and Franklin, 2013) (i). The area encompassed by the black dashed box highlights the location of the optic tract within the larger section. Ten times magnified image of the optic tract region in normal male Thy1-YFP mouse, with optic tract traced to highlight region of analysis (ii) **B.** Coronal sections containing optic tract from normal, vehicle-treated, and IndCl-treated EAE male Thy1-YFP (green) mice were collected 60 dpi. Sections were immunostained for MBP (red) and imaged at 20x magnification. MBP immunofluorescence is decreased in vehicle sections, an effect mitigated by IndCl treatment. **C.** Sections immunostained for CD45 (red), GFAP (green), and DAPI (blue) were imaged at 20x magnification. Vehicle-treated groups show increased CD45 and GFAP immunoreactivity compared to normal. IndCl groups show decreased GFAP but not CD45 immunofluorescence compared to vehicle. Insets show magnified $CD45^+$ cells (top) and $GFAP^+$ astrocytes (bottom) in vehicle and IndCl groups. **D.** Thy1-YFP sections were assessed for axonal integrity. Normal tissue shows coherent healthy axons however axon damage as indicated by axon fragmentation and swelling is evident in the optic tract of EAE vehicle-treated mice. Sections from IndCl-treated mice show a combination of fragmented swollen axons and intact axons. Insets show magnified images of $Thy1^+$ intact axons in normal, fragmented and swollen axons in vehicle, and a combination of fragmented and intact axons in IndCl groups. **E.** MBP staining intensity is significantly decreased in the vehicle group compared to normal but significantly increased in the IndCl group compared to vehicle. **F.** CD45 intensity is significantly increased in the vehicle group compared to normal, and not changed between vehicle and IndCl groups. **G.** GFAP staining intensity is significantly increased in vehicle compared to normal, however the IndCl group shows decreased staining intensity compared to vehicle. **H.** The number of $Thy1^+$ axon blebs is minimal in normal, significantly increased in vehicle but not attenuated in IndCl treatment groups. n=4 mice per group. *P<0.05, **P<0.01, *** P<0.001, ordinary one-way ANOVA with Kruskal-Wallis multiple comparison test. Scale bar is 100 µm.

EAE pathology in the dLGN is not significantly altered by IndCl treatment.

RGC axons from the retina project to a number of synaptic targets in the visual system, one of which is the LGN. In humans the LGN is composed of six distinct layers with interleaved koniocellular regions. Retinal projections synapse on specific layers depending on the originating eye, location in the retina and RGC type. In contrast, the mouse LGN is composed of three individual regions: the ventral LGN, intergeniculate nucleus, and dLGN. While the ventral and intergeniculate nuclei are also involved in the visual system specifically the efferent visual pathway, the primary target for the afferent visual system in the mouse is the dLGN. The dLGN is an important processing hub and relay station which sends and receives geniculo-cortical projections to the visual cortex where the final visual image is formed (Seabrook et al., 2017).

In order to evaluate the effect of EAE on the dLGN, coronal sections were obtained from Thy1-YFP mice, corresponding to plates 51 to 53 of the Paxinos and Franklin mouse brain atlas (**Figure 3.7A-i**)(Paxinos and Franklin, 2013). Sections were immunostained, then imaged at 40x magnification in four locations within the dLGN (**Figure 3.7A-ii**). Results from immunohistochemical analysis in each of the four regions were averaged for quantification.

Axon myelination in the dLGN was assessed in brain sections from various groups. Compared to normal sections which showed moderate myelination, MBP intensity from vehicle treated sections revealed decreased myelination with a small but non-significant increase in sections from IndCl-treated mice (**Figure 3.7B, D).**

Leukocyte assessment with CD45 immunoreactivity showed minimal presence in normal sections as compared to EAE+vehicle group (**Figure 3.7C, E)**. IndCl treatment did not change the increase in CD45 intensity as compared to vehicle-treated EAE group (**Figure 3.7E)**. Astrocyte activation was observed in EAE+vehicle group as compared to normal controls. However, IndCl treatment maintained the increase in astrocyte activation similar to EAE+vehicle group (**Figure 3.7F)**.

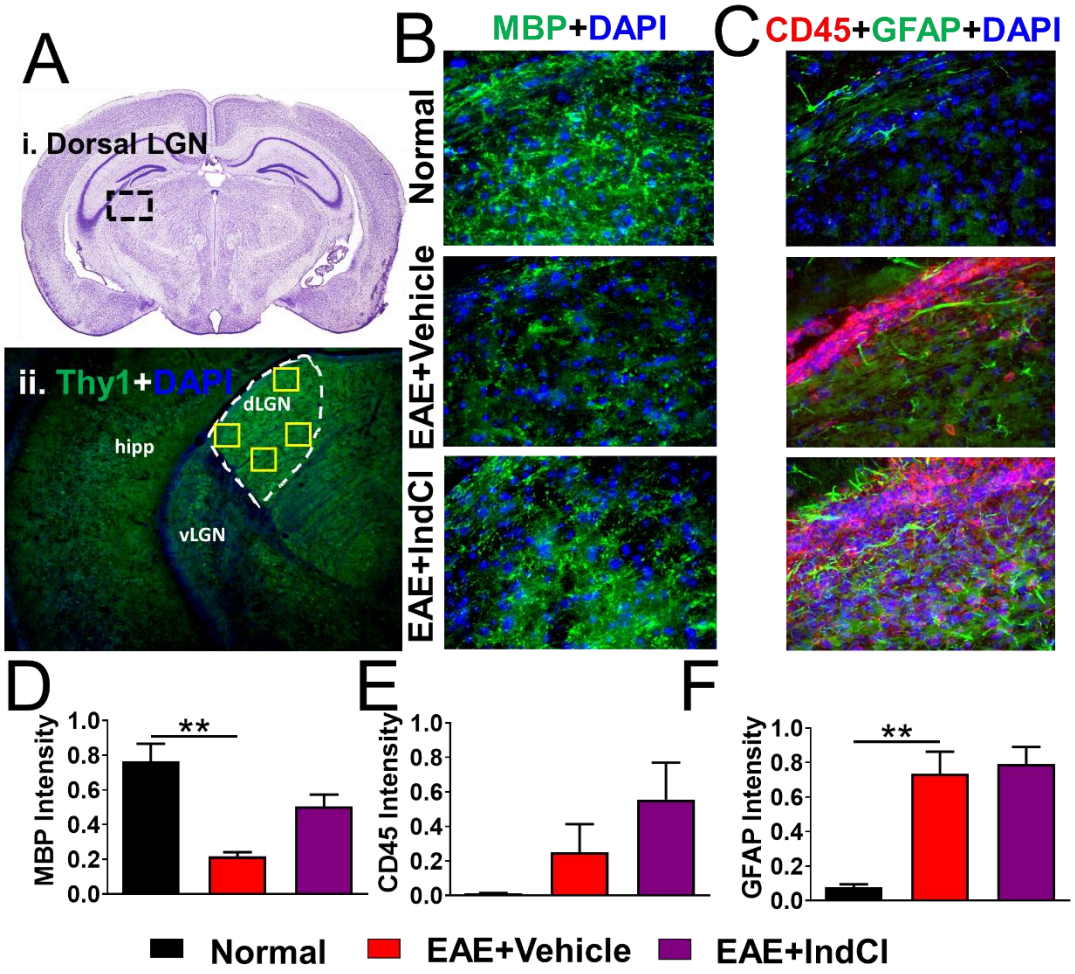

Figure 3.7: IndCl treatment improves myelin loss but not astrogliosis in the dLGN. A. Reference image of Paxinos plate 51 depicting a Nissl-stained mouse coronal section(Paxinos and Franklin, 2013) (i). The area encompassed by the black dashed box highlights the location of the dLGN within the larger section. Ten times magnified image of the LGN region in normal Thy1-YFP (green) male mouse section stained with MBP (red) and DAPI (blue), with dLGN traced to highlight region of analysis (ii). For immunohistochemical analysis four 40x images were taken in the areas denoted by the yellow boxes, analyzed individually, then averaged into one result for that mouse. **B.** Coronal sections containing dLGN were obtained from normal, vehicle-treated, and IndCl-treated Thy1-YFP male mice 60 dpi and stained for MBP (green). Decreased MBP immunoreactivity is evident in vehicle sections compared to normal, and is not significantly increased in the IndCl group. **C.** Normal sections stained for CD45 (red) and GFAP (green) show few $CD45^+$ cells, whereas vehicle and IndCl sections show large numbers of $CD45^+$ cells. GFAP immunoreactivity is minimal in normal sections but high in vehicle and IndCl sections. **D.** Quantified MBP staining shows a significant decrease in MBP intensity in vehicle sections compared to normal, which is not significantly changed in the IndCl group. **E.** Quantified CD45 staining shows trends of increasing intensity in vehicle mice compared to normal which do not reach significance. **F.** GFAP immunoreactivity is significantly increased in vehicle compared to normal, but IndCl treatment effects are not different from vehicle. n=4 mice per group. *P<0.05, **P<0.001, ordinary one-way ANOVA with Kruskal-Wallis multiple comparison test.

EAE-induced axon demyelination in V1

In mice and humans, the visual cortex is a major processing center for thalamocortical inputs. It synthesizes information provided by the anterior regions of the visual system described in this text, as well as other non-image forming areas and produces a final image in the brain. Furthermore, the visual cortex is highly myelinated and so, is particularly vulnerable to EAE-induced demyelination.

Axon myelination and neuronal changes were assessed in V1 of Thy1-YFP coronal sections corresponding to plates 52-54 (**Figure 3.8A-i**) (Paxinos and Franklin, 2013). Sections were analyzed in the demarcated region of interest which included layers two through six (**Figure 3.8A-ii**). V1 axons in normal control sections were highly myelinated in all layers analyzed but showed lower levels of myelination in more dorsal layers such as layer 2. EAE+vehicle V1 underwent significant axon demyelination as assessed by a decreased MBP mean intensity compared to normal group (**Figure 3.8B, D**). IndCl treatment during EAE, significantly attenuated myelin loss observed in vehicle sections by >6 fold (**Figure 3.8B, D)**.

Thalamocortical neurons in the LGN project to layer 4 and synapse on resident spiny stellate neurons of V1, as well as layers 5 and 6(Constantinople and Bruno, 2013). Spiny stellate neurons are thought to preprocess afferent visual information and transfer it to pyramidal neurons in layer 2-3 for further processing(Gilbert and Wiesel, 1979). Signals from layer 2-3 propagate to layer 5 neurons which drive the function of many efferent visual system nuclei, as well as extrastriate regions which further tune the visual

output(Gilbert and Wiesel, 1979). The complexity of visual processing occurring in layer 2-3 suggests that these pyramidal neurons contribute significantly to the formation of the final visual image.

Thy1-YFP mice express Thy1 in a subset of cortical pyramidal neurons(Porrero et al., 2010). In the B6.Cg-Tg(Thy1-YFP)16Jrs/J strain used for these studies, both layer 5 and layer 2/3 pyramidal neurons in the visual cortex expressed the fluorescent protein. To assess the effect of EAE on these layer 2-3 cells, $Thy1^+$ neurons were quantified in sections from all treatment groups. Normal sections showed significant numbers of $Thy1^+$ pyramidal neurons with intact apical dendrites (**Figure 3.8C**). Sections from EAE+vehicle groups did not show significant changes to the number of $Thy1^+$ cell bodies, however fewer apical dendrites were evident (**Figure 3.8C, E**). EAE+IndCl group did not show any difference in the number of $Thy1^+$ cell bodies compared to normal, but did show improvements in remaining apical dendrites.

PV positive interneurons regulate neuronal group firing and are important for maintaining spike timing in the visual cortex (Agetsuma et al., 2018). PV interneuron inactivation results in decreased synchrony of neuronal networks. To determine if EAE engendered changes in PV^+ neurons in the visual cortex, PV^+ neurons were imaged and counted between layers 2 and 5. No significant differences in the number of PV^+ cells were observed between groups (**Figure 3.8C, F**).

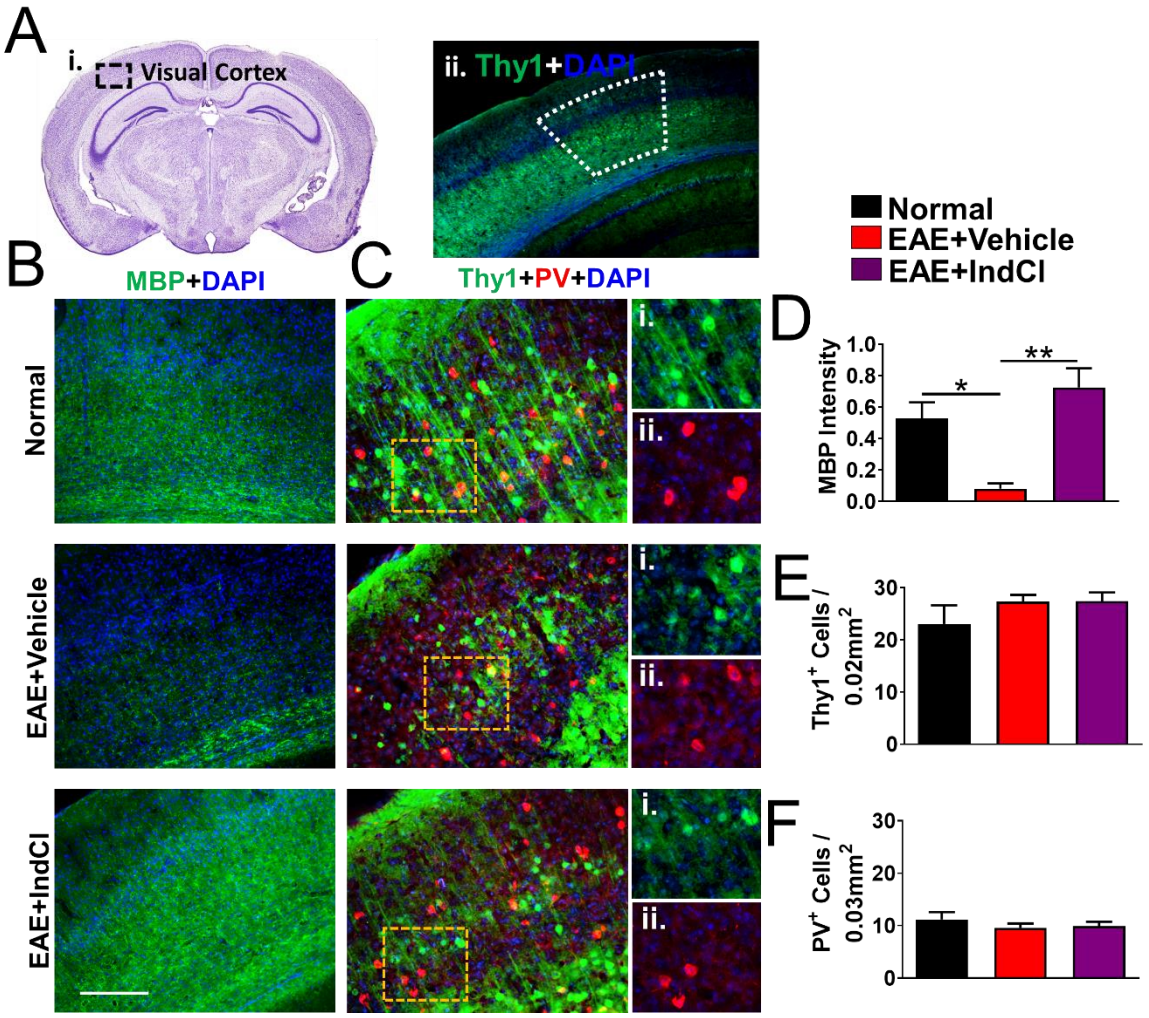

Figure 3.8: Treatment with IndCl attenuates myelin loss in the visual cortex of EAE mice A. Reference image of Paxinos plate 51 depicting a Nissl-stained mouse coronal section(Paxinos and Franklin, 2013) (i). The area encompassed by the black dashed box highlights the location of the visual cortex within the larger section. Four times magnified image of the visual cortex region in normal Thy1-YFP (green) male mouse section, with the region of analysis traced (ii). **B.** Coronal sections immunostained for MBP (green) in Figure 3.6D were imaged at 10x magnification and analyzed in the region of interest in (Aii) corresponding to V1 layers 2-6. Vehicle sections show decreased MBP immunoreactivity compared to normal. IndCl sections showed increased MBP staining compared to vehicle. **C.** Thy1-YFP coronal sections were immunostained for PV (red) and DAPI (blue) and imaged at 20x magnification in the visual cortex. Magnified split images showing Thy1 (i), and PV (ii) for all treatment groups, show no difference in $Thy1^+$ or PV^+ cell bodies between groups, however $Thy1^+$ axonal projections in vehicle sections are less numerous than in normal. **D.** MBP staining intensity was quantified in the visual cortex. Sections from vehicle mice show significantly lower MBP staining intensity compared to normal, which is increased in IndCl treated groups compared to vehicle. **E-F.** The number of PV^+ and $Thy1^+$ neurons was quantified in layers 2-3 of V1, but no significant differences between groups are observed. n=4 mice per group. *P<0.05, **P<0.001, ordinary one-way ANOVA with Kruskal-Wallis multiple comparison test. Scale bar is 200µm.

EAE induced decreases in retinal thickness as measured by OCT

OCT is an *in vivo* non-invasive imaging modality which can provide micron level resolution of thin structures such as the retina. It is commonly used in clinical and preclinical settings to resolve individual retinal layers and pathological changes to those layers. MS patients show decreased RNFL thickness in early and late stages of disease (Backner et al., 2019; Beck et al., 1992). Progressive decreases in RNFL thickness have also been demonstrated in the early stages of EAE(Hein et al., 2012).

Changes in retina layer thickness during EAE was assessed in a separate group of C57Bl/6 mice at 40dpi. The temporal retina was imaged approximately 0.3 mm lateral to the optic nerve (**Figure 3.9A**). Unbiased and accurate automatic segmentation of OCT images by system software was used to consistently demarcate the different layers of the retina and minimize bias (**Figure 3.9B**). The GCL and IPL were combined for analysis due to the difficulty associated with differentiating the two layers using OCT. Similar to OCT analysis for human patients, retina interneuron layers (IPL+INL) and PLs (ONL+PR) were grouped for simplicity (Al-Louzi et al., 2016; Walter et al., 2012).

Whole retina measurements did not show significant differences between normal and EAE treatment groups (**Figure 3.9C**). Vehicle-treated EAE mice showed a significant decrease in RNFL and the ONL+PR layer thickness as compared to normal that was not attenuated in EAE+IndCl treated group (**Figure 3.9C)**. Surprisingly, a significant increase in the RPE thickness of vehicle-treated EAE group compared to normal was observed.

GCL+IPL and INL+OPL layers were not significantly different between groups (**Figure 3.9**C).

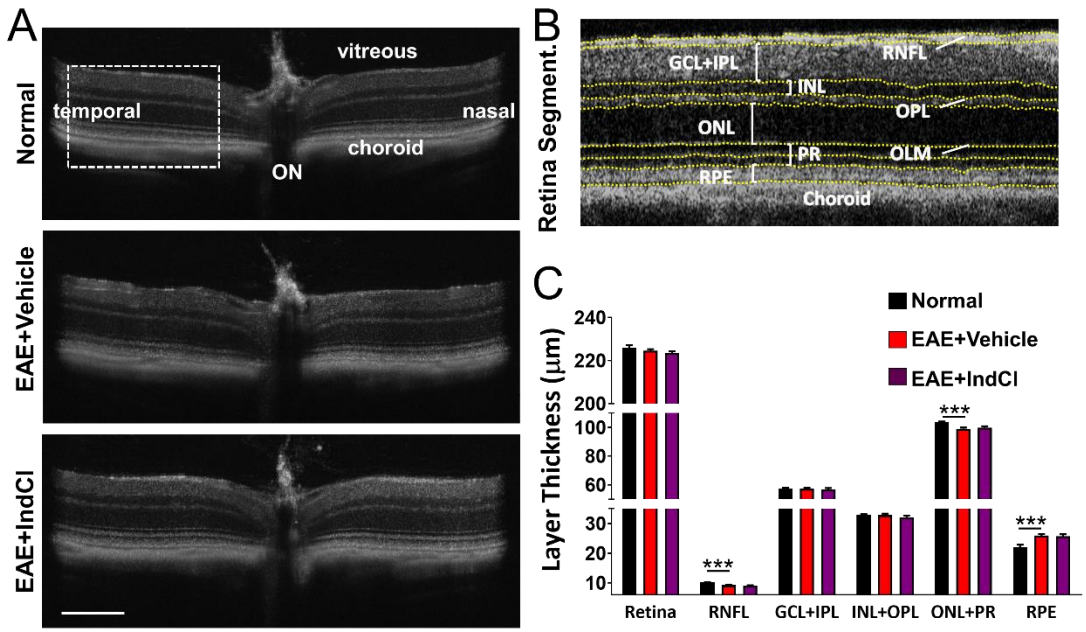

Figure 3.9: IndCl treatment does not affect thinning of the RNFL or changes in the thickness of posterior retinal layers during EAE. A. Representative OCT retina scans of C57Bl/6 normal, EAE + vehicle, and EAE + IndCl mice at 40 dpi, with optic nerve, choroid, vitreous, temporal and nasal regions demarcated in normal image. OCT scans show no obvious differences in retina morphology between treatment groups. B. The region indicated by the dashed rectangular box in (A), just lateral to the optic nerve, was imaged and segmented into individual layers to detect small changes in individual layer thicknesses that were not readily observable by eye. Automatic segmentation software demarcated and calculated individual layer thicknesses of the whole retina, RNFL, IPL, INL, OPL, ONL, the outer limiting membrane, the photoreceptor outer and inner segments (PR), RPE, and choroid. C. Quantification of retina layer thicknesses shows no differences in whole retina, combined GCL+IPL, or combined ONL+PR layers between groups. Vehicle mice show decreased RNFL and ONL+PR, but increased RPE thickness compared to normal. IndCl treated mice show no change in RNFL, ONL+PR, and RPE layer thickness compared to vehicle. n=14 eyes, 6 mice per group. *P<0.05, **P<0.01, ordinary one-way ANOVA with Kruskal-Wallis multiple comparison test. Scale bar is 200μm.

EAE induced changes in retina and visual pathway as measured by ERG and VEP

As demonstrated in the preceding histological analysis of afferent visual system nuclei and tracts, significant demyelination, inflammation, and axonal damage is present

in the visual pathway during EAE, some of which IndCl treatment attenuates. However, whether these effects result in functional changes to visual performance required further assessment. The ERG provides an assessment of retinal function and has been well characterized. The initial downward deflection of the voltage is identified as the a-wave and is thought to result from photoreceptor firing, while the fast upward deflection is identified as the b-wave and is generated by some retinal interneuron subtypes, Müller glia, and RGC firing (Brown, 1968; Miller and Dowling, 1970; Smith et al., 2014). When mice are dark-adapted, ERG and VEP responses are primarily driven by rod pathways (Ridder Iii and Nusinowitz, 2006).

To characterize the functional consequence of retinal pathology during EAE, retinal function in mice was assessed by recording ERGs in live, anesthetized, and dark-adapted C57Bl/6 mice at 40 dpi. ERG traces from normal mice show a characteristic downward deflection of the a-wave of about 200µV in amplitude, then an immediate ~500µV increase in amplitude characteristic of the b-wave, followed by a gradual return to baseline (**Figure 3.10A**). Vehicle treated EAE mice show similar ERG a-wave amplitudes, latencies, and b-wave latencies compared to normal, but a significant decrease in b-wave amplitudes (**Figure 3.10B-D**). IndCl treated EAE mice did not show any significant differences in ERG parameters compared to vehicle.

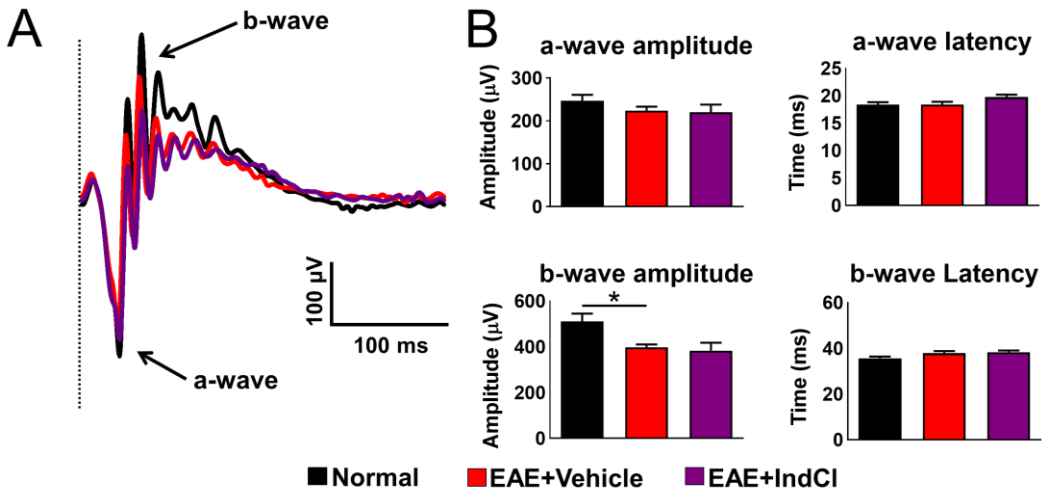

Figure 3.10: EAE mice show few improvements in retina function with IndCl treatment as measured by ERGs. A. Retina function in female C57Bl/6 mice was assessed by recording ERGs from normal, EAE + vehicle, and EAE+ IndCl mice at 40 dpi. Recording silver thread electrodes were placed on the cornea, reference needle electrodes in the snout, and a ground needle electrode in the tail. Sample ERG traces from treatment groups are shown with a-wave and b-wave peaks demarcated by the black arrows. **B.** No significant changes in a-wave amplitudes, a-wave latencies or b-wave latencies are observed between groups. Retinas from vehicle-treated mice show decreased b-wave amplitudes compared to normal controls, and IndCl treatment does not change this effect. *P<0.05, **P<0.001, ordinary one-way ANOVA with Kruskal-Wallis multiple comparison test.

The VEP is less characterized than the ERG and is accepted to be a assessment of afferent visual function as a whole. Thus, dysfunction in any part of the visual system affects recorded VEPs (Ridder Iii and Nusinowitz, 2006). VEP traces have an initial upward deflection described as the P1 peak, followed by a sharp downward deflection described as the N2 peak, and a return to baseline. Amplitude changes are primarily caused by axonal damage neuronal dysfunction (Pastare et al., 2013), whereas latency changes are thought to arise from primarily demyelinating events(You et al., 2011).

Functional effects of visual pathway pathology were measured by recording VEPs using subdermal electrodes resting on the skull above the visual cortex. In normal mice, VEPs showed an approximately 30μV positive deflection, then fast 50μV decrease in voltage, followed by a return to baseline (**Figure 3.11A**). Vehicle-treated EAE mice showed significant 50% decreases in P1 and N2 amplitudes compared to normal, but no change in latency (**Figure 3.11B**). IndCl treatment during EAE had minimal effects on VEP parameters, P1 and N2 amplitude and N2 latency, as compared to EAE+ vehicle. However, P1 latency was significantly decreased in EAE+IndCl treated mice as compared to EAE+vehicle mice.

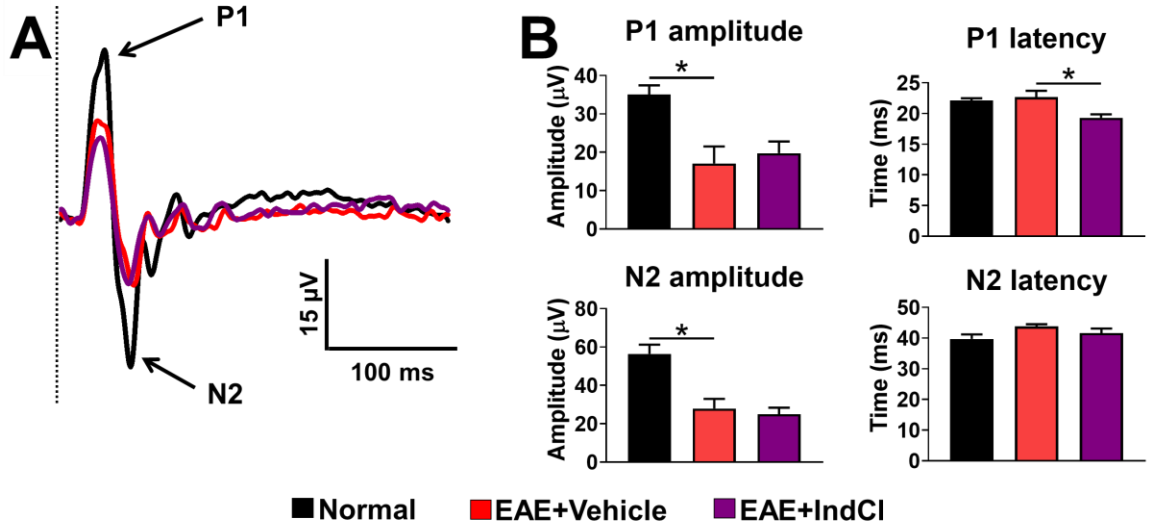

Figure 3.11: EAE mice exhibit severe deficits in visual function as measured by VEPs, which are not changed by IndCl treatment. A. Visual function in female EAE mice was assessed by recording VEPs from groups described in Figure 3.10A. Recording needle electrodes were placed subdermally above the visual cortex, reference needle electrodes in the snout, and a ground needle electrode in the tail. Sample VEP traces from all treatment groups are shown with P1 and N2 components indicated by the black arrows **B.** P1 and N2 amplitudes are significantly decreased in vehicle compared to normal by approximately 50%, an effect not changed by IndCl treatment. Vehicle mouse P1 and N2 latencies are not significantly different from normal, however IndCl treatment reduces P1 latency compared to vehicle. *n*=8 eyes, 4 mice per group. **P*<0.05, ***P*<0.001, ordinary one-way ANOVA with Kruskal-Wallis multiple comparison test.

Discussion

This is the first study to assess the therapeutic potential of the ERβ ligand IndCl for attenuating visual pathway pathology in EAE. Our results show extensive demyelination, axon damage, and inflammation in visual pathway white matter tracts with corresponding functional deficits during EAE. Similar to previously published data on the remyelinating and neuroprotective properties of ERβ ligands within the CNS (Khalaj et al., 2013; Khalaj et al., 2016; Moore et al., 2014b), IndCl treatment attenuated neurodegeneration in the retina, and improved myelination in almost all regions surveyed, but was not immunosuppressive (**Figure 3.12**). These effects were not sufficient to significantly improve EAE-induced morphological changes in OCTs or functional outcomes in ERGs.

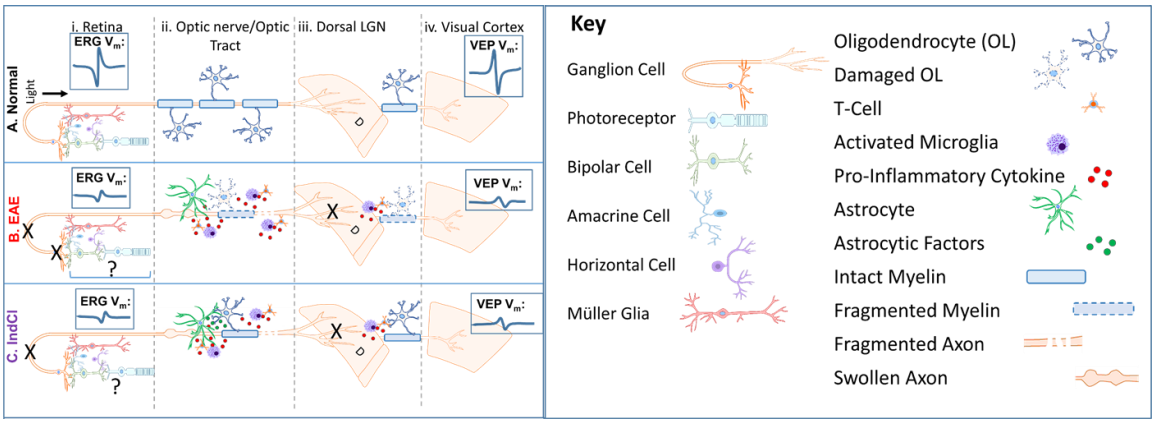

Figure 3.12: Model of visual pathway dysfunction and IndCl effects on visual system during EAE. A. Schematic depicting normal visual pathway. (i) Photoreceptors form synapses with bipolar cells which then synapse onto RGCs. Photoreceptor/bipolar cell and bipolar cell/RGC synaptic transmission is modulated by amacrine and horizontal cells. Müller glia span the neural portion of the retina and interact with the neural retina. ERGs amplitudes are robust and timely. (ii) Mature OLs myelinate most RGC axons in the optic nerve and optic tract thereby providing trophic support and improving axon conduction. (iii) RGC axon terminals form synapses with thalamocortical neurons in the dLGN. Myelinated thalamocortical neurons in the dLGN send projections to V1. (iv) With no disruption of the afferent visual system, VEP amplitudes are robust and timely. **B.** Schematic depicting EAE visual pathway. (i) In EAE, RGC cell bodies and their axons comprising the retinal nerve fiber layer are damaged. ERG amplitudes are decreased, but response latencies remain similar to normal. EAE-induced effects on photoreceptors, retinal interneurons, and Müller glia effects require further study. (ii) Breakdown of the blood-brain barrier during EAE results in leukocytic infiltration into the optic nerve and optic tract. The inflammatory milieu including pro-inflammatory factors from lymphocytes macrophages, and other immune cells leads to astrocytic activation, myelin loss, axonal swelling and axonal degradation. (iii) Axonal degradation in anterior regions of the visual pathway likely leads to a loss of synaptic input in the dLGN. Leukocytic infiltration into the dLGN leads to a loss of myelination. Thalamocortical projection neurons of the dLGN are likely demyelinated decreasing signal transmission to the visual cortex. (iv) Significant defects in the anterior portion of the visual pathway, and a loss of myelination in the visual cortex lead to decreased VEP amplitudes. **C.** Schematic depicting proposed effects of IndCl on the EAE visual pathway. (i) IndCl treatment protects RGC somas but does not affect intraretinal RGC axons comprising the retinal nerve fiber layer. ERG amplitudes are not improved with treatment. IndCl effects on photoreceptors, retinal interneurons, and Müller glia need further investigation. (ii) IndCl treatment results in partial decreases in leukocytic presence in the optic nerve, and astrocytic activation in the optic tract. IndCl also induces astrocytic production of the neuroprotective chemokine CXCL1 and decreases IFN-γ production, thus promoting OL recruitment, survival and differentiation(Karim et al., 2018a). This may be the mechanism by which IndCl promotes myelination in the optic nerve and optic tract. This effect is not sufficient to prevent RGC axon degradation. (iii) Persistent axonal damage in anterior visual pathway, even with robust remyelination, likely leads to a loss of synaptic input to the dLGN. Minimal remyelination in the dLGN indicates that EAE induced deficits to thalamocortical projections are likely not improved by IndCl treatment. (iv) Although the visual cortex and anterior regions of the visual pathway show improved myelination with IndCl treatments, significant axonal damage results in no improvements in VEP amplitudes and minimal effects to VEP latencies.

Retina

IndCl therapeutic treatment significantly attenuated RGC loss indicating a neuroprotective role in the retina. Because these RGCs expressed ERβ, it is possible that this effect was mediated either directly through ligand binding to RGC ERβs or indirectly through binding to estrogen receptors on other cell types such as microglia or astrocytes. Although few other studies have evaluated the effect of ERβ-specific agonists on RGC health, many studies have looked at estrogenic compounds which target multiple ER types concurrently. For instance, estrogen treatment is well accepted to have neuroprotective effects on RGC survival in animal models of glaucoma and optic nerve transection (Nakazawa et al., 2006; Prokai-Tatrai et al., 2013; Russo et al., 2008). These effects have been shown to be partially mediated by reduction of mitochondrial-induced oxidative stress in response to optic nerve axon damage(Kanamori et al., 2010a; Li et al., 2013; Li et al., 2016; Lieven et al., 2006; Wang et al., 2015). Estrogenic compounds including ERβ-specific and ERα-specific agents have also been shown to exert anti-oxidative and anti-inflammatory effects through indirect mechanisms associated with astrocyte and microglial signaling during inflammatory challenge with lipopolysaccharide(Bruce-Keller et al., 2000; Cerciat et al., 2010; Kipp et al., 2007; Smith et al., 2011). Furthermore, estradiol can act directly on astrocytes to induce release of neuroprotective agents and growth factors(Arevalo et al., 2010; Azcoitia et al., 2010). Thus IndCl-induced RGC survival within the retina was likely a result of various neuroprotective mechanism conferred by the ERβ ligand.

Surprisingly RGC protection by IndCl did not translate to RGC axonal survival within the RNFL. This may partially be because IndCl treatment did not improve axonal health in the optic nerve and optic tract, even in the presence of robust OL survival and myelination. Retrograde axonal degradation into the retina and subsequent thinning of the RNFL is a well-accepted effect of optic nerve damage(Huang et al., 2018; Kanamori et al., 2010b; Nagata et al., 2009), and is characteristic of our observations in the EAE optic nerve. Although IndCl effected partial changes to microglial and astrocytic activation in the optic nerve and tract, these cell types remained relatively active. Activated microglia and astrocytes have been implicated in optic nerve degeneration in EAE, and in mouse models of glaucoma (Feliciano-Sanchez et al., 2019; Mabuchi et al., 2003; Manogaran et al., 2018; May and Mittag, 2006; Yuan and Neufeld, 2001). Thus, it is likely that although RGC bodies were protected in the retina, the RNFL remained under significant stress from ongoing RGC axonal degradation, inflammation, and astrogliosis in the optic nerve and optic tract, and thus was not affected by IndCl treatment. However further studies are needed to elucidate IndCl mechanisms of action on RGC and RGC axon survival.

Immunomodulation

IndCl did not extensively suppress leukocytic presence and astrocyte reactivity during EAE, however it did exert moderate changes in select areas of the visual pathway, indicating an immunomodulatory profile. We have previously shown that although IndCl may not greatly modify the extent of leukocytic infiltration into the CNS it decreases the production of pro-inflammatory cytokines by peripheral leukocytes such as TNFα, IFNγ

and CXCL10, while increasing production of anti-inflammatory cytokines like CXCL1 (Karim et al., 2018b; Moore et al., 2014b). Over-expression of IFNγ exacerbates EAE by driving T-cells to a pro-inflammatory phenotype, enhancing cytokine and chemokine secretion (Imitola et al., 2005), promoting OL death and inhibiting myelination(Balabanov et al., 2006). Furthermore, intraocular injection of IFNγ increases latency measurements of VEPs while exerting subtle changes in myelinated visual system axons(Brosnan et al., 1989). CXCL10 is an IFNγ-inducible T cell and monocyte chemoattractant that promotes neuronal(Sui et al., 2006) and OL apoptosis(Tirotta et al., 2011), while CXCL1 is a neutrophil chemoattractant which attenuates EAE severity, axonal degeneration and improves myelination(Omari et al., 2009). It is possible that similar to our previously reported effects in the spinal cord, IndCl treatment attenuated IFNγ and CXCL10 production while promoting CXCL1 production within the visual system, thus mitigating OL death and myelin loss (Karim et al., 2018b). Taken together, this indicates that therapeutic IndCl treatment may have promoted remyelination partially by exerting immunomodulatory effects on infiltrating and resident leukocytes, as well as astrocytes. However, further research is necessary to evaluate these hypotheses.

Remyelination

The autoimmune profile of MS and EAE have long supported the importance of immunomodulation in MS therapies, a requirement potentially addressed by IndCl. However, there are a number of immunomodulatory MS therapies which, while effective for managing MS in relapsing-remitting stages of the disease, are often inadequate in

preventing progression to chronic neurodegenerative stages(2001; Kapoor et al., 2018; Ontaneda et al., 2017; Panitch et al., 2004; Wolinsky et al., 2007). Thus, immunomodulatory *remyelinating* therapies have been increasingly studied.

In the current studies, IndCl was shown to remyelinate almost all white matter tracts in the afferent visual pathway. Furthermore, we have previously demonstrated the remyelinating capability of IndCl and other ERβ ligands in the corpus callosum and spinal cord(Karim et al., 2018b; Karim et al., 2019a; Moore et al., 2014b). IndCl-induced remyelination in the corpus callosum and spinal cord was also associated with improved functional recovery in the motor system. However, in the visual system, EAE-induced ERG and VEP functional deficits were not attenuated with treatment. This lack of functional efficacy in the visual pathway was associated with ongoing axonal damage which was similarly not improved with IndCl.

A possible reason for differential functional effects in motor and visual systems is the timing of therapeutic treatment. In both studies, IndCl treatment is administered therapeutically at peak clinical disease, between 16 and 24 dpi. This is an ideal therapeutic window for attenuating motor dysfunction, but perhaps not for visual deficits. Studies in other animal models for EAE have shown, that inflammatory infiltration to visual pathway white matter tracts occurs as early as 7-8 dpi, demyelination 1-2 days after, and axonal degeneration and neuron loss at 14 dpi, all prior to quantifiable motor deficits (Hu et al., 2006; Shindler et al., 2008). Furthermore, neurodegenerative damage in visual pathway nuclei and tracts is quite severe and often has trans-synaptic anterograde and retrograde

effects. For instance, optic nerve transection in rodents not only results in upstream RGC death(Berkelaar et al., 1994), but also causes apoptosis of synaptic targets in the LGN(You et al., 2012). Similarly, ablation of a region in the visual cortex induces apoptosis of geniculocortical projection neurons(Al-Abdulla and Martin, 2002) as well as RGC loss (Cowey, 1974) in animal models, while stroke-induced visual cortex damage in humans causes progressive thinning of the RNFL (Jindahra et al., 2012). Thus, damage to any visual pathway area has significant upstream and downstream neurodegenerative effects. Given this disease profile, irrecoverable neuronal damage had likely occurred between the optic tract, LGN, and visual cortex prior to IndCl treatment start, thus rendering improvements in VEPs and ERGs relatively difficult to attain.

Studies which have assessed the capability of other remyelinating therapeutics to attenuate functional deficits in VEPs have also shown meager improvements with therapeutic treatment in animal models. Similar to IndCl (Karim et al., 2018b; Moore et al., 2014b; Young et al., 2012), the oral sphingosine 1-phosphate receptor modulator, fingolimod, was shown to improve EAE mediated paralysis, decrease demyelination in the brain and spinal cord, and improve conduction in the CNS with therapeutic treatment(Balatoni et al., 2007). However, although prophylactic fingolimod improved VEP latencies, therapeutic treatment resulted in no identifiable recovery during EAE. Similar to IndCl, fingolimod, glatiramer acetate, and interferon β-1b, other therapeutics currently approved for MS treatment, have been shown to have remyelinating effects(Aharoni et al., 2008; Miron et al., 2010; Njenga et al., 2000) which do not translate to significant improvements in VEPs in EAE.

Studies in humans give conflicting reports on the efficacy of currently approved MS drugs for alleviating VEP deficits in MS patients. Glatiramer acetate(Major et al., 2013) and Interferon (IFN) β-1a(Liscic and Brecelj, 2004) show no improvement in VEPs, while IFN β-1b(Anlar et al., 2003) and Natalizumab(Meuth et al., 2011) attenuate visual dysfunction in the relapsing remitting form of MS. Some studies have shown improvements in VEPs with Mitoxantrone(Hobom et al., 2004) and 4-aminopyridine treatment(Jones et al., 1983), however it is unclear which patients in those studies had chronic progressive and which had relapsing remitting MS. It is possible that the poor improvements in VEPs measured in animal models and the conflicting therapeutic effects reported in MS patients may be due to variable severity of visual pathway neuronal and axonal pathology occurring prior to treatment start.

In this study, we established a preclinical drug assessment paradigm capable of screening therapeutics for functional efficacy, remyelinating and neuroprotective potential in the visual system. Because visual pathway dysfunction has significant detrimental effects to the quality of life experienced by MS patients, understanding the pathophysiology of the visual pathway in demyelinating disease is vital to therapeutic development. Furthermore, correlating minimally invasive functional assessments to pathological changes in the CNS during treatment has the potential to minimize drug discovery time, and improve treatment procedures for patients. In this spirit, we assessed the efficacy of IndCl, and demonstrated that IndCl had remyelinating effects across the visual system, but did not attenuate axon degradation nor incur functionally relevant improvements. We hypothesize that this lack of efficacy results from missing the critical

therapeutic window for improving visual function. Determining this critical window is crucial for improving visual outcomes in MS. Thus, there is a need for longitudinal studies of visual pathway pathology and axon damage in MS and its animal models.

Chapter 4: Posterior visual pathway pathology is a significant aspect of EAE pathophysiology.

4.1 Introduction

The visual pathway is highly susceptible to MS induced neurodegenerative events, partially due to its highly myelinated nature. Visual pathway pathology is commonly assessed in MS patients, using *in vivo* techniques such as MRI, OCT, visual acuity tests, ERGs, and VEPs (Backner and Levin, 2018; Balcer et al., 2017; Graham and Klistorner, 2017; Kuchling et al., 2017; Monsalve et al., 2018). However, although *in vivo* assays of structural changes and functional deficits provide significant insights into disease progression within the visual pathway, they cannot be used to probe the cellular and molecular changes underlying macroscopic pathology. Furthermore, because no highly specific biomarker for MS has been identified, patients are primarily diagnosed with MS after significant motor, visual, or cognitive deficits separated in space and time have appeared (McDonald et al., 2001; Poser and Brinar, 2004; Solomon and Corboy, 2017). Thus, it is currently impossible to glean early information about the onset and development of MS visual pathology. In contrast, post-mortem histological assays of MS patients, may allow for the assessment cellular and molecular damage in the visual system, however only at the time of death(Evangelou et al., 2001; Kerrison et al., 1994).

The use of animal models seeks to counter some of these disadvantages, and allows for longitudinal assessments of visual pathway pathology before disease onset and throughout disease progression. Importantly, they allow the evaluation of structural

changes and functional deficits at the macroscopic, cellular, and molecular level. However, although there is significant evidence to indicate extensive posterior visual system (optic tract, LGN and V1) pathology in MS patients, most longitudinal studies in the visual system using animal models have been in the retina and optic nerve, anterior compartments of the visual system.

Specifically, MS patients present with significant decreases in LGN and occipital lobe volume, as well as lesions in in the optic radiations(Balk et al., 2015; Gabilondo et al., 2014; Gabilondo et al., 2017; Papadopoulou et al., 2019; Shen et al., 2019). However, there has only been one study by Araújo and colleagues assessing posterior visual system pathology in the CPZ demyelination animal model for MS (Araujo et al., 2017), and another in EAE looking at the occipital lobe(Diem et al., 2008). This especially surprising because a number of studies in animal models correlate anterior visual pathology with deficits in VEPs or visual functional tests such as visual acuity, and optokinetic nystagmus (Arezzo et al., 1988; Castoldi et al., 2019; Gambi et al., 1987; Henderson et al., 2008; Larabee et al., 2016; Lin et al., 2014; Nishioka et al., 2017). VEPs are recorded from V1 and provide an assessment of visual deficits throughout the anterior *and* posterior afferent visual pathway (Creel, 1995a). Similarly, evaluations of visual cognition rely on the function of *all* nuclei and tracts within the afferent visual system, and a number within the efferent system. Thus, studies investigating longitudinal visual pathway pathology in animal models for MS, specifically within the posterior visual system, are crucial.

The previous chapter discussed assessing anterior and posterior visual pathway dysfunction in the EAE mouse model of MS, and the effectiveness of treatment with a

potent remyelinating agent for attenuating visual functional deficits. Therapeutic treatment with the remyelinating agent IndCl starting at peak EAE disease, although robustly successful in remyelinating almost all white matter tracts in the afferent visual pathway, did not exert any functional improvements. This was in sharp contrast to its efficacy in improving motor function(Karim et al., 2019a; Moore et al., 2014b). The differences between the time course of motor degeneration (significant motor dysfunction is observed 15 to 21 dpi) and visual pathology (occurring between 7 to 14 dpi) indicate that treatment with IndCl at peak disease may have missed a critical therapeutic window for attenuation of visual dysfunction.

In order to investigate EAE-induced damage to the posterior visual system, and to identify potential therapeutic windows, we assessed longitudinal posterior visual pathway pathology in EAE. Demyelination, axon damage and functional deficits were observed in the EAE model beginning as early as 15 dpi. However, axon damage was not observed to be severe until peak disease around 27dpi. This indicated that a critical therapeutic window for IndCl treatment in EAE may exist soon after disease onset and at maximum, before peak clinical disease.

4.2 Methods

Twelve 8-12-week-old Thy1-YFP and PLP-EGFP male mice on a C57Bl/6 background were induced with EAE as has been described(Hasselmann et al., 2017a). EAE disease onset occurred between 9 and 12 dpi, and reached peak severity between 20 and 23dpi, after which point clinical disease was slightly attenuated from a score of 3 at peak disease to between 2 and 3 throughout late disease and euthanasia at 47 dpi (**Figure 4.1A**). Mice were handled daily to determine clinical scores, and if necessary, to palpate bladders or inject saline for hydration. Mice underwent *in vivo* ERGs and VEPs at 8-9 dpi, 21dpi, and 40 dpi, and OCT at 13dpi, 20dpi and 38dpi (**Figure 4.1B**). Four EAE mice were perfused for IHC at 3 different timepoints: 15 dpi, 26 dpi, and 47dpi. Ten PLP-eGFP and four Thy1-YFP mice served as controls and were not euthanized for IHC until experiment end.

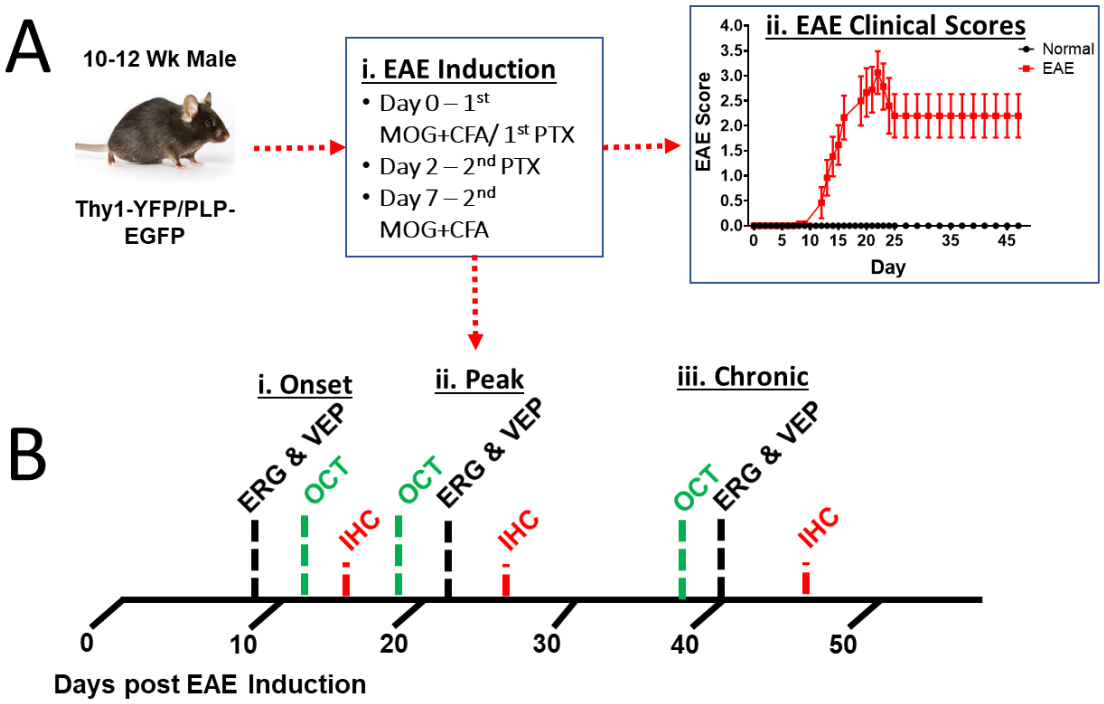

Figure 4.1: Experimental design for longitudinal assessment of visual pathway pathology in EAE. A. EAE was induced in 12-week-old male Thy1-YFP and PLP-eGFP mice with C57Bl/6 background. EAE induction involved initial immunization with MOG 35-55 peptide in CFA, IP injection of PTX on day 0, a second PTx injection at 2 dpi, and a final MOG+CFA immunization at 7dpi (i). EAE clinical scores (red) show disease onset occurring between 9 and 12dpi, peak disease between 20 and 23dpi, and slight decreases to average clinical score in the chronic disease stage between 25dpi and euthanasia at 47 dpi (ii). Clinical scores of normal mice (black) remain 0 through entirety of experiment. **B.** After EAE induction, *in vivo* visual assessments were performed around disease onset (i), peak disease (ii), and chronic disease stages (iii). ERGs and VEPs (black) were performed at 8-9 dpi, 21dpi, and 40 dpi, and OCT (green) at 13dpi, 20dpi and 38dpi. Four mice per timepoint were euthanized for IHC (red) just after onset (i), peak disease (ii) and late disease (iii). Ten PLP-eGFP and four Thy1-YFP mice served as controls and were not euthanized for IHC until experiment end.

4.3 Results

Posterior visual system damage is a key feature of MS pathophysiology. However, to date there have been very few investigations into posterior visual pathway structures, such as the optic tract, LGN, and visual cortex in EAE animal models. In the current work we investigated EAE-induced visual pathway demyelination, inflammation and neurodegeneration at onset, peak disease, and chronic disease stages using IHC. We then performed *in vivo* translationally relevant assays of retinal pathology using OCT, and visual pathway function using ERGs and VEPs.

EAE induces early demyelination and OL loss the optic tract.

The optic tract is an important white matter structure of the afferent visual pathway by which RGC axons first enter the brain after decussation at the optic chiasm. In the optic tract, RGC axons are heavily myelinated and are susceptible to EAE-induced demyelination and OL death.

To characterize EAE-induced effects on myelin and OL loss, coronal sections containing the optic tract were obtained from normal, and EAE mice at 15 dpi, 26 dpi, and 47 dpi. Sections were immunostained for MBP, and CC1, a mature myelinating OL marker, then co-stained with DAPI. Normal sections showed robust myelination in the optic tract and adjacent hypothalamus but minimal immunoreactivity observed in the adjacent amygdala (**Figure 4.2A**). Sections from EAE mice showed decreased myelination in the optic tract at all timepoints after EAE induction, and very little MBP immunoreactivity in adjacent structures. A large number of $CC1^+$ $DAPI^+$ mature myelinating OLs were

observed in the optic tract of normal mice, however in EAE sections, very few immunoreactive OLs were identified (**Figure 4.2B**). Quantification of MBP percent area showed near significant EAE-induced decreases in optic tract myelination compared to normal at 15dpi ($p=0.0549$). These decreases became significant at 26 and 47dpi (**Figure 4.2C**). $CC1^+$ OL numbers were significantly depleted by at least four-fold at all EAE timepoints compared to normal controls (**Figure 4.2D**).

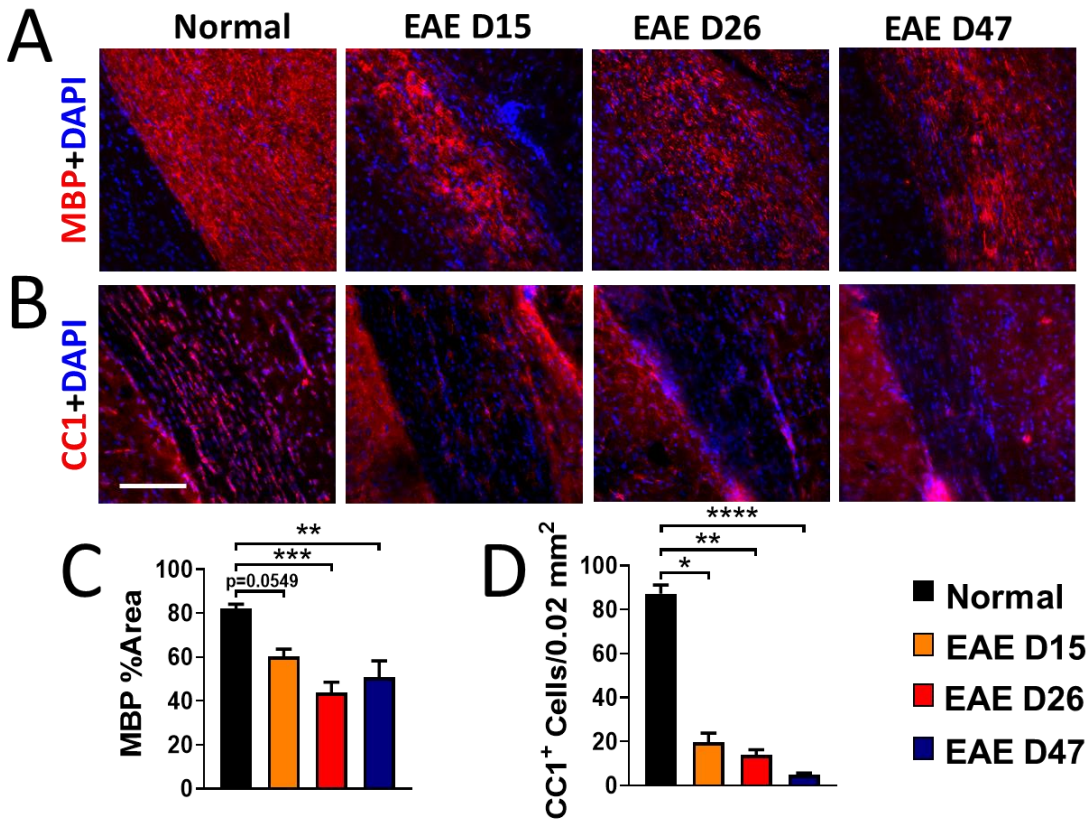

Figure 4.2: The optic tract exhibits significant demyelination and OL loss early in EAE and throughout EAE progression. A. Coronal sections containing the optic tract were obtained from normal and EAE Thy1-YFP transgenic mice at 15dpi (yellow), 26dpi (red), and 47dpi (navy blue). Sections were stained for MBP (red), co-stained for DAPI (blue) and imaged at 20x magnification. Optic tract and adjacent white matter areas show decreased myelination at 15dpi, 26dpi, and 47 dpi. **B.** Coronal optic tract sections were stained for CC1 (red), co-stained for DAPI, and imaged at 20x. Significant CC1 immunoreactivity is observed in normal sections with CC1 positive cells exhibiting cytosolic staining. **C.** Percent area of MBP staining was quantified in sections from normal and EAE groups. Decreased MBP area is observed at all timepoints but is only significant at 26dpi and 47dpi. **D.** Cell counts of $CC1^{+}DAPI^{+}$ cells reveal significant and greater than 4-fold decreases in the number of mature myelinating OLs at all timepoints. n=4 mice per group. *P<0.05, **P<0.01, *** P<0.001, ****P<0.0001, ordinary one-way ANOVA with Kruskal-Wallis multiple comparison test. Scale bar is 100µm.

Inflammation, astrogliosis and axonal damage are most prominent during peak and chronic disease stages in the optic tracts of EAE mice.

Microglia and macrophages accumulate in regions undergoing active demyelination and neurodegeneration in MS and EAE (ESIRI and READING, 1987; Ferguson et al., 1997; Kipp et al., 2017; Prineas et al., 2001). There they may amplify dysfunctional signals from CNS or immune system cells and produce a number of pro-inflammatory factors which can exacerbate myelin loss and axon damage (Carson, 2002). Astrocytes respond to CNS injury through astrogliosis, a number of changes which can include increases in the number of resident astrocytes and changes to morphology and molecular expression(Sofroniew, 2009). These effects are often associated with blood-brain barrier compromise, production of pro-inflammatory cytokines and chemokines, enhanced neuroinflammation, and scar formation in MS and EAE(Lopes Pinheiro et al., 2016).

To evaluate the progression microglial activation, astrogliosis and axonal damage in the optic tract during EAE, coronal sections containing the optic tract were obtained from Thy1-YFP transgenic mice and immunostained for Iba1 and GFAP, then co-stained for DAPI. Normal sections showed some Iba1 and GFAP immunoreactivity indicative of resident non-reactive microglia and astrocytes within the optic tract (**Figure 4.3A**). EAE sections did not show overt levels of microglia activation or astrogliosis until 26dpi. Microglial immunoreactivity remained high at 47dpi, however GFAP expression decreased. Normal sections showed a high density of coherent and aligned Thy1-YFP axons in the optic tract (**Figure 4.3B**). In EAE sections lower axon density and some axon

fragmentation was evident at 15dpi. At 26 dpi, just after peak clinical disease, severe axon fragmentation was observed, and few intact axons could be identified. This level of axon degradation remained present at 47dpi. Quantification of Iba1 immunoreactivity revealed significant increases compared to normal starting at 26 dpi, which remained at 47dpi (**Figure 4.3C**). GFAP immunoreactivity was significantly increased compared to normal at 15dpi and 26dpi, but decreased at 47dpi to a level not significantly different from normal (**Figure 4.3D**).

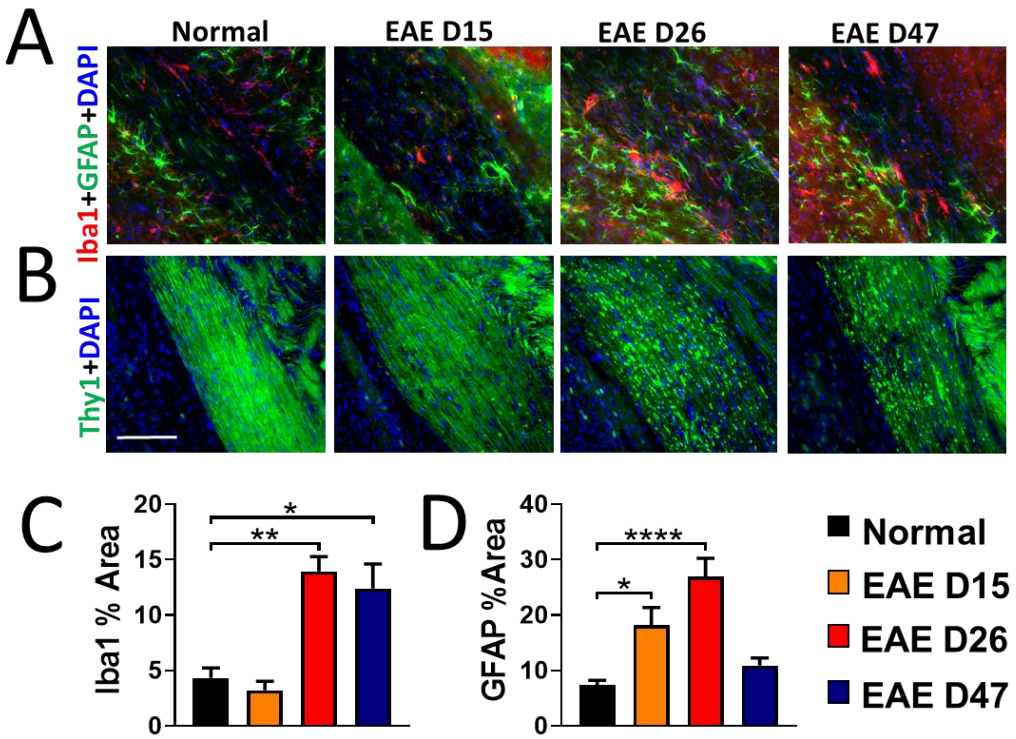

Figure 4.3: Optic tracts from EAE mice exhibit inflammation at peak disease, and progressive astrogliosis and axonal damage. A. Coronal optic tract sections were obtained from Thy1-YFP (green) normal and EAE mice at 15dpi, 26dpi, and 47dpi, stained for Iba1 (red), GFAP (green), and DAPI, and imaged at 20x magnification. Iba1 immunoreactivity is evident within the normal optic tract and surrounding areas however GFAP$^+$ astrocytes primarily border the optic tract. EAE sections show increases in Iba1 and GFAP immunoreactivity predominantly at 26dpi. **B.** Thy1-YFP axons are coherent and densely populate the optic tract in normal coronal sections. Fewer Thy1-YFP axons are observed at 15dpi, with some fragmentation and swelling evident. At 26dpi and 47dpi, significant axon fragmentation and swelling is observed and few intact axons remain. **C.** Iba1 immunoreactivity in EAE is increased significantly compared to normal at 26dpi and 47dpi, and GFAP (**D.**) at 15dpi and 26dpi. n=4 mice per group. *P<0.05, **P<0.01, **** P<0.0001, ordinary one-way ANOVA with Kruskal-Wallis multiple comparison test. Scale bar is 100µm.

Progressive demyelination is coupled with severe OL loss in the dLGN of EAE mice.

The dLGN not only serves as an important intermediary between the retina and the visual cortex in the afferent visual pathway, but also is significantly involved in processing and modulation of the visual signal(Kerschensteiner and Guido, 2017; Rompani et al., 2017). The human LGN consists of six cellular layers separated by thin sheets of myelinated fibers, and thus is susceptible to MS-induced demyelination (Corbett and Chen, 2018). Myelination in the normal mouse dLGN and demyelination due to 5wks of CPZ diet and the neurotoxin Ibotenic acid have previously been reported (Araujo et al., 2017; Coffey et al., 1988). However, EAE-induced effects on myelination within the mouse dLGN have not been previously assayed.

To assess longitudinal changes to myelination and OLs in the dLGN during EAE, coronal sections from normal and EAE mice containing the dLGN were immunostained for MBP, CC1, and Olig2 and co-stained with DAPI. Normal dLGN showed highly myelinated fiber tracts across the dLGN, interleaved between partially myelinated cellular layers (**Figure 4.4A**). Sections obtained from EAE mice at 15dpi, showed similar levels of myelination as in normal, however a loss of the organization of the myelinated fiber tracts. Sections from 26dpi and 47dpi EAE mice showed decreased overall levels of myelination, as well as fragmentation of myelinated fiber tracts. Quantification of myelin percent area revealed significant and progressive decreases in myelination at all EAE timepoints (**Figure 4.4C**). Olig2 immunostaining in normal dLGN sections revealed a significant presence of OL lineage cells which include OL precursors, premyelinating OLs, and mature myelinating OLs (**Figure 4.4B**). Very few $Olig2^{+}$ cells were observed in sections

from EAE mice at all timepoints. CC1 staining similarly revealed a significant presence of mature myelinating OLs in normal, and few in EAE at any timepoint. Quantification of Olig2$^+$ cells (**Figure 4.4D**) and CC1$^+$ cells (**Figure 4.4E**) showed almost complete ablation of Olig2$^+$ cells, and a 15-fold decrease in CC1$^+$ cells at all EAE timepoints.

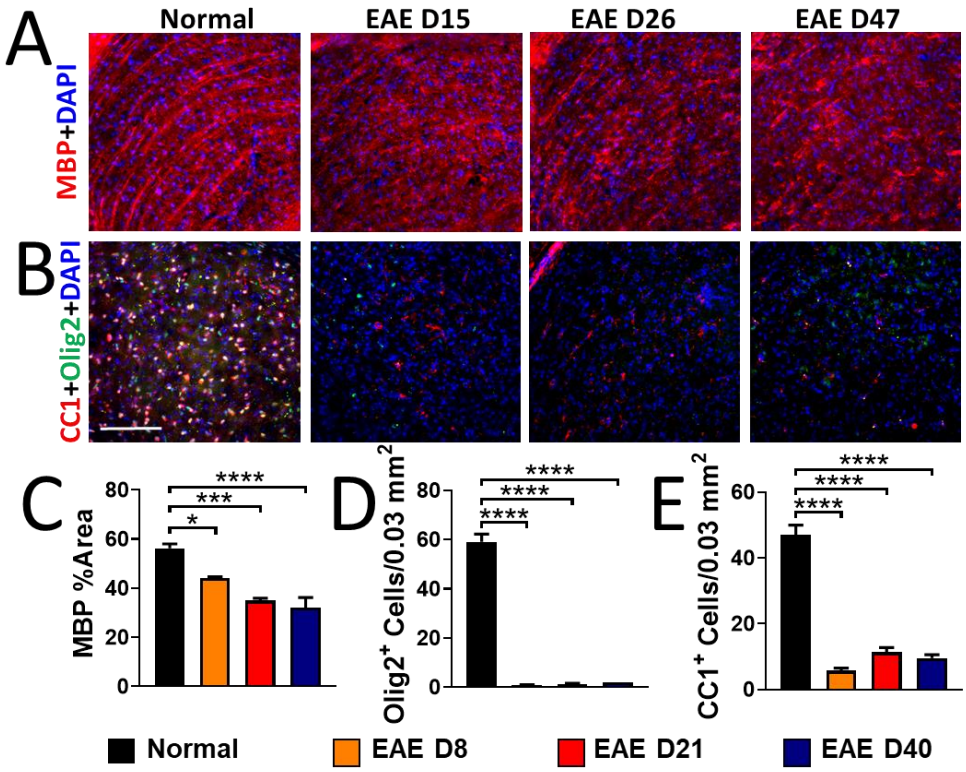

Figure 4.4: The dLGN exhibits progressive demyelination and extensive OL loss early in EAE and throughout disease progression. A. Coronal sections containing the dLGN were obtained from normal and EAE Thy1-YFP transgenic mice at 15dpi, 26dpi, and 47dpi. Sections were stained for MBP, co-stained for DAPI and imaged at 20x magnification. Decreased organization of dLGN myelinated fiber tracts, and decreased myelination is evident in EAE sections at 15dpi, 26dpi, and 47 dpi. **B.** Coronal dLGN sections were stained for Olig2 (green) and CC1(red), co-stained for DAPI, and imaged at 20x. Significant Olig2 and CC1 immunoreactivity is observed in normal sections with Olig2$^+$ and CC1$^+$ cells exhibiting nuclear and cytosolic staining respectively. **C.** Percent area of MBP staining was quantified in sections from normal and EAE groups. Significant and progressive decreases in MBP percent area is evident at all timepoints. **D.** Cell counts of Olig2$^+$ cells reveal almost complete ablation of OL lineage cells in the dLGN of EAE mice compared to high numbers in normal. **E.** Cell counts of CC1$^+$DAPI$^+$ cells reveal significant and greater than 15-fold decreases in the number of mature myelinating OLs at all timepoints. n=4 mice per group. *P<0.05, *** P<0.001, ****P<0.0001, ordinary one-way ANOVA with Kruskal-Wallis multiple comparison test. Scale bar is 100µm.

The dLGN exhibits progressive increases in astrogliosis in EAE, but no change to microglia, neuron numbers, or PV immunoreactivity.

Inflammatory demyelination incurred by CPZ diet has been shown to induce significant increases in microglial and astrocytic reactivity in the dLGN(Araujo et al., 2017). To probe EAE-induced longitudinal effects on the microglia and astrocyte populations within the dLGN, coronal LGN sections were obtained from normal mice and EAE mice euthanized at 15dpi, 26dpi, and 47dpi, immunostained for Iba1 and GFAP, and co-stained for DAPI. Normal sections showed minimal levels of Iba1 immunoreactivity, primarily located in the center of the dLGN, and GFAP immunoreactivity primarily located at the borders of the dLGN (**Figure 4.5A**). Sections from EAE mice showed non-significant changes to Iba1 immunoreactivity (**Figure 4.5A, C**) however progressive increases in GFAP immunoreactivity which were significant at 26dpi and 47dpi (**Figure 4.5A, D**).

The dLGN is home to a number of thalamocortical projection neurons which send afferents to layers 4-6 of V1, as well inhibitory interneurons which modulate information transfer from the retina to the visual cortex. Loss of synaptic input from RGCs has been shown to cause significant neuronal apoptosis in the LGN(You et al., 2012). The presence of significant EAE-induced damage in RGC axons of the optic tract suggested possible downstream neuronal loss in the dLGN. To quantify changes in dLGN neurons, normal and EAE coronal sections containing the dLGN were immunostained for NeuN and PV. In normal sections NeuN staining was evident in neuronal cell nuclei, while PV staining was primarily observed in dendritic fibers and some cell bodies (**Figure 4.5B**). Interestingly,

thin streaks absent of PV immunoreactivity were evident across the LGN and likely corresponded to the myelinated fiber tracts observed in figure 17A. EAE sections did not show differences in NeuN staining, or $NeuN^+$ cell numbers (**Figure 4.5B, E**). PV immunoreactivity was likewise not overtly changed in EAE compared to normal, however some loss of organization was observed in sections from all timepoints (**Figure 4.5B, F**).

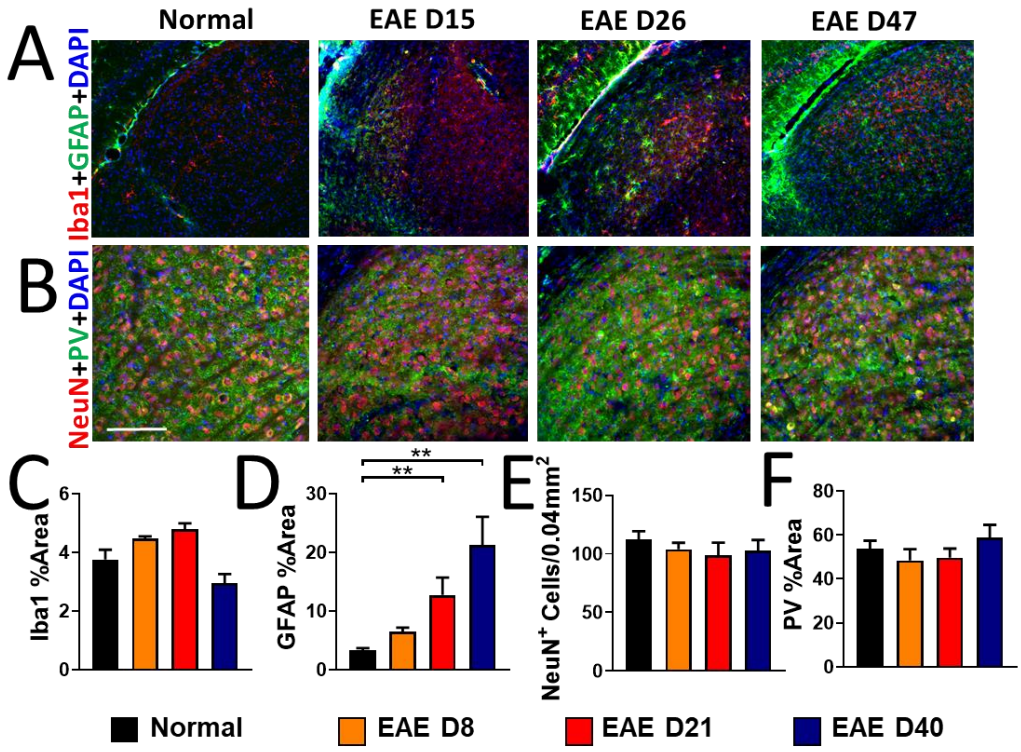

Figure 4.5: EAE-induced effects in the dLGN include astrogliosis, but not microglial activation or neuronal loss. A. Coronal sections containing the dLGN were obtained from normal and EAE mice at 15dpi, 26dpi, and 47dpi. Sections were stained for Iba1 and GFAP, co-stained for DAPI, and imaged at 20x magnification. The dLGN shows minimal Iba1 and GFAP immunoreactivity in normal sections, and minimal changes to $Iba1^+$ microglia in EAE sections, but progressive EAE-induced increases in GFAP immunoreactivity at 26pi and 47dpi. **B.** Coronal dLGN sections were immunostained for NeuN (red) and PV (green), co-stained for DAPI, and imaged at 20x. Normal sections show extensive numbers of NeuN nuclei, and PV^+ neuropil which are absent in some elongated tracts. EAE sections from all timepoints show similar numbers of NeuN nuclei, and similar overall PV^+ staining, but some disorganization of neuropil. **C.** Quantification of Iba1 percent area shows no significant difference in staining. **D.** GFAP percent area quantification shows progressive increases in GFAP staining which become significant compared to normal at 26dpi and 47dpi. **E-F.** No significant differences in $NeuN^+$ neurons, or PV percent area are observed between groups. n=4 mice per group. ** P<0.01, ordinary one-way ANOVA with Kruskal-Wallis multiple comparison test. Scale bar is 100µm.

The visual cortex exhibits significant and persistent demyelination in EAE, which is coupled with severe decreases to the OL population.

Thalamocortical neurons in the dLGN project to layer 4-6 of the visual cortex, where synaptic inputs are processed and transferred to layer 2/3, 5 and 6 pyramidal neurons. These neurons in conjunction with inhibitory circuits generated by cortical inhibitory neurons, and feedback from higher order visual areas, form the final visual image (Douglas and Martin, 2004; Gilbert and Wiesel, 1979; Gilbert and Wiesel, 1983; Glickfeld and Olsen, 2017; Wood et al., 2017). Although the cortex is accepted to be a gray matter region, a large number of cortical pyramidal neurons and PV^+ interneurons are myelinated (Micheva et al., 2016; Tomassy et al., 2014).

To evaluate the effects of EAE on myelination and OLs within V1, coronal sections containing V1, as identified by the presence of a large and dense granular cell region in layer 4A, were immunostained for MBP, CC1 and Olig2, then co-stained with DAPI. Normal sections were myelinated in V1, with the densest MBP staining present in ventral regions of the cortex (**Figure 4.6A**). A significant and almost 50% decrease in myelination was observed in EAE sections at all timepoints (**Figure 4.6A, C**). Layer 4 normal V1 was also highly populated by $Olig2^+$ OL lineage cells as well as $CC1^+$ mature myelinating OLs (**Figure 4.6B**). Both cell types were significantly decreased by at least 4- fold, and in the case of $CC1^+$ cells, 5-fold (**Figure 4.6B, D, E**).

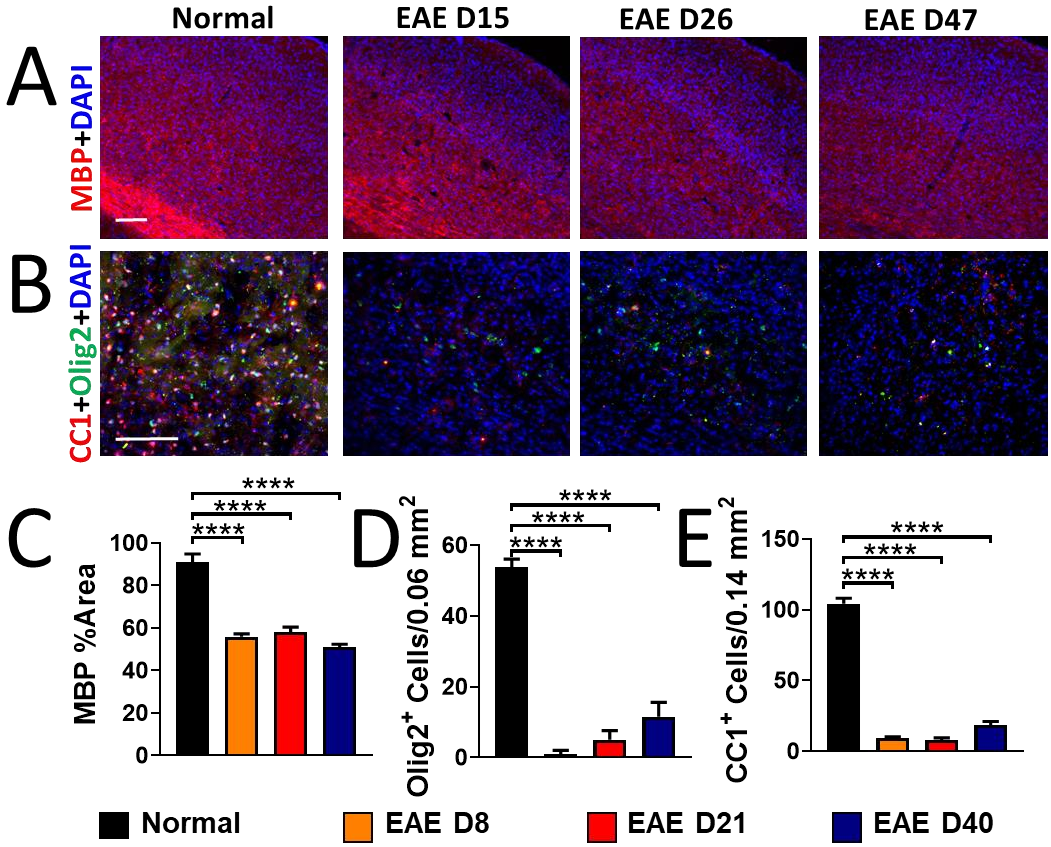

Figure 4.6: EAE visual cortex shows significant demyelination and OL loss compared to normal controls. A. Coronal sections containing V1 and obtained from normal, and EAE groups were stained for MBP and imaged at 10x magnification. Normal sections are myelinated, with densest regions of MBP immunoreactivity in more ventral regions of the visual cortex. The corpus callosum, ventral and adjacent to the visual cortex exhibits a higher density of MBP immunoreactivity than V1. EAE sections show depletion of MBP immunoreactivity compared to normal in visual cortex and adjacent corpus callosum at all timepoints. **B.** V1 coronal sections were immunostained for CC1 and Olig2, co-stained with DAPI, and imaged at 20x magnification in layers 4. Olig2$^+$ OL lineage cells, and CC1$^+$ mature myelinating OLs were ubiquitous in layer 4 of normal sections. EAE sections showed few Olig2$^+$ or CC1$^+$ cells. **C**. Significant myelin loss is observed at all EAE timepoints compared to normal controls. **D-E.** Quantification in layer 4 reveals significant, OL-lineage-cell and OL loss in V1 at all EAE timepoints compared to normal. *n*=4 mice per group. **** *P*<0.0001, ordinary one-way ANOVA with Kruskal-Wallis multiple comparison test. Scale bar is 100µm.

Astrogliosis, present at early and peak EAE disease, precedes high levels of microglial activation at peak disease in the cortex; these pathological changes are associated with progressive loss of PV^+ interneurons.

Cortical microglia have been shown to become ramified and hypertrophied in chronic stages of EAE (Mangiardi et al., 2011). Astrocytes in the cortex have been shown to express higher levels of GFAP, indicative of gliotic responses to injury, at peak, remitting, and late disease stages of the relapsing remitting EAE model and at peak disease in the MOG 35-55 peptide EAE model(Eilam et al., 2018; Jukkola et al., 2013). To evaluate cortical changes in microglial, and astrocytic reactivity in V1, coronal sections containing V1 were immunostained for Iba1 and GFAP respectively. Iba1 immunoreactivity was not changed compared to normal except at 26dpi (**Figure 4.7A, C**), however GFAP showed significant and progressive increase in immunoreactivity at 15dpi and 26dpi, but decreased to a level not significantly different from normal at 47dpi (**Figure 4.7A, D**).

Neuronal cell types in the visual cortex primarily include pyramidal neurons, granular cells, and inhibitory interneurons(Harris and Mrsic-Flogel, 2013). Granule cells in layer 4 are the primary recipients of geniculo-cortical information, while pyramidal neurons of layer 2-3, 5, and 6 are the primary excitatory neurons involved in visual processing and transference of cortical information to other brain regions(Douglas and Martin, 2004; Gilbert and Wiesel, 1979; Gilbert and Wiesel, 1983; Glickfeld and Olsen, 2017; Wood et al., 2017). In contrast, inhibitory neurons such as PV^+ cells are associated with modulation of visual processing(Wood et al., 2017). The loss of myelination from the

visual cortex had the potential to alter neuronal survival. Furthermore, V1 atrophy is a primary feature of MS pathology, indicating the possibility of V1 neuronal death(Balk et al., 2015; Gabilondo et al., 2014; Gabilondo et al., 2017).

In order to quantify EAE-induced neuronal pathology in V1, coronal sections from normal and EAE mice were immunostained for NeuN and PV, co-stained with DAPI, and imaged in layer 4. Normal sections showed robust numbers of $NeuN^+$ cells and PV^+ cells interspersed throughout with a high density of PV^+ fibers evident in layer 4B (**Figure 4.7B**). EAE sections showed similar amounts of $NeuN^+$ cells but decreased numbers of PV^+ cells compared to normal at all timepoints. Quantification revealed no differences in the number of $NeuN^+$ cells across groups, although a progressive decline of PV^+ cells which was significantly lower than normal at all EAE timepoints, was evident (**Figure 4.7 E, F)**.

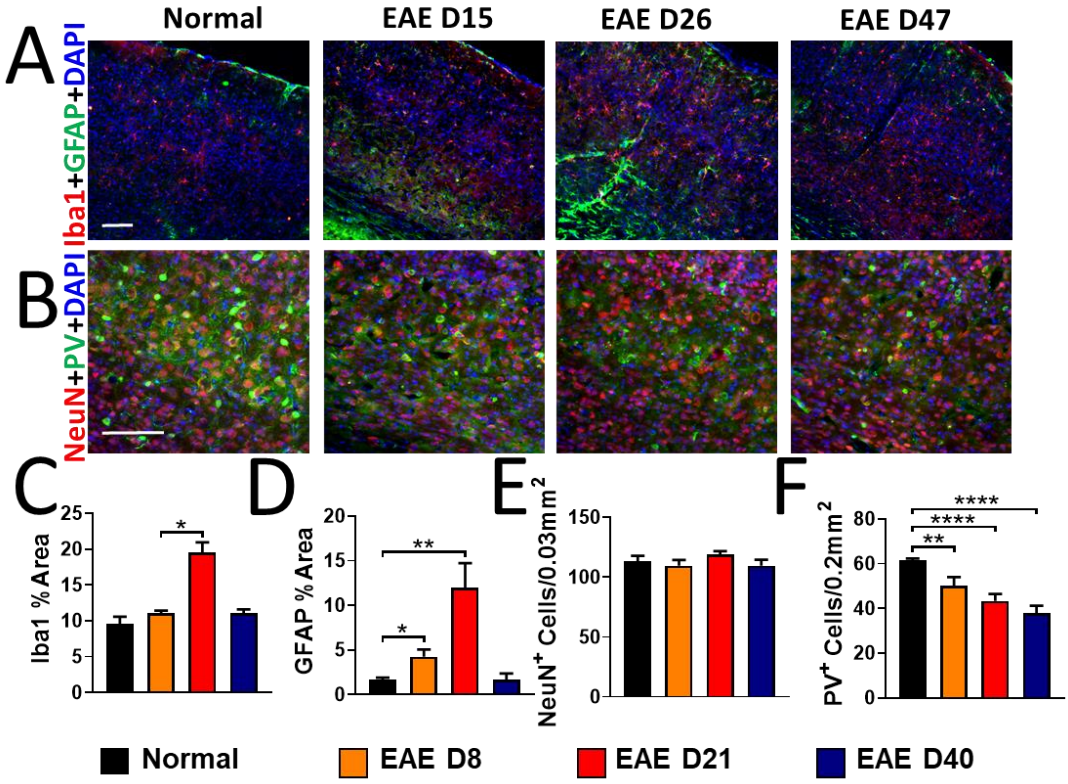

Figure 4.7: EAE visual cortex exhibits inflammation, astrogliosis, and progressive PV$^+$ interneuron loss. A. Coronal sections obtained from normal and EAE groups, and containing V1 were stained for Iba1 and GFAP, and imaged at 10x magnification. Iba1 immunoreactivity is relatively similar across groups with the exception of an increase in the EAE 26dpi group. GFAP immunoreactivity is increased in EAE sections at 15dpi and 26dpi, but not at 47dpi as compared to normal. **B.** Coronal sections containing V1 were obtained from normal and EAE mice, immunostained for NeuN and PV, and imaged in layer 4 of V1 at 20x magnification. NeuN$^+$ cell density does not overtly change between treatment groups, however the PV$^+$ interneuron density is decreased in all EAE sections compared to normal. **C-D.** Quantification of Iba1 and GFAP percent area show significant increases in Iba1 immunoreactivity at 26dpi, and in GFAP immunoreactivity at 15 and 26dpi compared to normal. **E-F.** The number of NeuN$^+$ cells is not significantly changed between groups, however a progressive decrease in PV$^+$ neurons is observed in EAE compared to normal, and is significant at all EAE timepoints. n=4 mice per group. *P<0.05, **P<0.001, **** P<0.0001, ordinary one-way ANOVA with Kruskal-Wallis multiple comparison test. Scale bar is 100µm.

In vivo studies of visual pathway pathology and function are crucial for understanding longitudinal disease progression in both MS and EAE. Especially useful in the assessment of the afferent visual pathway are translationally relevant methods such as

MRI, ERGs, VEPs, and OCT which can be assayed in animal models and transferred to the clinic. Although MRI is the gold-standard for evaluation of MS pathology, it is expensive and can be difficult to access for a number of MS and EAE researchers. As a result, evoked potentials and OCT which are similarly translationally relevant have been used with increasing frequency in evaluating MS pathology, and pathology in its animal models (Pihl-Jensen et al., 2017). However, a longitudinal correlation between histologically examined posterior visual pathway pathology, and *in vivo* OCT, ERGs, and VEPs has been yet to be provided in EAE.

EAE mice show decreased RNFL thickness only at the chronic EAE stage, but changes to posterior retinal layers throughout disease progression.

In order to evaluate EAE-induced pathological deficits in the retina, OCT was used to image retinas from awake and anesthetized, normal and EAE cohorts of mice at 13dpi, 20dpi, and 38dpi. These timepoints corresponded to onset, peak, and chronic disease stages respectively. Retinas from both eyes were imaged just temporal to the optic nerve (**Figure 4.8A-i**) and layer thicknesses measured across the retina, in the RNFL, GCL+IPL complex, INL+OPL, ONL+PR, and RPE (**Figure 4.8A-ii**). Layer thicknesses were not significantly different between groups in whole retina, INL+OPL, or ONL+PR measurements (**Figure 4.8B**). Significant decreases in thickness compared to normal were observed in the RNFL at 38dpi, GCL+IPL complex at 20dpi, and RPE at 13dpi, possibly due to cellular damage

in these areas. The RPE also exhibited a significant increase in layer thickness at 38dpi compared to normal possibly due to pathological swelling.

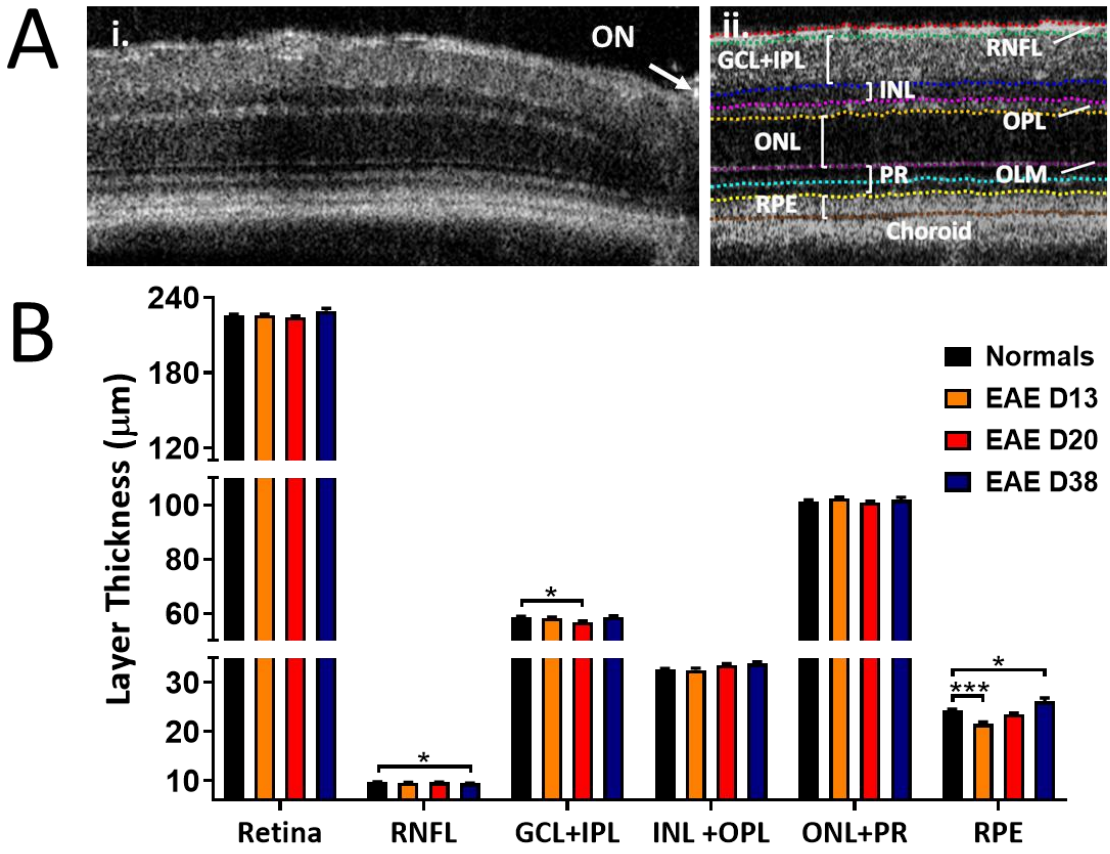

Figure 4.8: OCT imaging reveals EAE-induced pathological decreases in anterior retinal layer thicknesses and changes to RPE layer thickness throughout disease progression. A. OCT dataplots were obtained from the retinas of live and anesthetized mice temporal to the optic nerve (i). Automatic segmentation by Leica/Bioptigen imaging software quantified retinal layer thicknesses in the RNFL, GCL+IPL complex, INL, OPL, ONL, PR, and RPE regions (ii). For ease of analysis, INL+OPL, and ONL+PR layers were combined. **B.** No differences in overall retinal thickness are observed between treatment groups. RNFL shows significant decreases compared to normal only at 38dpi. GCL+IPL complex shows significant decreases in EAE mice compared to normal at 20dpi. The RPE layer shows significant decreases in layer thickness compared to normal during onset at 13dpi, and increases in the chronic stage at 38dpi. n=4 mice per group. *P<0.05, *** P<0.001, ordinary one-way ANOVA with Kruskal-Wallis multiple comparison test.

Retinal function is significantly impaired in EAE mice

To ascertain EAE-induced functional deficits in the retina, ERGs in response to three-candela-flash light stimulus were obtained from live anesthetized normal and EAE mice at 8dpi, 21dpi, and 40dpi. These timepoints, similar to those in OCT, corresponded to EAE onset, peak EAE, and chronic EAE disease stages respectively. Normal mice exhibited robust ERGs with average latencies of response to light stimulus of 20ms and 40ms and average amplitudes of 200µV and 500µV for A-wave and B-wave respectively (**Figure 4.9A-C**). EAE mice exhibited increased latency of response after light stimulus compared to normal controls in the A-wave and B-wave at 8dpi but not at 21dpi or 40dpi (**Figure 4.9A, B**). A-wave and B-wave amplitude deficits were also evident in EAE mice compared to normal at 8dpi, and B-wave deficits persisted through 26dpi and 47dpi (**Figure 4.9A, C**).

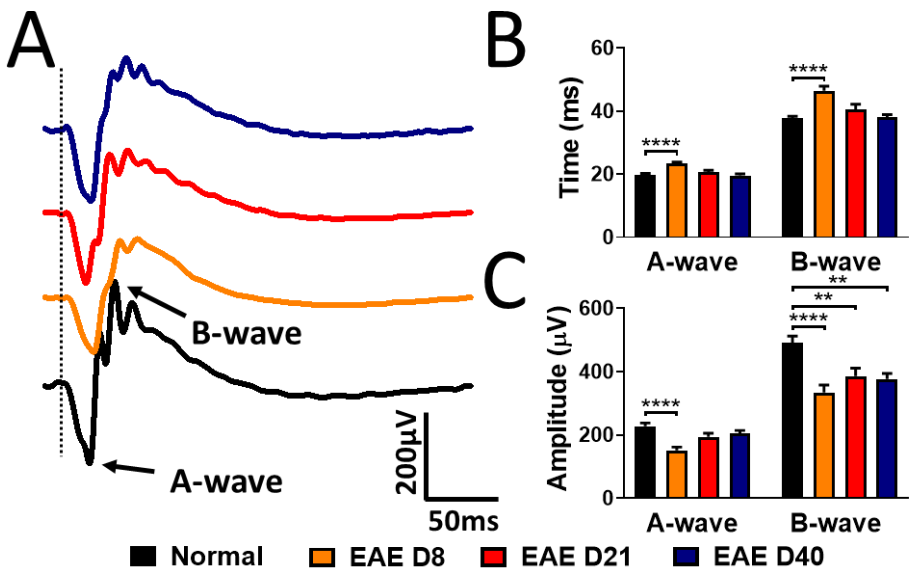

Figure 4.9: ERG latencies after flash stimulus are impaired early in EAE, whereas amplitude deficits are evident throughout disease progression. A. ERGs in response to three-candela-flash light stimulus were obtained from live and anesthetized normal and EAE mice. Representative traces depict averaged traces for normal, 8dpi EAE, 21dpi EAE, and 40dpi EAE groups. A-wave and B-wave peaks are identified. **B.** Normal ERG A-wave and B-wave peaks occur at approximately 20ms and 40ms after stimulus respectively. EAE mice at 8dpi exhibit delays in A-wave and B-wave peak time after stimulus compared to normal. Peak latencies of EAE mice at 21dpi and 40dpi are not significantly different from normal. **C.** Normal ERG A-wave and B-wave peak amplitudes average approximately 200 and 500µV respectively. A-wave amplitudes are significantly decreased compared to normal in EAE mice at 8dpi however not at 21dpi or 40dpi. B-wave amplitudes are significantly decreased at all EAE timepoints compared to normal. *n*=4 mice per group. ***P*<0.01, **** *P*<0.0001, ordinary one-way ANOVA with Kruskal-Wallis multiple comparison test.

Afferent visual function is significantly impaired in EAE mice

To characterize EAE-induced functional deficits across the afferent visual pathway, VEPs in response to three-candela-flash light stimulus were obtained from live anesthetized normal and EAE mice at 8dpi, 21dpi, and 40dpi. Normal controls exhibited robust VEPs consisting of an initial positive P1 deflection, followed by a negative N2, and gradual return to baseline (**Figure 4.10A**). Response times of P1 and N2 peaks averaged 20ms and 40ms, while amplitudes averaged 40µV, and 60µV respectively (**Figure 4.10A-**

C). EAE mice exhibited significant increases in P1 and N2 latencies at 8dpi and 21dpi, but no difference compared to normal at 40dpi (**Figure 4.10B**). P1 amplitudes were not significantly different between normal and EAE groups, however N2 amplitudes were decreased at all EAE timepoints compared to normal (**Figure 4.10C**).

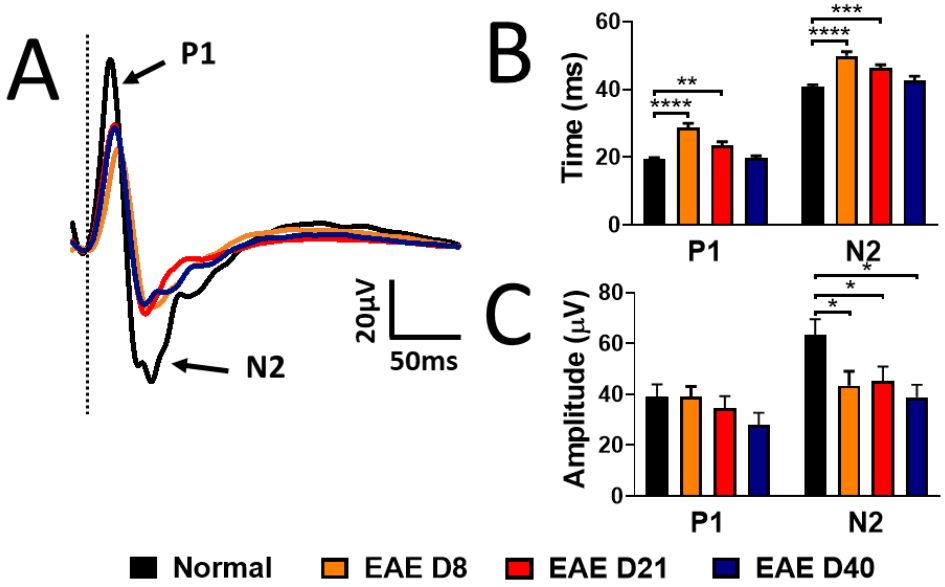

Figure 4.10: VEP latencies after flash stimulus are impaired at onset and peak EAE, whereas N2 amplitude deficits are present throughout disease progression. A. VEPs in response to three-candela-flash light stimulus were obtained from live and anesthetized normal and EAE mice. Representative traces depict averaged traces for normal, 8dpi EAE, 21dpi EAE, and 40dpi EAE groups. P1 and N2 peaks are identified. **B.** Normal VEP P1 and N2 peaks occur at approximately 20ms and 40ms after stimulus respectively. EAE mice at 8dpi and 21dpi exhibit delays in P1 and N2 peak time after stimulus compared to normal. Peak latencies of EAE mice at 40dpi are not significantly different from normal. **C.** Normal VEP P1 and N2 peak amplitudes average approximately 40 and 60µV respectively. P1 amplitudes are not significantly different between normal and EAE groups, however N2 amplitudes are decreased compared to normal at all EAE timepoints. n=4 mice per group. *P<0.05, **P<0.01, ***P<0.001, **** P<0.0001, ordinary one-way ANOVA with Kruskal-Wallis multiple comparison test.

4.4 Discussion

In the preceding study, EAE-induced visual pathway pathology was assessed in the posterior visual system over the course of the disease. To this end, histological assessments, *in vivo* assessments of retinal morphology, and *in vivo* functional assessments of the retina and visual pathway were employed. Histological results revealed that significant demyelination occurred throughout the visual system early in EAE, astrogliosis primarily at early timepoints, microglial activation primarily at peak disease, and neurodegeneration at peak to chronic disease stages. Retinal pathology was restricted to the RNFL and GCL+IPL layers at chronic and peak disease stages respectively, and to the RPE at both peak and chronic disease. The retina exhibited functional deficits associated with photoreceptor activity at early timepoints, and associated with retina interneurons and RGCs at all timepoints. Deficits in visual response times occurred primarily at early and peak disease, whereas decreased amplitudes were measured at all disease stages.

Retinal pathology

MS patients with or without ON often show pathological thinning or thickening of various retinal layers throughout disease progression. Anterior regions of the retina such as the RNFL and GCL+IPL primarily exhibit progressive thinning(Al-Louzi et al., 2016; Gabilondo et al., 2015; Saidha et al., 2011a). In medial areas such as the INL and OPL there is often no MS-induced effect observed although one study indicated a correlation between macular thinning, high expanded disability status scale scores, and thinning of the

middle retina (Saidha et al., 2011b). Outer neural retina areas such as the ONL and PR can have varied responses after optic neuritis depending on disease stage. Acute swelling of these layers often occurs within 1 month after ON onset, followed by either no discernable difference in thickness from baseline, or a progressive decline(Al-Louzi et al., 2016; Gabilondo et al., 2015; Seigo et al., 2012).

In the preceding work, we show significant EAE-induced decreases in the RNFL at chronic disease stages, similar to observations in MS patients, who show higher levels of RNFL atrophy with disease progression (Behbehani et al., 2017; Garcia-Martin et al., 2017). In addition, GCL+IPL thinning was observed at peak disease similar to reports in MS where it is often observed soon after optic neuritis(Al-Louzi et al., 2016; Saidha et al., 2011b). Furthermore, two recently published studies in EAE have also reported decreased GCIP (Manogaran et al., 2018; Nishioka et al., 2019).

Interestingly, GCL+IPL thinning appeared to be resolved at 40dpi, and was not significantly different from normal. Previous OCT assessments of retina in EAE also show no difference in GCIP thickness between normal and 40dpi (**Figure 3.9C**). It is unclear why the GCIP thickness is so changed in the chronic stage however macular edema has been reported in MS patients (Gelfand et al., 2012). Swelling of the GCIP after neuronal damage may have contributed to observed increases in layer thickness.

The RPE has been reported to thicken in MS patients with optic neuritis (Droby et al., 2016). In the current work, we report thinning of the RPE after 13dpi, a return to baseline at 20dpi, and subsequent thickening at 38dpi. Although RPE pathology has not

been previously studied in animal models for MS, RPE thinning is commonly associated with loss of pigment epithelial cells often due to aging, and thickening often due to chronic inflammatory retinal damage (Bonilha, 2008; Gao and Hollyfield, 1992; Penfold et al., 2001). It is possible that similar events occurred in EAE with early pigment epithelial cell damage resulting in the observed thinning and the presence of a chronic inflammatory response causing RPE hypertrophy. However, further investigations into RPE cellular pathology during EAE are necessary.

ERGs

Retinal pathology identified by OCT was associated with functional deficits in ERGs. A-wave amplitudes and latencies, results of photoreceptor activity, were both impaired at 8dpi. ERGs obtained from MS patients show conflicting results with respect to photoreceptor response time and amplitude of response, with some studies reporting no differences compared to normal controls (Hamurcu et al., 2017; Papakostopoulos et al., 1989), and others showing an impaired response(Forooghian et al., 2006; Hanson et al., 2018). The contradictory responses reported in MS may be due to differential timing of assessment. We report impairments in the A-wave only in early EAE, and prior to onset, but not at peak disease or chronic disease. The transient nature of the response in EAE indicates that some MS studies may have been completed outside of the window of observable photoreceptor dysfunction. Because the A-wave is associated with photoreceptor activity, and the photoreceptors are the first step in visual processing, it is important to characterize early deficits in these cell types during MS and EAE.

In contrast, deficits in B-wave amplitudes and latencies are consistently reported in MS patients(Forooghian et al., 2006; Hamurcu et al., 2017; Hanson et al., 2018; Papakostopoulos et al., 1989). These are associated with cells post-synaptic to the photoreceptors including bipolar cells, Müller glia, and RGCs (Perlman, 1995; Smith et al., 2014). The deficits observed in the A-wave early in EAE, and the B-wave at all EAE timepoints indicate significant pathology within the neural retina.

Visual pathway pathology

The visual pathway exhibits significant deficits in MS which include demyelinated lesions throughout white matter tracts(Graham and Klistorner, 2017), and gray matter atrophy(Balk et al., 2015; Gabilondo et al., 2014; Gabilondo et al., 2017; Papadopoulou et al., 2019; Shen et al., 2019). In EAE, white and gray matter pathology of the posterior visual pathway was observed throughout disease progression.

White matter pathology

White matter pathology included early demyelination and astrogliosis at all EAE timepoints, as well as microglial activation and extensive axonal damage at peak and chronic disease timepoints. It is unclear why early demyelination was not associated with overt microglial activation in EAE, as acute demyelinating lesions in MS are generally characterized by the presence of macrophages and microglia throughout the lesion area (Kuhlmann et al., 2017). Among other roles, these pro-inflammatory cells engulf damaged myelin and OLs as well as normal appearing white matter from MS patients (Hendrickx et al., 2014) and as such play a major role in demyelination. However, an insight to how

demyelination could proceed in optic tract, in the absence of these cells could be provided by the presence of hypertrophied and activated astrocytes, which also play a major role in myelin removal under disease conditions(Morizawa et al., 2017).

Demyelination was also associated with early pathological increases in VEP latencies in EAE, which were attenuated at peak and chronic disease stages. These results support deficits observed in optic neuritis in which there is acute vision loss followed by partial recovery(Toosy et al., 2014). One potential explanation for this is that axons which are partially demyelinated at early disease stages can still conduct albeit more slowly than fully myelinated axons. Demyelination of the axon results in a conduction block(Smith and McDonald, 1999) and as the severity of demyelination and axon damage progresses these axons would stop contributing to the VEP and thus no longer delay VEP peak times. Robust axons which were minimally myelinated, and fire similarly to normally myelinated axons could become primary contributors to the EAE VEP, and thus return the latency recorded to normal levels.

However, this is unlikely for a few reasons. First, such a scenario would require progressive decreases in VEP amplitudes. Because the VEP amplitude is a compound action potential recorded in V1, it is a measure of the number of V1 neurons which can be recruited to fire in response to the flash stimulus at the retina(Creel, 1995a). If the former argument were correct, the amplitude of the VEP would remain close to normal levels at early timepoints when latency deficits are most pronounced. In this case a large number of V1 neurons would still contribute to the V1 amplitude even if they or their synaptic

precursors were partially demyelinated. However, significant deficits in VEP amplitudes were observed in early disease stages, and these deficits did not become progressively worse with disease progression.

Second, the presented histological results do not support this hypothesis. Significant demyelination occurred early, and did not become progressively worse in the optic tract, and visual cortex. The dLGN did show progressive demyelination but even so, there was an almost 30% drop in myelination at the early timepoint compared to normal.

Finally, partially demyelinated axons still contributing to the VEP would be expected to cause a broadening of VEP peaks compared to normal at early EAE timepoints, as has been reported in other evoked potentials(Deguchi et al., 1992). However, measures of the full width half maximum of VEP peaks revealed no significant differences in the broadness of recorded peaks between groups (**Appendix Figure A.1**), indicating that the presented hypothesis is incorrect.

Another potential explanation for spontaneous recovery of visual function could be a reorganization of sodium channels after prolonged demyelination. Myelin internodes generally exhibit low densities of sodium channels (>25 per μm^2 compared to ~1000 per μm^2 at nodes of Ranvier)(G. Waxman, 2005). However, 14 days after demyelination, sodium channels are distributed in relatively high densities in internodal regions (England et al., 1990). Such changes to sodium channel expression have been reported in optic nerve and spinal cord axons during EAE(Craner et al., 2003; Craner et al., 2004) and support the observation that demyelinated axons exhibit an abrogated but not abolished ability to

conduct potentials(Bostock and Sears, 1978). Further investigations of sodium channel distribution in the optic tract are necessary to elucidate this potential mechanism.

Axonal damage and loss are well-known features of MS pathophysiology, and primary indicators of disability outcomes. Damaged axons are present throughout active MS lesions and at the borders of inactive lesions (Ferguson et al., 1997; McDonald et al., 1999). In the current work, we show the presence of some damaged axons within the optic tract as early as 15dpi. The majority of axons at this timepoint were intact, but a few swollen endbulbs, indicative of transection, were present. At 26dpi and 47 dpi, the number of damaged axons increased greatly, and axons appeared fragmented. Thus, demyelination at 15dpi appears to precede overt axonal damage at 26dpi. This is similar to reports in the optic nerve which show demyelination at 11dpi and extensive axonal damage at 19dpi(Fairless et al., 2012). High numbers of activated microglia and macrophages were associated with higher levels of axon fragmentation at 26dpi, indicating a possible role for pro-inflammatory microglia in precipitating axonal loss. This is similarly observed in MS lesions in which there is a correlation between the number of macrophages and the extent of axonal damage(Ferguson et al., 1997).

Gray matter pathology

Extensive microglia and macrophage presence has been associated with degradation of synaptic proteins in the cortex(Rasmussen et al., 2007), production of reactive oxygen and nitrogen species precipitating axon degeneration (Nikic et al., 2011), as well as irreversible neuronal damage in a number of neurodegenerative diseases(Tang and Le, 2016). In the pathological brain, astrocytes express pro-inflammatory cytokines implicated in demyelination, exhibit decreased levels of potassium buffering, and provide insufficient fluid transfer, events which have been implicated in neurodegeneration (Lapato and Tiwari-Woodruff, 2018; Olabarria and Goldman, 2017). In the dLGN and V1, increases in microglial presence and astrogliosis were observed throughout EAE and may play a role in the observed disruption of PV^+ dendrites in the dLGN, and PV^+ neuron loss in V1. In fact, inflammatory demyelination has been shown to negatively impact inhibitory synapses in the dLGN, and PV^+ interneurons in the cortex(Araujo et al., 2017; Clements et al., 2008; Falco et al., 2014; Lapato et al., 2017; Potter et al., 2016). Furthermore, PV^+ neurons are myelinated and may be particularly susceptible to inflammatory demyelinating events(Micheva et al., 2016).

In the visual cortex, PV^+ neurons regulate network synchrony and their suppression results in decreased responsiveness to natural visual stimuli(Agetsuma et al., 2018; Zhu et al., 2015). VEPs obtained from EAE mice revealed significant deficits in amplitude of the visual response, suggesting a similar decrease in responsiveness. Thus, the observed

deficits in VEP amplitudes may be directly related to PV pathology, however further investigation is needed.

The pathophysiology of EAE in the posterior visual pathway is characterized by extensive demyelination early in disease followed by irreversible neurodegeneration at peak and late disease timepoints. These events are associated with microglial activation and astrogliosis, which in EAE and MS, can exacerbate neurodegenerative events. Similar results have been extensively reported on in the anterior portions of the visual system. Thus, therapeutic intervention to attenuate visual pathway pathology may require early treatment with remyelinating and immunomodulatory agents to attenuate inflammatory responses and prevent irreversible axon and neuronal damage. In the event, however that this is not possible therapeutic outcomes may be bleak.

Chapter 5: CPZ diet results in significant demyelination of the visual system but few functional deficits

5.1 Introduction

The CPZ demyelination model is a frequently used animal model for MS which relies on the toxic copper chelator CPZ, to induce regional demyelination within the brain. Unlike EAE, it does not rely on peripheral immune lymphocytes crossing the BBB to produce inflammatory factors that lead to demyelination and neurodegeneration in the CNS. Rather, the CPZ diet results in a copper deficiency associated with OL apoptosis and subsequent myelin loss. It is currently unclear the exact mechanism of action associated with CPZ-induced demyelination. However, the induced copper deficit is associated with dysfunction of mitochondrial enzymes such as cytochrome oxidase and monoamine oxidase, which rely on copper for proper function and oxidative phosphorylation (citation 39,40,43 from matsushima paper). For high-energy demand CNS cell types like OLs which rely significantly on mitochondrial activity, such deficits are particularly devastating and may lead to the observed OL apoptosis in this model. However, it is unknown why primarily OLs, and not similarly high-energy-demand CNS cell types like neurons, are affected (Matsushima and Morell 2001).

Although the CPZ model is particularly useful for understanding the role of demyelination in CNS pathology, very few studies have assessed CPZ-induced visual pathway pathology. Such a study is of particular interest due to the utility of the CPZ model for identifying remyelinating therapeutic agents (Alme et al., 2015; Ghaiad et al., 2017;

Moore et al., 2014b). Because successful pre-clinical agents are increasing evaluated in clinical trials using visual outcome measures, further evaluation of CPZ diet effects on the visual system is necessary.

In the following work, we present an assessment of CPZ-induced progressive visual pathway pathology in the mouse through *in vivo* and immunohistochemical assessments of the retina, optic tract, dLGN, and visual cortex. We evaluate functional changes, changes to myelination, astrogliosis, microglial activation, and axonal health at regular timepoints throughout disease progression until 12wks of CPZ diet. We report extensive and progressive demyelination across visual system white matter tracts, which does not result in overt axonal damage, or functional deficits.

5.2 Methods

Twenty-eight 8-12-week-old Thy1-YFP and PLP-EGFP male mice on a C57Bl/6 background received rodent chow infused with 0.2% CPZ (Envigo, Huntingdon UK) (**Figure 5.1A**). Mice were split into two separate experiments. One cohort of eight mice underwent longitudinal ERG and VEP assessments (Expt 1) at 6, 9, and 12weeks (**Figure 5.1B-i**). Another cohort of twenty mice were evaluated with OCT (Expt 2) (**Figure 5.1B-ii**). Groups of five mice in Expt 2 were perfused after 3wks, 6wks, 9wks, and 12wks of CPZ diet for IHC. Ten PLP-eGFP and four Thy1-YFP mice served as controls and were not euthanized for IHC until experiment end.

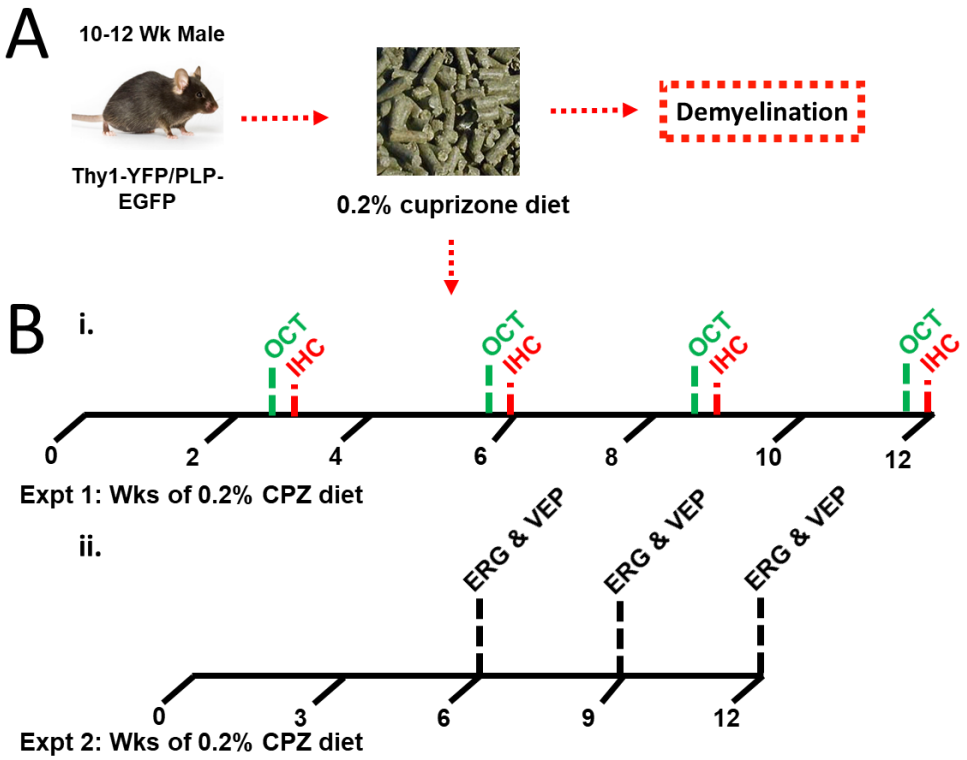

Figure 5.1: Experimental design for longitudinal assessment of visual pathway pathology in CPZ. A. Twenty-eight 10 to 12-week-old Thy-YFP and PLP-EGFP male mice on a C57Bl/6 background were placed on 0.2% CPZ diet, provided in normal rodent chow (Envigo, Huntingdon UK), resulting in selective demyelination within the CNS. **B.** Mice were split into two individual experiments: 20 mice for experiment 1, and 8 mice for experiment 2. Retina function of experiment 1 mice was evaluated after 3, 6, 9, and 12wks of CPZ diet (i). Five mice from experiment 1 were perfused for IHC at each timepoint. The second cohort of 8 mice underwent ERGs and VEPs after 6, 9, and 12wks of CPZ diet (ii). Ten PLP-eGFP and four Thy1-YFP mice served as controls and were not euthanized for IHC until experiment end.

5.3 Results

The CPZ diet has been reported to induce selective and reproducible demyelination in various CNS regions including the corpus callosum(Atkinson et al., 2019; Baxi et al., 2017; Lapato et al., 2017; Moore et al., 2014b; Steelman et al., 2012; Yamate-Morgan et al., 2019), hippocampus(Baxi et al., 2017; Koutsoudaki et al., 2009; Lapato et al., 2017; Norkute et al., 2009), cortex (Baxi et al., 2017; Gudi et al., 2009; Silvestroff et al., 2012), and cerebellum(Groebe et al., 2009; Oakden et al., 2017; Skripuletz et al., 2010; Steelman et al., 2012). Only one study has previously investigated CPZ demyelination within the visual pathway, however the time course of CPZ demyelination was not assessed(Araujo et al., 2017). The following work reports on longitudinal changes in myelination, microglia and astrocyte populations, axonal health and functional changes over the course of 12wks of 0.2% CPZ diet.

CPZ diet induces demyelination and mature OL loss after 3, 6, 9 and 12wks in the optic tract.

To investigate CPZ-induced changes to myelination and OLs in the optic tract coronal sections were obtained from PLP-EGFP mice either on normal diet, or on CPZ diet. CPZ mice were perfused after 3, 6, 9, or 12wks of CPZ diet, immunostained for MBP and CC1, then co-stained for DAPI. Sections from normal mice exhibited robust levels of myelination in the optic tract and adjacent hypothalamic regions, but not in the amygdala (**Figure 5.2A**). CPZ diet resulted in significant myelin loss evident at 3, 6, and 12wks of diet, however optic tracts from 9wk CPZ mice showed increased levels of myelination, and

were not significantly different from normal (**Figure 5.2A, C**). Normal sections obtained from PLP-EGFP mice and stained for CC1 showed robust numbers of PLP^+ premyelinating and mature OLs, and $CC1^+$ mature OLs (**Figure 5.2B**). CPZ diet had no significant effect on PLP^+ cell numbers, but resulted in decreased numbers of $CC1^+$ mature myelinating OLs at 6, 9 and 12wks (**Figure 5.2B, D, E**).

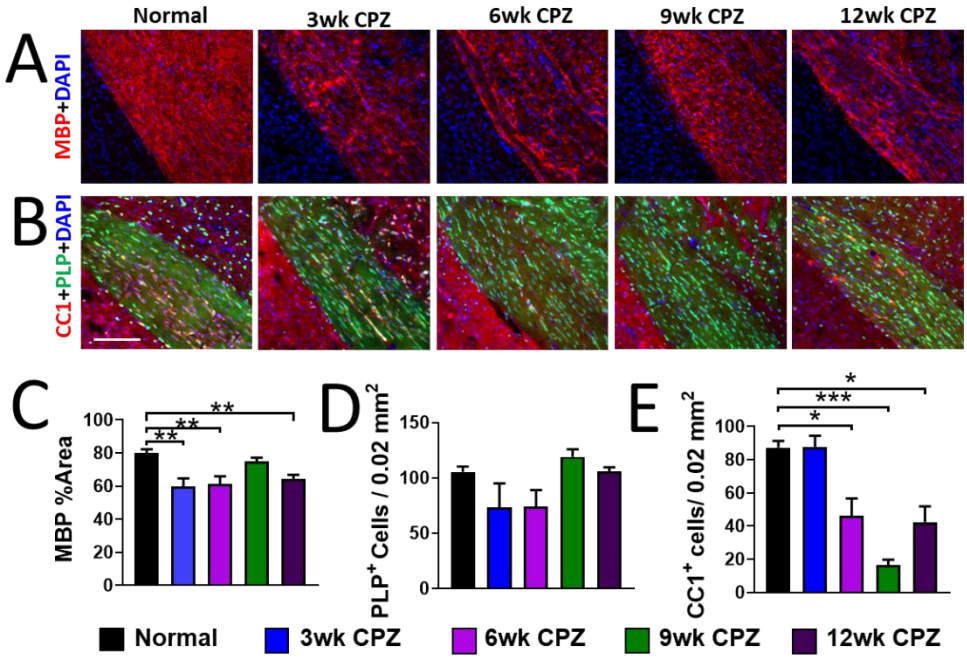

Figure 5.2: Toxic 0.2% CPZ diet induces significant demyelination after 3, 6, and 12 weeks, and mature myelinating OL loss after 6, 9 and 12wks in the optic tract. A. PLP-EGFP (green) mice were perfused after 3 (blue), 6 (purple), 9 (green), and 12wks (dark purple) of 0.2% toxic CPZ diet for IHC. Sections containing the optic tract were obtained, immunostained for MBP, co-stained with DAPI, and imaged at 20x in the dorsal region. Normal sections show robust myelination in the optic tract and adjacent hypothalamic region. Sections obtained from 3, 6, and 12 wk CPZ mice show patchy MBP staining and decreased overall MBP immunoreactivity. The 9wk CPZ section shows increased MBP staining which is not as robust as normal. **B.** Sections containing the optic tract and similarly obtained from normal, 3, 6, 9, and 12wk CPZ PLP-EGFP mice were immunostained for CC1 and co-stained with DAPI. Normal sections show high numbers of PLP^+ cells and few $CC1^+$ in more dorsal optic tract areas. In more ventral regions however, the density of PLP^+ cells remains similar but that of $CC1^+$ cells is increased. Sections from mice at all CPZ timepoints show high numbers of PLP^+ cells, however $CC1^+$ cells are depleted at 6wks, 9wks, and 12wks. **C.** Quantification of MBP percent area reveals significant decreases in MBP coverage at 3, 6, and 12wks compared to normal. **D-E.** Quantification of PLP^+ cells, and $CC1^+$ cells reveals no change in the former, but significant decreases in the latter at 6, 9 and 12wks compared to normal controls. n=5 mice per group. *P<0.05, **P<0.001, *** P<0.001, ordinary one-way ANOVA with Kruskal-Wallis multiple comparison test. Scale bar is 100µm.

Inflammation and astrogliosis, but not axon damage, are prevalent in the optic tract of CPZ mice.

The CPZ model does not exhibit a peripherally-induced immune response, nor overt blood-brain barrier breakdown (Bakker and Ludwin, 1987; Kondo et al., 1987). However, apoptotic OL and myelin debris results in early microglial and astrocytic recruitment, and subsequent phagocytosis of debris(Blakemore, 1972). Furthermore, significant astrocytic gliosis may precede microglial infiltration to demyelinated lesion sites(Matsushima and Morell, 2001).

To assay CPZ induced microglial activation and astrogliosis in the optic tract, coronal sections containing optic tract were obtained from normal, 3, 6, 9, and 12wk CPZ PLP-EGFP mice. Sections were immunostained for Iba1 and GFAP then co-stained with DAPI. Normal sections exhibited low levels of microglial immune reactivity throughout the optic tract, indicative of resident non-reactive cells. GFAP immunoreactivity was similarly low and primarily present in the borders of the optic tract (**Figure 5.3A**). Sections from CPZ mice at 3, 6, and 9wks showed a significantly higher presence of Iba1 compared to normal, with microglia exhibiting activated and hypertrophied morphology, (**Figure 5.3A, B**). Overall microglial presence was decreased in 12wk tissues, however reactive morphology persisted. Astrogliosis was evident in at all CPZ timepoints however was most pronounced after 3 and 6wks of CPZ diet (**Figure 5.3A, C**).

Axon damage has been reported in the corpus callosum after 3, 6, 9, and 12wks of CPZ diet, after focal demyelination with lysolecithin, and in MS lesions (Crawford et al., 2009b; Lapato et al., 2017; Schultz et al., 2017; Yamate-Morgan et al., 2019). In the EAE

model, axon damage within the optic nerve and optic tract is severe and occurs early(Brambilla et al., 2012; Manogaran et al., 2019; Shindler et al., 2008). To probe potential deficits in axon integrity due to CPZ demyelination, sections containing the optic tract were obtained from normal and 12wk CPZ Thy1-YFP mice in which cell bodies and axons of a subset of excitatory neurons fluoresce green. Normal sections showed intact, aligned, and well-organized axons in the dorsal optic tract (**Figure 5.3D**). Sections from 12wk CPZ mice similarly show undamaged and well-aligned axons.

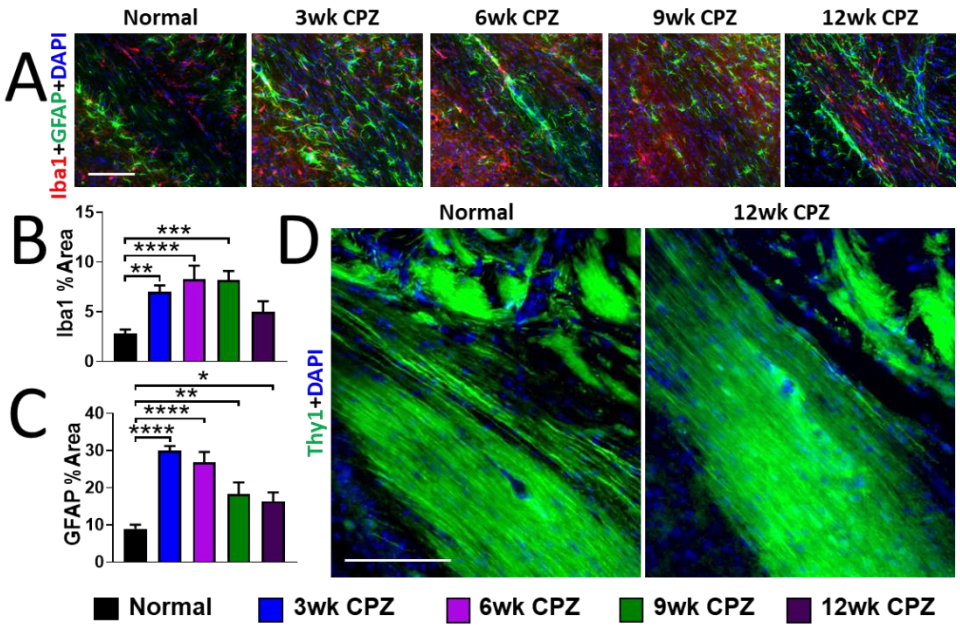

Figure 5.3: CPZ demyelination results in significant microglial activation after 3, 6, and 9wks, and astrogliosis after 3, 6, 9, and 12wks, but does not cause observable axon damage in the optic tract. A. Sections containing optic tract were obtained from normal, 3, 6, 9, and 12wk CPZ PLP-EGFP mice, immunostained for Iba1 and GFAP, and co-stained for DAPI. Normal sections show low levels of Iba1 immunoreactivity, and low levels of GFAP immunoreactivity which are highest at the borders of the optic tract. Sections from mice after 3, 6, and 9wk CPZ show high levels of Iba1, with microglia exhibiting hypertrophied morphology. Sections from 12wk CPZ mice similarly show hypertrophied microglia, but an overall decrease in Iba1 immunoreactivity. Astrogliosis as evidenced by GFAP staining is highest in 3 and 6wk CPZ sections, but still higher than normal in 9wk and 12wk. **B-C.** Quantification of Iba1 and GFAP immunoreactivity show significant increases in Iba1 at 3, 6, and 9wk, and in GFAP at all CPZ timepoints, compared to normal. **D.** Optic tract sections were obtained from normal and 12wk CPZ Thy1-YFP mice. Normal and CPZ sections show intact and well aligned axons with no observable damage in 12wk CPZ. *n*=5 mice per group. **P*<0.05, ***P*<0.001, *** *P*<0.001, **** *P*<0.0001, ordinary one-way ANOVA with Kruskal-Wallis multiple comparison test. Scale bar is 100µm.

Progressive demyelination and OL loss are observed in the dLGN of CPZ mice.

The LGN is important for visual processing and the transference of visual information from the retina to the visual cortex. Maintenance of myelination, glial homeostasis, and neuronal health is crucial for proper function. As recently reported by Araújo and colleagues, the mouse dLGN undergoes significant myelin loss after 3 and 5wks of CPZ diet which is associated with increased microglial and astrocytic presence and changes to the balance between excitation and inhibition after 5 weeks (Araujo et al., 2017). MS patients also present with LGN atrophy which may be indicative of myelin loss and neuronal damage(Papadopoulou et al., 2019; Sepulcre et al., 2009). Such imbalances could lead to progressive functional deficits in LGN visual processing. However, a longitudinal time course study on LGN myelination, and changes to glial and neuronal populations under CPZ challenge has not been previously described.

To assess progressive changes to LGN myelination in the CPZ model, coronal sections containing the dLGN were obtained from normal, 3, 6, 9, and 12wk CPZ PLP-EGFP mice. Sections were immunostained for MBP, then co-stained for DAPI. Normal sections showed laminar layers of MBP immunoreactivity corresponding to myelinated fiber tracts within the LGN (**Figure 5.4A**). Sections from 3wk CPZ mice showed disorganization of fiber tracts, as well as demyelinated areas. Remaining sections showed progressive decreases in myelination which reached significance in relation to normal after 9 and 12 wks CPZ diet (**Figure 5.4A, C**). To evaluate changes to OL populations in the LGN, sections were immunostained for CC1 and co-stained with DAPI. Normal sections

exhibited high numbers of PLP$^+$ premyelinating and CC1$^+$ mature myelinating OLs, in conjunction with PLP$^+$ myelinated fiber tracts (**Figure 5.4B**). CPZ diet resulted in significantly decreased numbers of PLP$^+$ cells after 6wks and 12wks of CPZ diet, and CC1$^+$ cells at the 6 and 9wk timepoint (**Figure 5.4B, D, E**).

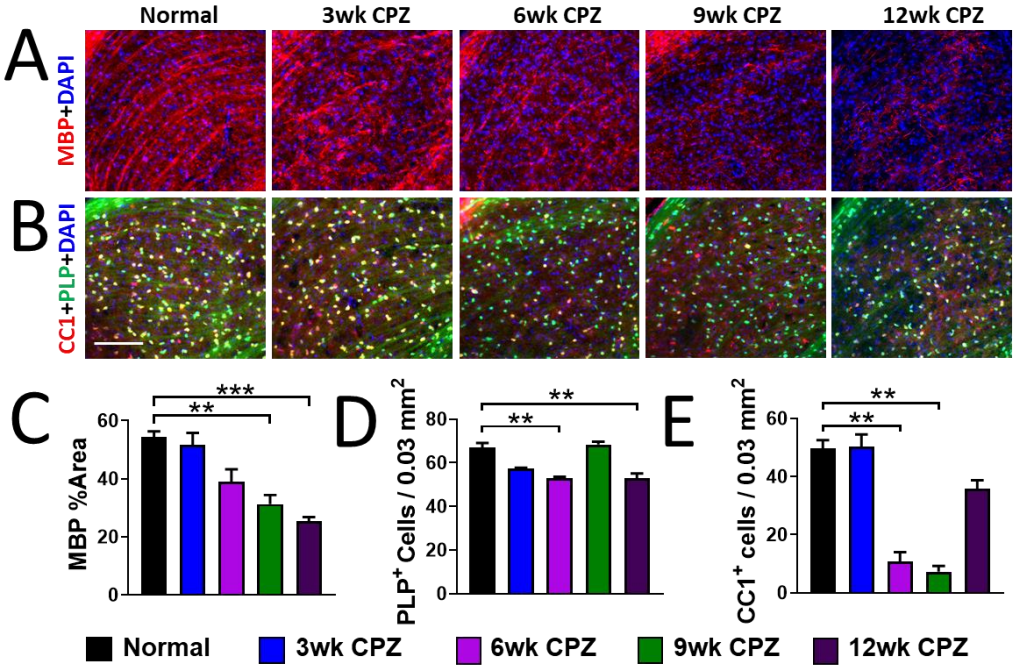

Figure 5.4: CPZ diet results in progressive demyelination of the dLGN, coupled with changes to OL populations. A. Coronal sections containing the dLGN were obtained from normal 3, 6, 9, and 12wk CPZ PLP-EGFP mice, immunostained for MBP, and co-stained for DAPI. Sections were imaged at 20x magnification. Normal sections show laminar myelinated tracts interspersed with regions with low MBP immunoreactivity. CPZ diet results in progressive loss of myelin and little myelin remaining after 9 and 12wks CPZ diet. **B.** Sections from PLP-EGFP mice were immunostained for CC1 and co-stained with DAPI. Normal sections show a high density of PLP$^+$ and CC1$^+$ cells. CPZ diet results in regional decreases in PLP$^+$ cells and CC1$^+$ cells between 6 and 12wks. **C.** Quantification of MBP percent area reveals progressive decreases in dLGN myelination which reach significance compared to normal after 9 and 12wks of CPZ diet. **D-E.** Cell counts of PLP$^+$ and CC1$^+$ cells show significantly decreased numbers of PLP$^+$ cells after 6 and 12wks CPZ diet, and decreased numbers of CC1$^+$ cells after 6 and 9wks CPZ diet. n=5 mice per group. $^{**}P<0.001$, $^{***}P<0.001$, ordinary one-way ANOVA with Kruskal-Wallis multiple comparison test. Scale bar is 100µm.

CPZ demyelination results in early inflammatory responses, decreases in PV immunoreactivity in the dLGN.

To quantify the extent of microglial activation and astrogliosis in the dLGN throughout progressive CPZ-induced demyelination, coronal sections from PLP-EGFP normal, 3, 6, 9, and 12wk CPZ mice were immunostained for Iba1 and GFAP, then co-stained with DAPI. Normal sections displayed Iba1 immunoreactivity throughout the dLGN with microglia exhibiting ramified and thus "resting" morphology (**Figure 5.5A**). In contrast, GFAP immunoreactivity was present primarily at the borders of the LGN. Sections from CPZ mice showed increased Iba1 immunoreactivity compared to normal after 3 and 6wks of CPZ diet but not at later timepoints such as 9 and 12wk (**Figure 5.5A, C**). GFAP immunoreactivity was increased compared to normal after 3, 9 and 12wks of CPZ diet but not at 6wks (**Figure 5.5A, D**).

To evaluate CPZ mediated effects on neuronal populations in the dLGN, sections were immunostained for NeuN and PV, then co-stained with DAPI. In normal sections, NeuN staining was localized to neuronal nuclei and remained fairly consistent across CPZ groups (**Figure 5.5B**). Normal sections exhibited PV staining in a high density of fibers primarily localized within the core of the dLGN. The pattern of PV immunoreactivity changed substantially as CPZ demyelination progressed, with ectopic axonal staining evident in 12wk CPZ sections both within the core and shell of the dLGN (white arrows). PV immunoreactivity was also significantly decreased after 9 and 12wks of CPZ diet, however the number of $NeuN^+$ cells was unchanged at all CPZ timepoints compared to normal (**Figure 5.5E, F**).

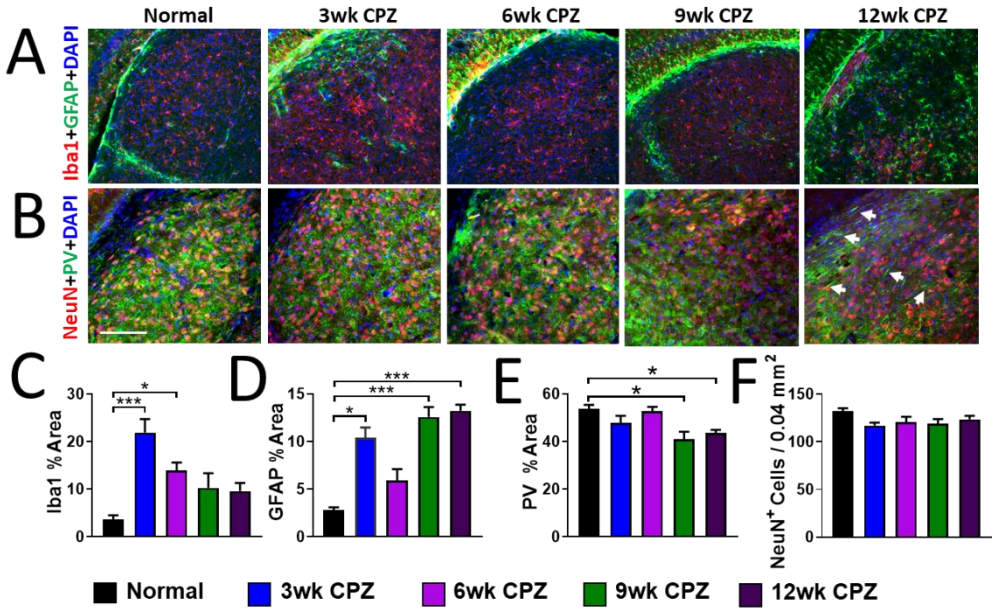

Figure 5.5: CPZ demyelination induces early inflammatory responses, some of which are resolved, and decreases in PV immunoreactivity late in disease within the dLGN. A. Coronal sections containing the dLGN were obtained from PLP-EGFP mice, immunostained for Iba1 and GFAP, co-stained for DAPI, and imaged at 20x magnification. Normal sections show Iba1$^+$ microglia throughout the dLGN with ramified morphology, and GFAP$^+$ astrocytes primarily constrained to the borders of the dLGN. Sections from 3wk CPZ mice show increases in overall microglial immunoreactivity and the presence of two lesions. Microglia which are not present in the lesions maintain a ramified structure, however those comprising the lesion appear hypertrophied. No lesions are observed in sections from 6wk CPZ mice however Iba1 immunoreactivity remains high compared to normal sections. Sections from 9wk CPZ mice show decreased Iba1 immunoreactivity throughout the dLGN, whereas 12wk CPZ sections show areas of high microglial presence indicative of lesions, and areas almost completely absent of microglia. GFAP$^+$ astrocytes show significant infiltration into the dLGN from the dorsal borders after 3wk CPZ diet. A few astrocytes are present in the interior of the dLGN after 9wk CPZ diet. Sections from 12wk CPZ mice exhibit extensive astrocytic presence within the interior of the dLGN, primarily bordering lesions containing high numbers of microglia. **B.** Sections were immunostained for NeuN and PV and imaged at 20x. NeuN immunoreactivity is localized to neuronal nuclei, and remains relatively consistent between normal and CPZ groups. PV immunoreactivity in normal sections is primarily localized to neuropil in the dLGN. CPZ groups exhibit substantial changes to pattern of PV immunostaining and decreased overall PV immunoreactivity after 9 and 12wks of CPZ diet. Sections from 12wk CPZ mice also show ectopic PV axonal staining indicated by the white arrows. **C.** Iba1 immunoreactivity is significantly increased compared to normal after 3 and 6wks of CPZ diet, but is decreased to a point not significantly different from normal at 9 and 12wks. **D.** GFAP immunoreactivity is significantly increased compared to normal after 3, 9 and 12wks CPZ diet, but not at 6wks. **E.** PV percent area is significantly decreased after 9 and 12wks of CPZ diet compared to normal. **F.** The number of NeuN$^+$ cells is unchanged between groups. n=5 mice per group. *P<0.05, *** P<0.001, **** P<0.0001, ordinary one-way ANOVA with Kruskal-Wallis multiple comparison test. Scale bar is 100µm.

CPZ diet induces progressive demyelination and OL loss in the visual cortex.

The visual cortex undergoes significant pathological changes in MS and in EAE including decreased volume and demyelination(Gabilondo et al., 2014; Gabilondo et al., 2017; Girolamo et al., 2011; Petracca et al., 2017). As described, the CPZ diet induces demyelination, inflammatory responses, astrogliosis and neuronal loss in more anterior portions of the visual pathway. Because the visual cortex is susceptible to demyelination and inflammation induced neurodegenerative deficits, as well as trans-synaptic neurodegeneration(You et al., 2012), an assessment of CPZ diet effects within the visual cortex was necessary. V1 is the primary image forming locus of the visual system and thus pathological changes due to CPZ diet may have significant implications for afferent visual system function.

To determine CPZ diet induced changes to V1 myelination and OL populations, sections were obtained from normal, 3, 6, 9, and 12wk CPZ PLP-EGFP mice, and immunostained for MBP and CC1. Sections from normal mice showed high levels of MBP immunoreactivity throughout the cortex, with slightly lower levels within the superficial layers and layer 5-6 (**Figure 5.6A**). Similar to the LGN, V1 exhibited progressive demyelination which reached significance compared to normal after 9 and 12wks of CPZ diet (**Figure 5.6A, C**). In normal sections, PLP^+ premyelinating and mature myelinating OLs, and $CC1^+$ mature myelinating OLs, were observed throughout layer 4 at medium densities, with many cells expressing both markers (**Figure 5.6B**). The number of PLP^+ cells in CPZ sections showed progressive decreases which reached significance after 9 and

12wk CPZ diet (**Figure 5.6B, D**). In contrast, $CC1^+$ cell number was significantly reduced compared to normal controls by at least 6-fold after 6, 9, and 12wks of CPZ diet (**Figure 5.6B, E**).

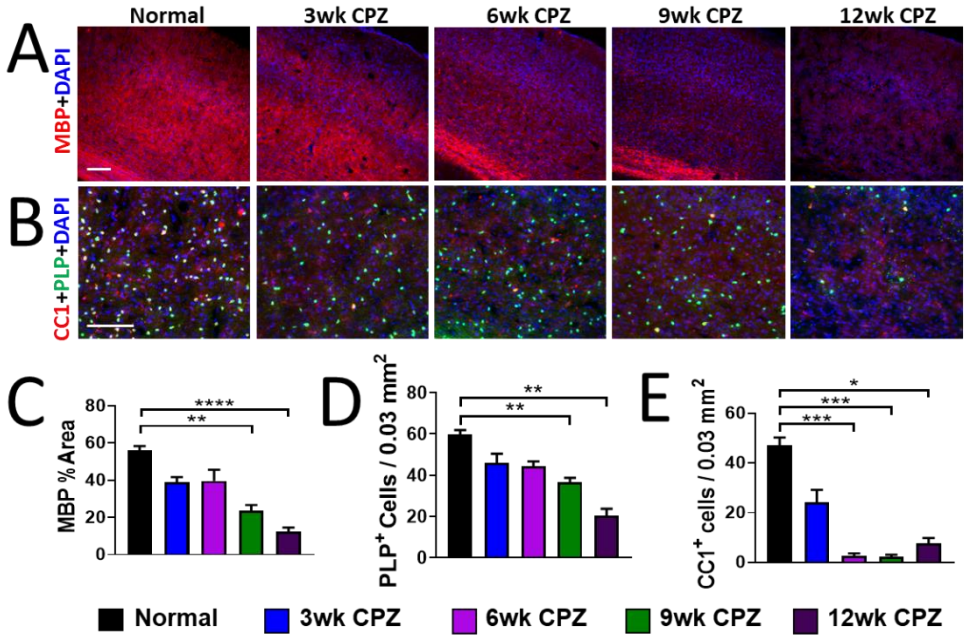

Figure 5.6: Progressive demyelination and OL loss are evident in V1 of CPZ mice. A. Coronal sections containing V1 were obtained from normal controls, and 3, 6, 9, and 12wk CPZ PLP-EGFP mice, immunostained for MBP, co-stained for DAPI, and imaged at 10x magnification. Normal sections show robust myelination throughout V1 with some decreases evident in superficial cortical layers and layer 5-6. CPZ diet results in progressive decreases in cortical myelination which are evident as early as after 3wks of CPZ diet. After 9wks, almost no cortical myelin remains, and after 12wks, callosal myelin is severely depleted as well. **B.** Sections were immunostained for CC1, co-stained for DAPI, and imaged at 20x magnification. Normal sections show high numbers of PLP^+ cells and $CC1^+$ cells at medium densities throughout layer 4 of V1. CPZ diet resulted in a progressive decrease in PLP^+ cells, and $CC1^+$ cells. **C.** Quantification of MBP percent area revealed progressive demyelination in V1 which reaches significance after 9 and 12wks CPZ diet. **D.** Progressive loss of PLP^+ cells reaches significance after 9 and 12wks of CPZ diet. **E.** $CC1^+$ cell numbers are significantly decreased after 6, 9 and 12wks of CPZ diet. *n*=5 mice per group. **P*<0.05, ***P*<0.001, *** *P*<0.001, **** *P*<0.0001, ordinary one-way ANOVA with Kruskal-Wallis multiple comparison test. Scale bar is 100µm.

Early inflammatory responses and late astrogliosis are features of CPZ-induced pathology in the visual cortex.

Astrogliosis and changes to microglial presence in V1 were quantified by immunostaining sections for Iba1 and GFAP. Normal sections showed medium densities of $Iba1^+$ microglia with ramified morphologies indicative of a "resting" phenotype (**Figure 5.7A**). Low densities of $GFAP^+$ astrocytes were present in normal, with primary immunoreactivity exhibited in the meningeal glia limitans border. V1 exhibited increased microglial presence compared to normal primarily after 3, 6, and 9wks of CPZ diet (**Figure 5.7A, C**). In contrast significant increases to GFAP immunoreactivity were not observed until after 9 and 12wks of CPZ diet (**Figure 5.7A, D**). Changes to microglia and astrocytes in V1 are in stark contrast to observations in the optic tract (**Figure 5.3A-C**) and dLGN (**Figure 5.5A, C, D**), in which astrogliosis occurs early and concurrently with increased microglial presence. Neuron numbers and PV^+ interneurons were quantified by immunostaining V1 sections for NeuN and PV. Normal sections showed high densities of smaller $NeuN^+$ cells within layer 4A and 4C, and low densities of larger neurons in layer 4B. PV^+ cells were present throughout layer 4 but at lower densities than $NeuN^+$ cells. PV^+ neuropil was also observed, primarily within layer 4B (**Figure 5.7B**). No significant differences in neuronal populations were observed between groups (**Figure 5.7B, E, F**). There were, however, CPZ-induced decreases in PV^+ neuropil staining compared to normal in 3, 6, and 12wk CPZ sections (**Figure 5.7B**).

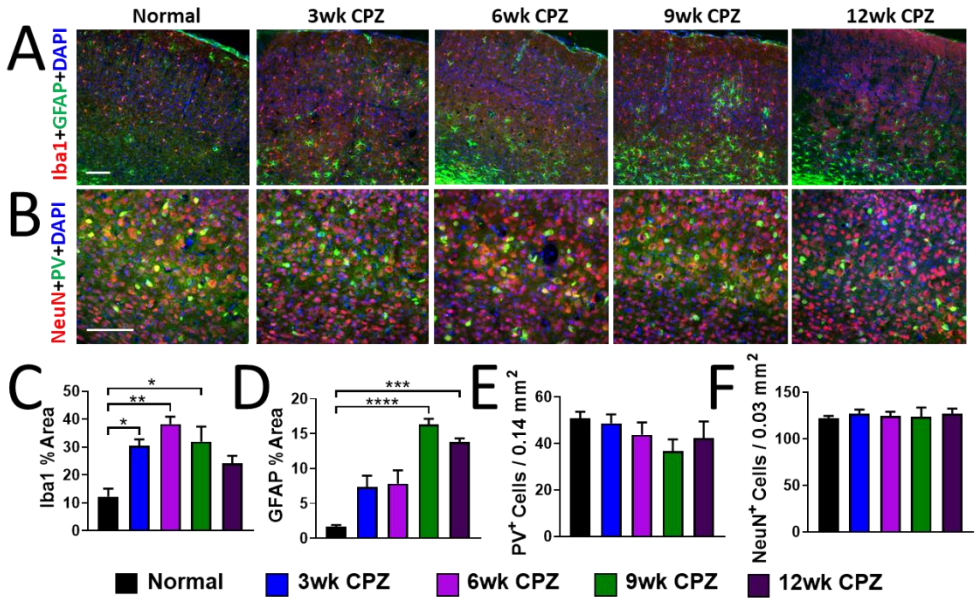

Figure 5.7: Toxic CPZ diet induces early microglial activation and late astrogliosis, but insignificant changes to neuron numbers in V1. A. Coronal sections obtained from normal controls, and 3, 6, 9, and 12wk CPZ PLP-EGFP mice were immunostained for Iba1 and GFAP, co-stained for DAPI, and imaged at 10x magnification. Normal sections show low Iba1 immunoreactivity overall, primarily present in ramified "resting" microglia. GFAP immunoreactivity is also low within the interior of the cortex and is highest within the glia limitans of the meninges. CPZ diet induces increases in V1 Iba1 immunoreactivity in sections from 3, 6, 9 and 12wk CPZ mice, and V1 GFAP immunoreactivity in sections from 9 and 12wk CPZ mice. **B.** Sections were immunostained for NeuN and PV, co-stained for DAPI, and imaged at 20x magnification. Normal sections show high densities of small $NeuN^+$ cells in layers 4A and 4C, and medium densities of large $NeuN^+$ cells in layer 4B. PV immunoreactivity is evident in low densities of neurons interspersed throughout layer 4, and neuropil primarily within layer 4B. Sections from CPZ diet mice exhibit similar numbers of $NeuN^+$ cells and PV^+ cells throughout layer 4, but decreased PV^+ dendritic staining within layer 4B. **C-D.** Quantification of Iba1 and GFAP immunoreactivity reveals significantly increased microglial presence after 3, 6, and 9wks, and significant astrogliosis after 9 and 12wks of CPZ diet. **E-F.** No differences in $NeuN^+$ or PV^+ cells are observed between groups. n=5 mice per group. *P<0.05, **P<0.001, *** P<0.001, **** P<0.0001, ordinary one-way ANOVA with Kruskal-Wallis multiple comparison test. Scale bar is 100µm.

Axons of RGCs, which leave the retina and comprise the optic nerve are demyelinated and undergo significant changes to inflammatory glial populations under the toxic CPZ diet. Demyelination, astrogliosis, and microglial activation after lipopolysaccharide injection into the optic nerve are associated with upstream RGC loss (Aranda et al., 2015), similar to events observed in EAE(Jin et al., 2019). Such pathological

deficits in the CPZ model may precipitate upstream RNFL and RGC degeneration and dysfunction.

Additionally, photoreceptors within the retina have high energy demands and rely heavily on their mitochondria for phototransduction of light stimuli(Country, 2017). Cells of the RPE are also involved in phototransduction and similarly require high levels of ATP(Country, 2017). Because CPZ-induced damage to OLs is thought to be partially mediated by insufficient energy production due to significant deficiencies in copper availability, photoreceptors and pigment epithelial cells within the retina may similarly be susceptible to CPZ-induced damage and functional deficits.

CPZ diet results in posterior retinal pathology.

To evaluate retinal pathology in the CPZ model, retinas of live anesthetized normal and CPZ diet PLP-EGFP mice were examined using OCT after 3, 6, 9, and 12wks of CPZ diet. OCT dataplots of the temporal retina were obtained just lateral to the optic nerve (**Figure 5.8A-i**). Bioptigen/Leica software was used to automatically segment retinal layers (**Figure 5.8A-ii**) and quantify the thickness of the whole retina, RNFL, GCL+IPL, INL+OPL, ONL+PR, and RPE. Overall retinal thickness was increased after 6 and 12wks of CPZ diet compared to normal controls (**Figure 5.8B**). Interior retinal layers including the RNFL, GCL+IPL, and INL+OPL were not changed at any CPZ timepoint. The PL exhibited significant decreases in thickness after 9 and 12wks of CPZ diet whereas the thickness of the RPE was increased after 6, 9 and 12wks.

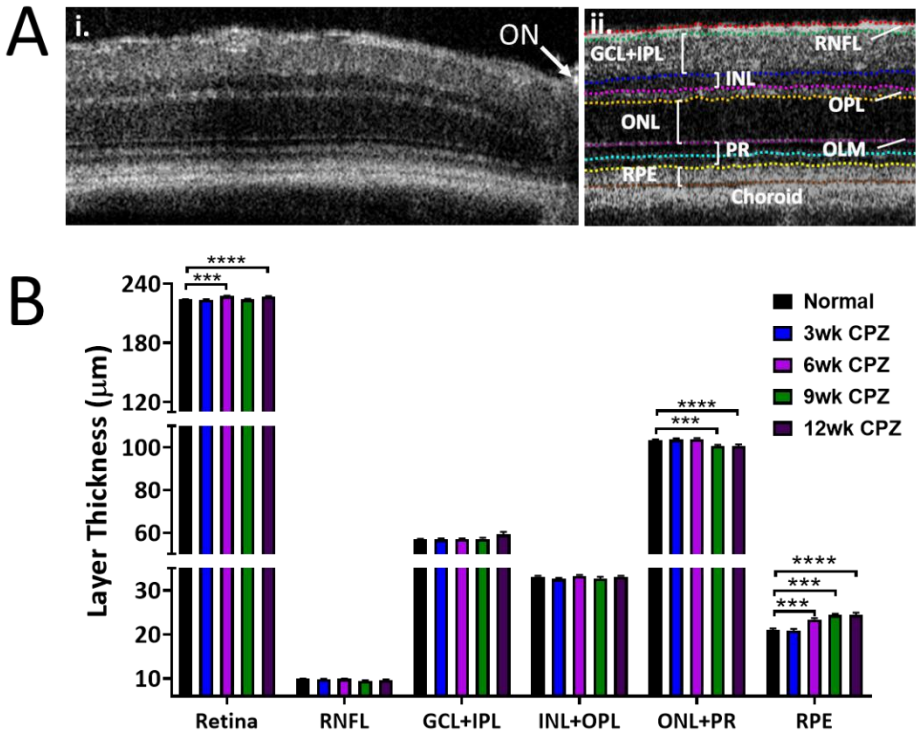

Figure 5.8: CPZ diet induces pathological changes in posterior retinal layers. *In vivo* OCT data plots were obtained from live anesthetized normal controls, and CPZ mice, after 3, 6, 9 and 12wks of CPZ diet. Data plots were analyzed to determine individual layer thicknesses. **A.** Representative OCT data plot of the temporal retina with optic nerve identified for orientation (i). Automatic segmentation was performed using Bioptigen/Leica segmentation software. Retinal layers identified include the RNFL, GCL+IPL, INL, OPL, ONL, OLM, PR, RPE and choroid (ii). **B.** Whole retina thickness is increased compared to normal after 6 and 12wks CPZ diet. RNFL, GCL+IPL, and INL+OPL layers are unaffected throughout CPZ administration. CPZ diet induces significant decreases in ONL+PR thickness after 9 and 12wks, and increases in RPE thickness after 6, 9 and 12wks compared to normal. n=5 mice per group. *P<0.05, **P<0.001, *** P<0.001, **** P<0.0001, ordinary one-way ANOVA with Kruskal-Wallis multiple comparison test. Scale bar is 100µm.

Retinal function is not minimally impaired in CPZ mice.

In order to assess the effect of CPZ demyelination on retinal function, flash ERGs were obtained from live anesthetized normal and CPZ mice after 3, 6, 9, and 12wks of CPZ diet. Normal ERGs consist of an initial downward deflection of the ERG occurring around 20ms and labeled as the A-wave, followed by a sharp increase in electrical potential

peaking at 40ms and referred to as the B-wave (**Figure 5.9A**). Normal amplitudes average at approximately 200 µV for the A-wave and 500µV for the B-wave. CPZ mice exhibited minimal deficits in retinal function compared to normal controls. Photoreceptor generated A-wave response time to stimulus were unaffected at all CPZ timepoints (**Figure 5.9B**). However, B-wave response time to stimulus, a result of retinal interneuron, RGCs, and Muller glia activity, were decreased compared to normal controls after 6 and 12wks of CPZ diet, indicating hyperactivity of those cell types. Neither A-wave nor B-wave amplitudes were significantly changed in CPZ diet groups (**Figure 5.9C**).

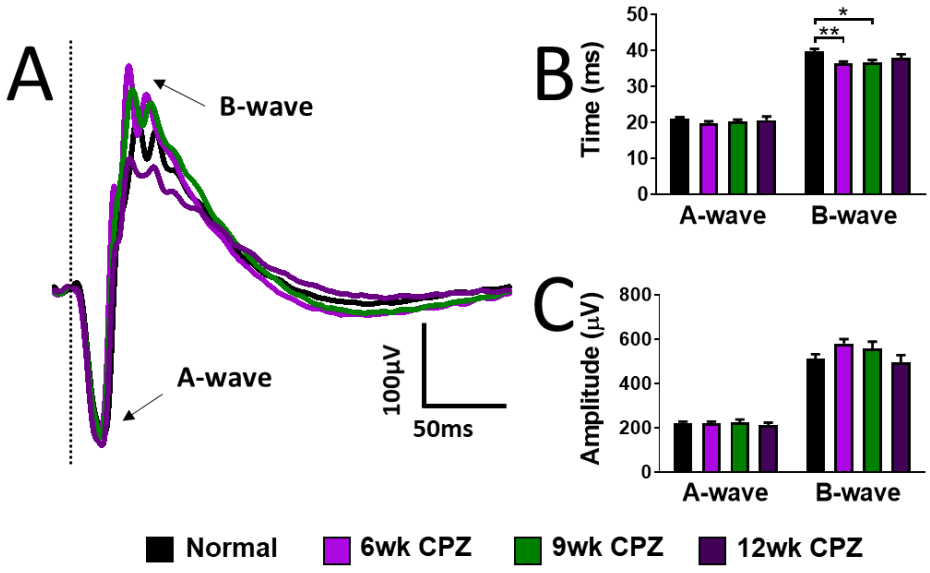

Figure 5.9: Retinas of CPZ mice exhibit few functional deficits. ERGs were obtained from live anesthetized normal controls, and CPZ mice after 6, 9, and 12wks of CPZ diet. **A.** Sample traces obtained by averaging ERG traces of all mice in individual experimental groups. A-wave and B-wave are identified for orientation. In the normal ERG trace, the A-wave occurs at approximately 20ms with an amplitude of 200µV. The B-wave occurs around 40ms with an amplitude of approximately 500µV. Traces from 6 and 9wk CPZ groups exhibit slightly faster A- and B- wave response times, as well as increased B-wave amplitudes compared to normal. **B.** Quantification of A- and B-wave response times reveal no significant differences in A-wave latencies between groups, but significant decreases in B-wave response times after 6 and 9wks of CPZ diet. **C.** Neither A- nor B- wave amplitudes are significantly different between normal and CPZ groups. *n*=5 mice per group. *P<0.05, **P<0.001, ordinary one-way ANOVA with Kruskal-Wallis multiple comparison test.

Visual function is partially impaired in CPZ mice.

To investigate CPZ-induced effects on visual pathway function, *in vivo* flash VEPs were obtained from live anesthetized normal or 6, 9 and 12wk CPZ mice. Normal mice exhibited robust VEPs, with P1 peaks typically occurring 20ms after stimulus, and with amplitudes of approximately 50µV (**Figure 5.10A**). N2 peaks occurred approximately 40ms after stimulus and had an average amplitude of 90µV. The CPZ diet resulted in few changes to VEPs compared to normal. The P1 latency of 9wk CPZ mice was significantly decreased, and the N2 amplitude of 6wk CPZ mice significantly increased compared to normal (**Figure 5.10B, C**).

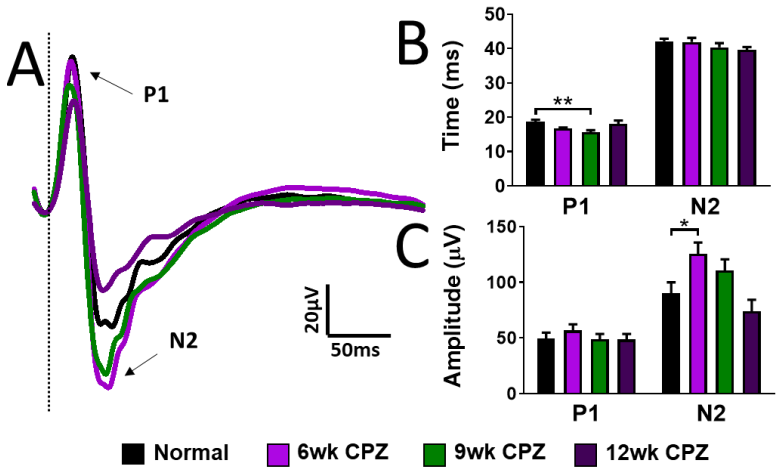

Figure 5.10: CPZ diet and visual pathway demyelination elicits minimal changes to visual pathway function. VEPs were obtained from live anesthetized normal controls, and CPZ mice after 6, 9, and 12wks of CPZ diet. **A.** Sample traces obtained by averaging VEP traces of all mice in individual experimental groups. P1 and N2 peaks are identified for orientation. In the normal VEP trace, the P1 occurs at approximately 20ms with an amplitude of 50µV. N2 occurs around 40ms with an amplitude of approximately 90µV. Representative trace from the 6wk CPZ group shows higher N2 amplitude than those generated by normal controls. Representative trace from the 9wk CPZ group exhibits slightly faster P1 response time, and increased B-wave amplitude compared to normal. **B.** Quantification of P1 and N2 response times reveals no significant differences in latencies between groups, except for a latency decrease in the P1 peak of 9wk CPZ mice with respect to normal. **C.** P1 amplitudes are not changed between normal and CPZ groups, however the N2 amplitude is significantly increased at the 6wk CPZ timepoint compared to normal. *n*=5 mice per group. *P<0.05, **P<0.001, ordinary one-way ANOVA with Kruskal-Wallis multiple comparison test.

Discussion

In contrast to EAE, CPZ diet induced progressive and extensive demyelination across the posterior visual pathway which was not coupled to overt functional deficits or axon damage. Furthermore, CPZ animals exhibited increased levels of microglial activation throughout disease progression. Microglia may have exerted neuroprotective effects during CPZ demyelination that were not available in EAE.

CPZ-induced demyelination, microglial inflammation, and astrogliosis

During CPZ demyelination, mature OLs undergo apoptosis resulting in microglial recruitment and subsequent demyelination(Matsushima and Morell, 2001). Activated Microglia/macrophages are present in the corpus callosum within 2 weeks of starting CPZ diet, increased at 3 weeks, and peak between 4-6 weeks(Hiremath et al., 1998). In fact, the only immune cells which have been found in demyelinated areas are microglia and macrophages (Hiremath et al., 2008). Similar to the above reports, we observed increased levels of microglial presence prior to overt demyelination in posterior visual pathway structures. We did not observe any changes to axon morphology indicating that CPZ demyelination did not result in significant axonal damage in the posterior visual system.

This result was in stark contrast to the EAE model in which demyelination and severe OL loss preceded overt microglial presence, and subsequent axonal damage. Although the lack of microglial activation was surprising in EAE, the notable absence may have contributed to the severity of axon damage later occurring in the optic tract, and progressive neuronal loss in V1.

Among other roles, microglia/macrophages work to clear myelin debris at demyelination sites(Blakemore, 1972; Smith, 1999). Furthermore, when exhibiting an immunomodulatory M2 phenotype, they promote OPC migration survival and differentiation (Butovsky et al., 2006; Miron et al., 2013; Miron, 2017; Morell et al., 1998; Pang et al., 2013). In the CPZ model, microglia may express a similar M2 phenotype during demyelination, as waves of remyelination were observed in the optic tract at 9wks, and the number of OLs was not as severely depleted in most posterior visual pathway areas as in EAE.

Microglia have also been shown to directly protect neurons during disease. Under injury conditions, microglia have been shown to ensheathe injured neurons and reversibly strip axosomatic inhibitory synapses, in a mechanism that is associated with neuroprotection from subsequent damage(Blinzinger and Kreutzberg, 1968; Chen et al., 2012; Chen et al., 2014). The removal of inhibitory synapses by microglia can result in increased firing of synaptic NMDA receptors, which has been shown to stimulate anti-apoptotic and anti-necrotic pathways(Chen et al., 2014; Hardingham and Bading, 2003).

In the posterior visual pathway, we observed increased microglial presence, decreases in the area covered by PV^+ neuropil in the dLGN, faster VEP response times to light stimulus, and increased VEP amplitudes. Taken together these CPZ-induced changes are indicative of decreased inhibition within the visual pathway. Hyperactivity in CPZ mice is not limited to the visual pathway. Our lab and others have previously reported significant increases in seizure activity in CPZ mice, indicating a loss of inhibition in other CNS

regions (Hoffmann et al., 2008; Lapato et al., 2017). It is possible that increased hyperactivity of visual pathway function during CPZ diet may have been associated with microglial removal of inhibitory synapses in the posterior visual system, however further investigation is necessary.

Astrocytic activation was increased throughout CPZ demyelination in the optic tract, and primarily after 9 and 12wks of CPZ in the dLGN and V1. Studies from our lab and many other studies have reported similar CPZ-induced increases in astrogliosis in other CNS regions such as the corpus callosum (Carlton, 1969; Gudi et al., 2009; Lapato et al., 2017; Yamate-Morgan et al., 2019), hippocampus (Koutsoudaki et al., 2009; Lapato et al., 2017), cortex(Skripuletz et al., 2008), cerebellum (Skripuletz et al., 2010), and basal ganglia (Pott et al., 2009). Under CPZ demyelination conditions, astrocytes produce growth factors that like microglial derived compounds, promote OPC proliferation, and regulate OL differentiation and survival (Gudi et al., 2014). Astrocytes also assist microglia in their invasion of demyelinated lesion sites and their ablation results in delayed removal of myelin debris, OPC proliferation, remyelination, and decreased numbers of mature OLs during remyelination (Skripuletz et al., 2013). As such astrocytes may also exert a neuroprotective role during CPZ-induced demyelination of the visual pathway, and cross-talk between astrocytes and microglia may also have contributed to the decreased level of neuronal damage observed in CPZ as compared to EAE.

Retinal Pathology

CPZ diet resulted in changes in retinal layer thickness that were confined to the posterior retina. The layers corresponding to the photoreceptors were significantly decreased after prolonged CPZ diet, whereas the RPE layer thickened. RPE thickening preceded thinning of the PLs indicating that RPE dysfunction may have precipitated changes to the PL. Interestingly, morphological changes to the PLs did not result in direct functional deficits, as the A-wave of the ERG was unaffected.

Thickening of the RPE has been reported in MS patients with optic neuritis(Droby et al., 2016) and in pathological conditions associated with chronic inflammatory retinal damage (Bonilha, 2008; Curcio et al., 2017; Gao and Hollyfield, 1992; Penfold et al., 2001). Because photoreceptors rely heavily on the RPE for, re-isomerization of all-*trans*-retinal to 11-*cis*-retinal, stabilizing ion composition in sub-retinal space and maintaining photoreceptor excitability, and phagocytoses of shed photoreceptor outer segments, RPE dysfunction is often associated with photoreceptor and retinal dysfunction (Strauss, 2005). In addition, the RPE has a primary role in transporting ions and metabolic waste from the subretinal space to the blood, transfer of nutrients from the blood to the subretinal space, secretion of immunosuppressive factors, and maintenance of the blood retinal barrier (Strauss, 2005). Thus CPZ-induced disruptions to the RPE could have significant effects on retinal health, however further histological study is required to characterize cellular changes in the retina during CPZ demyelination.

ERG

Retinal function as measured by ERGs was somewhat enhanced during CPZ demyelination. ERG amplitudes were not significantly changed, however showed trends toward increases at the 6 and 9wk timepoint. In contrast, one study of retinal function in CPZ showed decreased amplitude of multifocal ERG (mfERG) after 6wks of CPZ diet, contrary to our results (Namekata et al., 2014). The mfERG is the result of simultaneous recordings of local ERG responses across many regions in the retina(Hood et al., 2003). In contrast, the flash ERG used in this study utilizes one electrode to determine overall retinal function. The stimulus paradigm is also vastly different in mfERGs, where rather than one single illuminating stimulus across the retina, there are a number of hexagonal stimuli which can be independently black or white at any given moment. As such, mfERGs can confer changing edge-specific stimuli to retinal neurons. This results in increased sensitivity to contrast-based deficits in the retina, which is not present in the flash ERG and may explain the differing results observed.

Decreased latency of the b-wave was observed in CPZ mice after 6 and 9wks, contrary to most results reported in MS patients in which b-wave latencies are either unaffected or delayed (Coupland and Kirkham, 1982; Hamurcu et al., 2017; Papakostopoulos et al., 1989). However, one recent study in MS patients similarly reported shortened latencies of the b-wave in pattern ERGs which are particularly sensitive to RGC activity (Monsalve et al., 2018). Monsalve and colleagues suggested that the increased susceptibility of slower spiking midget RGCs to MS-induced optic neuritis, resulted in a dropout of the contribution of these cells to the ERG, and thus faster overall latencies. Midget RGCs contribute primarily to the parvocellular pathway, are particularly important

for identifying fine details (Sanes and Masland, 2015). The study confirmed that blurring the edges of the pattern stimuli presented to normal patients, resulted in similar decreases in latency (Monsalve et al., 2018). Furthermore, midget RGCs and the parvocellular pathway have been previously been reported to be less robust to demyelination and axon damage than their magnocellular counterparts (Evangelou et al., 2001; Mey and Thanos, 1993; Perez de Sevilla Muller et al., 2014).

Although overt axon damage axon damage was not observed in the optic tract in CPZ mice, significant demyelination occurred. In fact virally induced demyelination of the visual pathway including the optic nerve has also been shown to enhance ERG responses rather than depress them (Tansey et al., 1986). To investigate the mechanisms associated with demyelination induced enhancement of retinal responses, future studies may require evaluating responses to pattern evoked potentials and histological assessments of midget and parasol ganglion cells in 6 and 9wk CPZ mice.

In conclusion, the CPZ model can be employed to study progressive demyelination in the visual pathway separate from peripheral immune involvement and axon damage. Additionally, the potential neuroprotective role which microglia and astrocytes may have under demyelinating conditions is intriguing and requires further study.

Chapter 6: Conclusion and prospects

6.1 Summary of Major Results

In the preceding work, the efficacy of the known remyelinating agent IndCl for ameliorating visual pathway dysfunction was evaluated in the EAE mouse model of MS. This model is the most commonly used animal model for MS as it closely recapitulates the inflammatory demyelination and neurodegeneration observed in MS patients. Although IndCl treatment resulted in robust remyelination of the visual pathway, this was not associated with improvements in visual function, in contrast to currently and previously published improvements to motor function(Karim et al., 2019b; Moore et al., 2014a). It was hypothesized that a contributing factor to this discrepancy, was the extent of axon damage present in the visual system in EAE mice: because loss of function in MS patients is associated with progressive neuro-axonal damage, a remyelinating agent such as IndCl given after overt neuro-axonal damage, may have been too little too late.

To evaluate this hypothesis, a longitudinal study of EAE induced damage to the visual system was performed, with focus on the posterior visual system, as it has been poorly studied in comparison to the anterior visual system in EAE. EAE mice exhibited significant demyelination and OL loss at all assayed timepoints, but did not show severe axon damage until after peak disease. Functional deficits were observed at all timepoints. This indicated that an ideal therapeutic window could be between disease onset and at peak disease. However further studies are needed in order to:

1. Further define the proposed therapeutic window.

2. Evaluate the efficacy of therapeutic IndCl in attenuating visual pathway dysfunction, if given during the proposed therapeutic window.

Interestingly, ERG and VEP visual response times were increased early in EAE, but were decreased back to normal levels at peak and late disease timepoints. This phenomenon was indicative of spontaneous but partial functional recovery, and supports observations in MS patients with optic neuritis who experience acute vision loss followed by functional recovery. It was hypothesized that rather than being a result of spontaneous remyelination, or progressive dropout of partially demyelinated axons leading to the VEP primarily being contributed to fast-firing surviving axons, this event was due to reorganization of sodium channels within the white matter tracts of the visual pathway. However further study is required in order to:

3. Assess the progression of sodium channel reorganization in the optic nerve and optic tract.

Posterior visual pathway pathology was then longitudinally investigated in another commonly used animal model for MS, the CPZ demyelination model. Progressive demyelination was observed in this model, but OL loss was not as severe as observed in EAE, and axonal damage was not evident. Major differences between EAE and CPZ pathological deficits include the presence of peripheral immune cell infiltration to the CNS in EAE which is not an aspect of CPZ pathophysiology, and the observed higher levels of microglial activation throughout the posterior visual pathway in CPZ compared to EAE.

Because lymphocytic infiltration has been implicated in exacerbated neuronal damage in MS, and because microglia have been shown to exert neuroprotective effects on the CNS during CPZ demyelination, it is postulated that these two factors may have may have contributed to the exacerbated neurodegenerative damage in EAE. However, further studies are needed to:

4. Investigate which aspect of the immune response contributes to axon damage in the visual pathway.

6.2 Future Directions

1. **Further investigation of the proposed therapeutic window**

   Future studies will require further examining the therapeutic window proposed in this dissertation to determine an optimal timepoint for IndCl delivery to attenuate visual pathway pathology. The ideal period would be after visual deficits have been observed, such that subsequent findings would be translationally relevant, but before overt axon damage. Furthermore, it is necessary to define a point after which therapeutic treatment with IndCl, could no longer exert benefits to visual function. Thus, it may be necessary to perform another longitudinal study constrained to the times between EAE onset and EAE peak disease, and to observe changes to axon morphology in the optic nerve and optic tract, as well as concurrent changes to visual function.

2. **Evaluation of the efficacy of therapeutic IndCl in attenuating visual pathway dysfunction, if given during the proposed therapeutic window.**

In conjunction with the proposed longitudinal study between EAE onset and peak disease IndCl could be provided to a separate cohort of EAE mice starting at each timepoint assessed in the longitudinal study, and through euthanasia. Axon damage and neuronal loss could be assessed for each IndCl treatment group to determine whether early remyelination with IndCl treatment prevents further axonal damage. ERG and VEP functional assessments could also be performed on each treatment group prior to euthanasia to determine the extent of axon damage that can occur before treatment with IndCl becomes ineffective.

3. **Assessment of the progression of sodium channel reorganization in the optic nerve and optic tract during EAE.**

Sections containing visual pathway structures from this and other longitudinal studies could be stained for sodium channel markers such as Nav1.2 and Nav1.6 to investigate changes in the distribution of sodium channels throughout EAE progression. Special focus could be given to the time periods between EAE induction and EAE onset, and between EAE onset and EAE peak disease as the most drastic changes to the VEP and ERGs during this period.

4. **Investigation of which aspect of the immune response contributes to axon damage in the visual pathway.**

Remyelination was not sufficient to attenuate visual pathway dysfunction in EAE, which in addition to the timing of administration, could also be due to the involvement of peripheral lymphocytes in EAE pathophysiology. To isolate this potential contribution, studies on lymphocyte involvement could be performed

using antibodies against T-cell and/or B-cell subtypes. A humanized version of such antibody alemtuzumab, inhibits T cell responses, alleviates inflammatory responses during relapses, and is already approved for use in MS patients however has limited efficacy in preventing long-term disability progression in MS patients(Ruck et al., 2015). If early axon damage were attenuated in mice treated with alemtuzumab it could indicate that co-therapy with a remyelinating agent such as IndCl and an immunomodulatory agent like alemtuzumab, may improve therapeutic outcomes in the visual system, potentially even if given at peak disease.

Additionally, the peripherally mediated immune response may be dominated by different inflammatory phenotypes at different stages of disease. For instance, early and peak disease stages may be characterized by more pro-inflammatory lymphocytes, and chronic disease stages by more quiescent lymphocytes. Such differences could contribute to demyelination and axonal damage in different ways. The adoptive transfer EAE model, in which encephalitogenic T-lymphocytes are obtained from donor EAE mice and used to induce EAE in a second cohort of naïve recipient mice, could be used to examine the effects of T-lymphocytes obtained at early, peak and late disease stages on demyelination and axon damage in the recipient mouse. Chemokine and cytokine analyses could be performed on donor splenocytes, to ascertain the phenotypic profile of these cells at different EAE timepoints, and potentially to correlate pathological deficits in myelination and axon health to differential cytokine and chemokine production. This could yield more focused immunomodulatory

therapeutic targets that could be provided in conjunction with a remyelinating agent.

The results of the preceding study indicate that administration of remyelinating agents at peak disease is insufficient to recover axons, and that early administration prior to overt axon damage may be necessary to generate functional benefits. Future studies should thus investigate the therapeutic potential of remyelinating agents for the visual pathway when provided soon after disease onset. However, such an approach is not always possible in MS patients who may not be diagnosed with MS-induced visual deficits until significant neurodegeneration within the visual pathway has occurred. As such, approaches that can be used outside of the proposed therapeutic window, between onset and peak clinical disease, are necessary. The extensive axon damage evident in the lymphocyte-mediated EAE model is in sharp contrast to the minimal effects on axon and neuron health observed in the non-lymphocyte-mediated CPZ model within the visual system. These differential effects indicate a potential role for lymphocytes in exacerbating axon and neuron damage in the visual system during EAE. Further investigation of the peripherally mediated immune response in EAE may yield therapeutic targets that when combined with remyelinating therapies may attenuate neurodegenerative damage and thus is vital for the progression of MS research.

Appendix

A.1 Supplementary figures

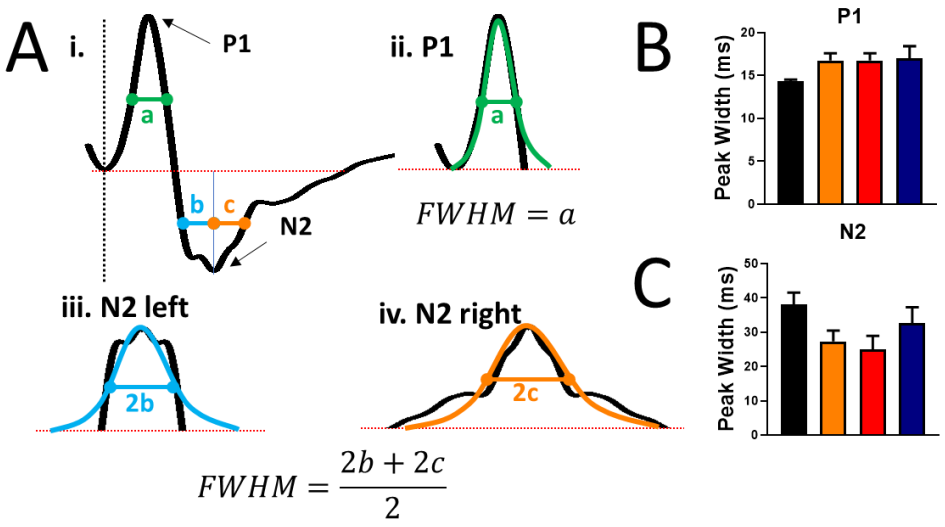

Figure A.1: EAE does not induce significant changes to the broadness of the VEP peak. A. Sample normal VEP trace with widths used for calculating full width half maximums (FWHM) identified (i). P1 peak was plotted from baseline (red dashed line) fitted with gaussian curve (green line), and FWHM (a) was calculated from gaussian curve (ii). N2 peak exhibited asymmetric features. N2 peak was split into individual tails around the N2 peak amplitude. Individual tails were mirrored to generate N2 left peak (iii), and N2 right peak (iv). N2 left and right peaks were fitted with two separate gaussians (blue and orange lines respectively, and individual FWHM values were calculated for each mirrored peak. FWHM values were averaged to approximate FWHM of original N2 data. **B-C.** No significant differences in peak broadness were observed between groups for P1 or N2 peaks.

A.2 References

. MS Prevalence. Vol., ed.^eds. National Multiple Sclerosis Society.

2001. Randomized controlled trial of interferon- beta-1a in secondary progressive MS: Clinical results. Neurology. 56**,** 1496-504.

Agetsuma, M., et al., 2018. Parvalbumin-Positive Interneurons Regulate Neuronal Ensembles in Visual Cortex. Cereb Cortex. 28**,** 1831-1845.

Aharoni, R., et al., 2008. Demyelination arrest and remyelination induced by glatiramer acetate treatment of experimental autoimmune encephalomyelitis. Proceedings of the National Academy of Sciences of the United States of America. 105**,** 11358-11363.

Ahlfors, S.P., Ilmoniemi, R.J., Hamalainen, M.S., 1992. Estimates of visually evoked cortical currents. Electroencephalogr Clin Neurophysiol. 82**,** 225-36.

Al-Abdulla, N.A., Martin, L.J., 2002. Projection neurons and interneurons in the lateral geniculate nucleus undergo distinct forms of degeneration ranging from retrograde and transsynaptic apoptosis to transient atrophy after cortical ablation in rat. Neuroscience. 115**,** 7-14.

Al-Louzi, O.A., et al., 2016. Outer retinal changes following acute optic neuritis. Mult Scler. 22**,** 362-72.

Al-Shamsi, M., et al., 2015. Bioenergetics of the spinal cord in experimental autoimmune encephalitis of rats. BMC Neurosci. 16**,** 37.

Alme, M.N., et al., 2015. Fingolimod does not enhance cerebellar remyelination in the cuprizone model. J Neuroimmunol. 285**,** 180-6.

Andersen, O., et al., 2018. Diffusion tensor imaging in multiple sclerosis at different final outcomes. Acta Neurol Scand. 137**,** 165-173.

Anlar, O., et al., 2003. Visual evoked potentials in multiple sclerosis before and after two years of interferon therapy. Int J Neurosci. 113**,** 483-9.

Aranda, M.L., et al., 2015. Experimental optic neuritis induced by the microinjection of lipopolysaccharide into the optic nerve. Exp Neurol. 266**,** 30-41.

Araujo, S.E.S., et al., 2017. Inflammatory demyelination alters subcortical visual circuits. J Neuroinflammation. 14**,** 162.

Arevalo, M.A., et al., 2010. Actions of estrogens on glial cells: Implications for neuroprotection. Biochim Biophys Acta. 1800**,** 1106-12.

Arezzo, J.C., et al., 1988. Electrophysiological analysis of factors involved in the primary demyelinating diseases: the rabbit eye model system. Brain Res. 462**,** 286-300.

Arshavsky, V.Y., Lamb, T.D., Pugh, E.N., Jr., 2002. G proteins and phototransduction. Annu Rev Physiol. 64**,** 153-87.

Atkinson, K.C., et al., 2019. Diffusion tensor imaging identifies aspects of therapeutic estrogen receptor beta ligand-induced remyelination in a mouse model of multiple sclerosis. Neurobiol Dis. 130**,** 104501.

Azcoitia, I., et al., 2010. Role of astroglia in the neuroplastic and neuroprotective actions of estradiol. European Journal of Neuroscience. 32**,** 1995-2002.

Backner, Y., Levin, N., 2018. Keep Your Eyes Wide Open: On Visual- and Vision-Related Measurements to Better Understand Multiple Sclerosis Pathophysiology. J Neuroophthalmol. 38**,** 85-90.

Backner, Y., et al., 2019. Vision and Vision-Related Measures in Progressive Multiple Sclerosis. Front Neurol. 10**,** 455.

Bakker, D.A., Ludwin, S.K., 1987. Blood-brain barrier permeability during Cuprizone-induced demyelination. Implications for the pathogenesis of immune-mediated demyelinating diseases. J Neurol Sci. 78**,** 125-37.

Balabanov, R., et al., 2006. Suppressor of cytokine signaling 1 expression protects oligodendrocytes from the deleterious effects of interferon-gamma. J Neurosci. 26**,** 5143-52.

Balatoni, B., et al., 2007. FTY720 sustains and restores neuronal function in the DA rat model of MOG-induced experimental autoimmune encephalomyelitis. Brain Res Bull. 74**,** 307-16.

Balcer, L.J., et al., 2015. Vision and vision-related outcome measures in multiple sclerosis. Brain. 138**,** 11-27.

Balcer, L.J., et al., 2017. Validity of low-contrast letter acuity as a visual performance outcome measure for multiple sclerosis. Mult Scler. 23**,** 734-747.

Balk, L.J., et al., 2015. Bidirectional trans-synaptic axonal degeneration in the visual pathway in multiple sclerosis. J Neurol Neurosurg Psychiatry. 86**,** 419-24.

Bannerman, P.G., et al., 2005. Motor neuron pathology in experimental autoimmune encephalomyelitis: studies in THY1-YFP transgenic mice. Brain. 128**,** 1877-86.

Barber, A.N., Ronstrom, G.N., Muelling, R.J., Jr., 1954. DEVELOPMENT OF THE VISUAL PATHWAY: OPTIC CHIASM. JAMA Ophthalmology. 52**,** 447-453.

Baxi, E.G., et al., 2017. Lineage tracing reveals dynamic changes in oligodendrocyte precursor cells following cuprizone-induced demyelination. Glia. 65**,** 2087-2098.

Beck, R.W., et al., 1992. A randomized, controlled trial of corticosteroids in the treatment of acute optic neuritis. The Optic Neuritis Study Group. N Engl J Med. 326**,** 581-8.

Behbehani, R., et al., 2017. Optical coherence tomography segmentation analysis in relapsing remitting versus progressive multiple sclerosis. PLoS One. 12**,** e0172120.

Berkelaar, M., et al., 1994. Axotomy results in delayed death and apoptosis of retinal ganglion cells in adult rats. J Neurosci. 14**,** 4368-74.

Bettelli, E., et al., 2003. Myelin oligodendrocyte glycoprotein-specific T cell receptor transgenic mice develop spontaneous autoimmune optic neuritis. J Exp Med. 197**,** 1073-81.

Bickford, M.E., et al., 2015. Retinal and Tectal "Driver-Like" Inputs Converge in the Shell of the Mouse Dorsal Lateral Geniculate Nucleus. J Neurosci. 35**,** 10523-34.

Blakemore, W.F., 1972. Observations on oligodendrocyte degeneration, the resolution of status spongiosus and remyelination in cuprizone intoxication in mice. J Neurocytol. 1**,** 413-26.

Blanco, R., et al., 2014. Functional assessment of the visual pathway with multifocal visual evoked potentials, and their relationship with disability in patients with multiple sclerosis. Mult Scler. 20**,** 183-91.

Blinzinger, K., Kreutzberg, G., 1968. Displacement of synaptic terminals from regenerating motoneurons by microglial cells. Zeitschrift für Zellforschung und Mikroskopische Anatomie. 85**,** 145-157.

Bock, M., et al., 2012. Impairment of contrast visual acuity as a functional correlate of retinal nerve fibre layer thinning and total macular volume reduction in multiple sclerosis. Br J Ophthalmol. 96**,** 62-7.

Bonilha, V.L., 2008. Age and disease-related structural changes in the retinal pigment epithelium. Clinical ophthalmology (Auckland, N.Z.). 2**,** 413-424.

Bostock, H., Sears, T.A., 1978. The internodal axon membrane: electrical excitability and continuous conduction in segmental demyelination. J Physiol. 280**,** 273-301.

Bove, R., Chitnis, T., Houtchens, M., 2014. Menopause in multiple sclerosis: therapeutic considerations. J Neurol. 261**,** 1257-68.

Brambilla, R., et al., 2012. Transgenic inhibition of astroglial NF-kappaB protects from optic nerve damage and retinal ganglion cell loss in experimental optic neuritis. J Neuroinflammation. 9**,** 213.

Brosnan, C.F., et al., 1989. Preliminary studies of cytokine-induced functional effects on the visual pathways in the rabbit. Journal of Neuroimmunology. 25**,** 227-239.

Brown, K.T., 1968. The electroretinogram: Its components and their origins. Vision Research. 8**,** 633-IN6.

Browne, P., et al., 2014. ATLAS OF MULTIPLE SCLEROSIS 2013: A GROWING GLOBAL PROBLEM WITH WIDESPREAD INEQUITY. Neurology. 83**,** 1022-1024.

Bruce-Keller, A.J., et al., 2000. Antiinflammatory effects of estrogen on microglial activation. Endocrinology. 141**,** 3646-56.

Bureau, I., von Saint Paul, F., Svoboda, K., 2006. Interdigitated Paralemniscal and Lemniscal Pathways in the Mouse Barrel Cortex. PLOS Biology. 4**,** e382.

Butovsky, O., et al., 2006. Microglia activated by IL-4 or IFN-gamma differentially induce neurogenesis and oligodendrogenesis from adult stem/progenitor cells. Mol Cell Neurosci. 31**,** 149-60.

Buzzard, T., 1893. Atrophy of the optic nerve as a symptom of chronic disease of the central nervous system. The British Medical Journal. 2**,** 770-784.

Carlton, W.W., 1969. Spongiform encephalopathy induced in rats and guinea pigs by cuprizone. Experimental and Molecular Pathology. 10**,** 274-287.

Carson, M.J., 2002. Microglia as liaisons between the immune and central nervous systems: Functional implications for multiple sclerosis. Glia. 40**,** 218-231.

Castoldi, V., et al., 2019. Non-invasive visual evoked potentials to assess optic nerve involvement in the dark agouti rat model of experimental autoimmune encephalomyelitis induced by myelin oligodendrocyte glycoprotein. Brain Pathol.

Cerciat, M., et al., 2010. Selective estrogen receptor modulators decrease the production of interleukin-6 and interferon-gamma-inducible protein-10 by astrocytes exposed to inflammatory challenge in vitro. Glia. 58**,** 93-102.

Chen, Z., et al., 2012. Lipopolysaccharide-induced microglial activation and neuroprotection against experimental brain injury is independent of hematogenous TLR4. J Neurosci. 32**,** 11706-15.

Chen, Z.H., et al., 2014. Microglial displacement of inhibitory synapses provides neuroprotection in the adult brain. Nature Communications. 5**,** 12.

Chiaravalloti, N.D., DeLuca, J., 2008. Cognitive impairment in multiple sclerosis. Lancet Neurol. 7**,** 1139-51.

Clements, R.J., McDonough, J., Freeman, E.J., 2008. Distribution of parvalbumin and calretinin immunoreactive interneurons in motor cortex from multiple sclerosis post-mortem tissue. Exp Brain Res. 187**,** 459-65.

Coffey, P.J., et al., 1988. Ibotenic acid induced demyelination in the central nervous system: a consequence of a local inflammatory response. Neurosci Lett. 84**,** 178-84.

Confavreux, C., et al., 1998. Rate of pregnancy-related relapse in multiple sclerosis. Pregnancy in Multiple Sclerosis Group. N Engl J Med. 339**,** 285-91.

Constantinople, C.M., Bruno, R.M., 2013. Deep cortical layers are activated directly by thalamus. Science. 340**,** 1591-4.

Corbett, J.J., Chen, J., 2018. Chapter 20 - The Visual System. In: Fundamental Neuroscience for Basic and Clinical Applications (Fifth Edition). Vol., D.E. Haines, G.A. Mihailoff, ed.^eds. Elsevier, pp. 286-305.e1.

Costello, F., 2016. Vision Disturbances in Multiple Sclerosis. Semin Neurol. 36**,** 185-195.

Country, M.W., 2017. Retinal metabolism: A comparative look at energetics in the retina. Brain Research. 1672**,** 50-57.

Coupland, S.G., Kirkham, T.H., 1982. Flash electroretinogram abnormalities in patients with clinically definite multiple sclerosis. Can J Neurol Sci. 9**,** 325-30.

Cowey, A., 1974. Atrophy of Retinal Ganglion Cells after Removal of Striate Cortex in a Rhesus Monkey. Perception. 3**,** 257-260.

Craner, M.J., et al., 2003. Abnormal sodium channel distribution in optic nerve axons in a model of inflammatory demyelination. Brain. 126**,** 1552-1561.

Craner, M.J., et al., 2004. Co-localization of sodium channel Nav1.6 and the sodium–calcium exchanger at sites of axonal injury in the spinal cord in EAE. Brain. 127**,** 294-303.

Crawford, D.K., Mangiardi, M., Tiwari-Woodruff, S.K., 2009a. Assaying the functional effects of demyelination and remyelination: revisiting field potential recordings. J Neurosci Methods. 182**,** 25-33.

Crawford, D.K., et al., 2009b. Functional recovery of callosal axons following demyelination: a critical window. Neuroscience. 164**,** 1407-1421.

Crawford, D.K., et al., 2010. Oestrogen receptor beta ligand: a novel treatment to enhance endogenous functional remyelination. Brain. 133**,** 2999-3016.

Creel, D., 1995a. Visually Evoked Potentials. In: Webvision: The Organization of the Retina and Visual System. Vol., H. Kolb, E. Fernandez, R. Nelson, ed.^eds. University of Utah Health Sciences Center

Copyright: (c) 2019 Webvision., Salt Lake City (UT).

Creel, D.J., 1995b. Visual and Auditory Anomalies Associated with Albinism. In: Webvision: The Organization of the Retina and Visual System. Vol., H. Kolb, E. Fernandez, R. Nelson, ed.^eds. University of Utah Health Sciences Center

Copyright: (c) 2019 Webvision., Salt Lake City (UT).

Cruz-Martin, A., et al., 2014. A dedicated circuit links direction-selective retinal ganglion cells to the primary visual cortex. Nature. 507**,** 358-61.

Curcio, C.A., et al., 2017. Activated Retinal Pigment Epithelium, an Optical Coherence Tomography Biomarker for Progression in Age-Related Macular Degeneration. Invest Ophthalmol Vis Sci. 58**,** Bio211-bio226.

De Angelis, M., et al., 2005. Indazole Estrogens: Highly Selective Ligands for the Estrogen Receptor β. Journal of Medicinal Chemistry. 48**,** 1132-1144.

De Moraes, C.G., 2013. Anatomy of the visual pathways. J Glaucoma. 22 Suppl 5**,** S2-7.

Deguchi, K., et al., 1992. Electrophysiological follow-up of acute and chronic experimental allergic encephalomyelitis in the Lewis rat. Eur Arch Psychiatry Clin Neurosci. 242**,** 1-5.

Delclaux, C., et al., 1996. Role of gelatinase B and elastase in human polymorphonuclear neutrophil migration across basement membrane. Am J Respir Cell Mol Biol. 14**,** 288-95.

Dhande, O.S., Huberman, A.D., 2014. Retinal ganglion cell maps in the brain: implications for visual processing. Curr Opin Neurobiol. 24**,** 133-42.

Diem, R., et al., 2008. Autoimmune optic neuritis in the common marmoset monkey: comparison of visual evoked potentials with MRI and histopathology. Invest Ophthalmol Vis Sci. 49**,** 3707-14.

Dobson, R., Giovannoni, G., 2019. Multiple sclerosis - a review. Eur J Neurol. 26**,** 27-40.

Douglas, R.J., Martin, K.A., 2004. Neuronal circuits of the neocortex. Annu Rev Neurosci. 27**,** 419-51.

Drager, U.C., 1985. Birth dates of retinal ganglion cells giving rise to the crossed and uncrossed optic projections in the mouse. Proc R Soc Lond B Biol Sci. 224**,** 57-77.

Droby, A., et al., 2016. A novel automated segmentation method for retinal layers in OCT images proves retinal degeneration after optic neuritis. Br J Ophthalmol. 100**,** 484-90.

Duarte-Silva, E., et al., 2018. Sildenafil ameliorates EAE by decreasing apoptosis in the spinal cord of C57BL/6 mice. Journal of Neuroimmunology. 321**,** 125-137.

Ebrey, T., Koutalos, Y., 2001. Vertebrate Photoreceptors. Progress in Retinal and Eye Research. 20**,** 49-94.

Eilam, R., et al., 2018. Astrocyte disruption of neurovascular communication is linked to cortical damage in an animal model of multiple sclerosis. Glia. 66**,** 1098-1117.

England, J.D., et al., 1990. Changed distribution of sodium channels along demyelinated axons. Proc Natl Acad Sci U S A. 87**,** 6777-80.

Erskine, L., Herrera, E., 2014. Connecting the retina to the brain. ASN neuro. 6**,** 1759091414562107.

ESIRI, M.M., READING, M.C., 1987. MACROPHAGE POPULATIONS ASSOCIATED WITH MULTIPLE SCLEROSIS PLAQUES. Neuropathology and Applied Neurobiology. 13**,** 451-465.

Evangelou, N., et al., 2001. Size-selective neuronal changes in the anterior optic pathways suggest a differential susceptibility to injury in multiple sclerosis. Brain. 124**,** 1813-20.

Fahey, P.K., Burkhardt, D.A., 2003. Center-surround organization in bipolar cells: symmetry for opposing contrasts. Vis Neurosci. 20**,** 1-10.

Fairless, R., et al., 2012. Preclinical retinal neurodegeneration in a model of multiple sclerosis. J Neurosci. 32**,** 5585-97.

Falco, A., et al., 2014. Reduction in parvalbumin-positive interneurons and inhibitory input in the cortex of mice with experimental autoimmune encephalomyelitis. Exp Brain Res. 232**,** 2439-49.

Feliciano-Sanchez, A., et al., 2019. Development and optimisation of an animal model for the study of ganglion cells in degenerative diseases of the retina and optic nerve. Arch Soc Esp Oftalmol. 94**,** 263-272.

Feng, G., et al., 2000. Imaging neuronal subsets in transgenic mice expressing multiple spectral variants of GFP. Neuron. 28**,** 41-51.

Ferguson, B., et al., 1997. Axonal damage in acute multiple sclerosis lesions. Brain. 120**,** 393-399.

Fisher, J.B., et al., 2006. Relation of visual function to retinal nerve fiber layer thickness in multiple sclerosis. Ophthalmology. 113**,** 324-332.

Fisher, T.G., Alitto, H.J., Usrey, W.M., 2017. Retinal and Nonretinal Contributions to Extraclassical Surround Suppression in the Lateral Geniculate Nucleus. The Journal of Neuroscience. 37**,** 226.

FitzGibbon, T., Nestorovski, Z., 2013. Human intraretinal myelination: axon diameters and axon/myelin thickness ratios. Indian journal of ophthalmology. 61**,** 567-575.

Fitzpatrick, D., 2004. Central Visual Pathways. In: Neuroscience. Sensation and Sensory Processing, Vol., D. Fitzpatrick, ed.^eds. Sinauer Associates, Inc, Massachusetts, pp. 259-282.

Forooghian, F., et al., 2006. Electroretinographic abnormalities in multiple sclerosis: possible role for retinal autoantibodies. Doc Ophthalmol. 113**,** 123-32.

Freund, T.F., Martin, K.A.C., Whitteridge, D., 1985. Innervation of cat visual areas 17 and 18 by physiologically identified X- and Y- type thalamic afferents. I. Arborization patterns and quantitative distribution of postsynaptic elements. Journal of Comparative Neurology. 242**,** 263-274.

G. Waxman, S., 2005. Altered Distributions and Functions of Multiple Sodium Channel Subtypes in Multiple Sclerosis and its Models. Vol., ed.^eds., pp. 101-118.

Gabilondo, I., et al., 2014. Trans-synaptic axonal degeneration in the visual pathway in multiple sclerosis. Ann Neurol. 75**,** 98-107.

Gabilondo, I., et al., 2015. Dynamics of retinal injury after acute optic neuritis. Annals of Neurology. 77**,** 517-528.

Gabilondo, I., et al., 2017. The influence of posterior visual pathway damage on visual information processing speed in multiple sclerosis. Mult Scler. 23**,** 1276-1288.

Gambi, D., Onofrj, M., Di Trapani, G., 1987. Experimental allergic encephalomyelitis, a model of demyelination in central nervous system (CNS). Riv Neurol. 57**,** 27-32.

Gao, H., Hollyfield, J.G., 1992. Aging of the human retina. Differential loss of neurons and retinal pigment epithelial cells. Invest Ophthalmol Vis Sci. 33**,** 1-17.

Garcia-Martin, E., et al., 2017. Retinal and Optic Nerve Degeneration in Patients with Multiple Sclerosis Followed up for 5 Years. Ophthalmology. 124**,** 688-696.

Gelfand, J.M., et al., 2012. Microcystic macular oedema in multiple sclerosis is associated with disease severity. Brain. 135**,** 1786-93.

Georgiev, D., 2011. Photons do collapse in the retina not in the brain cortex: evidence from visual illusions. NeuroQuantology. 9**,** 206-230.

Ghaiad, H.R., et al., 2017. Resveratrol Promotes Remyelination in Cuprizone Model of Multiple Sclerosis: Biochemical and Histological Study. Mol Neurobiol. 54**,** 3219-3229.

Gilbert, C.D., Wiesel, T.N., 1979. Morphology and intracortical projections of functionally characterised neurones in the cat visual cortex. Nature. 280**,** 120-125.

Gilbert, C.D., Wiesel, T.N., 1983. Functional Organization of the Visual Cortex. In: Progress in Brain Research. Vol. 58, J.P. Changeux, J. Glowinski, M. Imbert, F.E. Bloom, ed.^eds. Elsevier, pp. 209-218.

Girolamo, F., et al., 2011. Cerebral cortex demyelination and oligodendrocyte precursor response to experimental autoimmune encephalomyelitis. Neurobiology of Disease. 43**,** 678-689.

Glickfeld, L.L., Olsen, S.R., 2017. Higher-Order Areas of the Mouse Visual Cortex. Annu Rev Vis Sci. 3**,** 251-273.

Gollisch, T., Meister, M., 2010. Eye smarter than scientists believed: neural computations in circuits of the retina. Neuron. 65**,** 150-64.

Gomez, F.P., et al., 2013. Hormone and immune system interactions in demyelinating disease. Horm Behav. 63**,** 315-21.

Graham, E.C., et al., 2016. Progressive Loss of Retinal Ganglion Cells and Axons in Nonoptic Neuritis Eyes in Multiple Sclerosis: A Longitudinal Optical Coherence Tomography Study. Invest Ophthalmol Vis Sci. 57**,** 2311-7.

Graham, S.L., Klistorner, A., 2017. Afferent visual pathways in multiple sclerosis: a review. Clin Exp Ophthalmol. 45**,** 62-72.

Groebe, A., et al., 2009. Cuprizone treatment induces distinct demyelination, astrocytosis, and microglia cell invasion or proliferation in the mouse cerebellum. Cerebellum. 8**,** 163-74.

Gudi, V., et al., 2009. Regional differences between grey and white matter in cuprizone induced demyelination. Brain Res. 1283**,** 127-38.

Gudi, V., et al., 2014. Glial response during cuprizone-induced de- and remyelination in the CNS: lessons learned. Frontiers in cellular neuroscience. 8**,** 73-73.

Hamos, J.E., et al., 1987. Synaptic circuits involving an individual retinogeniculate axon in the cat. Journal of Comparative Neurology. 259**,** 165-192.

Hamurcu, M., et al., 2017. Analysis of multiple sclerosis patients with electrophysiological and structural tests. Int Ophthalmol. 37**,** 649-653.

Hanisch, U.-K., Gertig, U., 2014. Microglial diversity by responses and responders. Frontiers in Cellular Neuroscience. 8**,** 101.

Hanson, J.V.M., et al., 2018. Outer Retinal Dysfunction in the Absence of Structural Abnormalities in Multiple Sclerosis. Invest Ophthalmol Vis Sci. 59**,** 549-560.

Hardingham, G.E., Bading, H., 2003. The Yin and Yang of NMDA receptor signalling. Trends Neurosci. 26**,** 81-9.

Harris, K.D., Mrsic-Flogel, T.D., 2013. Cortical connectivity and sensory coding. Nature. 503**,** 51-8.

Hasselmann, J.P., et al., 2017a. Consistent induction of chronic experimental autoimmune encephalomyelitis in C57BL/6 mice for the longitudinal study of pathology and repair. J Neurosci Methods.

Hasselmann, J.P.C., et al., 2017b. Consistent induction of chronic experimental autoimmune encephalomyelitis in C57BL/6 mice for the longitudinal study of pathology and repair. J Neurosci Methods. 284**,** 71-84.

Hayreh, S.S., et al., 1981. Experimental allergic encephalomyelitis. I. Optic nerve and central nervous system manifestations. Invest Ophthalmol Vis Sci. 21**,** 256-69.

Heesen, C., et al., 2008. Patient perception of bodily functions in multiple sclerosis: gait and visual function are the most valuable. Multiple Sclerosis Journal. 14**,** 988-991.

Hegedus, B., et al., 2009. Optic nerve dysfunction in a mouse model of neurofibromatosis-1 optic glioma. J Neuropathol Exp Neurol. 68**,** 542-51.

Hein, K., et al., 2012. An optical coherence tomography study on degeneration of retinal nerve fiber layer in rats with autoimmune optic neuritis. Invest Ophthalmol Vis Sci. 53.

Henderson, A.P., et al., 2008. An investigation of the retinal nerve fibre layer in progressive multiple sclerosis using optical coherence tomography. Brain. 131**,** 277-87.

Hendrickx, D.A., et al., 2014. Enhanced uptake of multiple sclerosis-derived myelin by THP-1 macrophages and primary human microglia. J Neuroinflammation. 11**,** 64.

Herrera, E., Garcia-Frigola, C., 2008. Genetics and development of the optic chiasm. Front Biosci. 13**,** 1646-53.

Herrera, E., Erskine, L., Morenilla-Palao, C., 2019. Guidance of retinal axons in mammals. Seminars in Cell & Developmental Biology. 85**,** 48-59.

Hiremath, M.M., et al., 1998. Microglial/macrophage accumulation during cuprizone-induced demyelination in C57BL/6 mice. Journal of Neuroimmunology. 92**,** 38-49.

Hiremath, M.M., et al., 2008. MHC class II exacerbates demyelination in vivo independently of T cells. J Neuroimmunol. 203**,** 23-32.

Hobom, M., et al., 2004. Mechanisms and time course of neuronal degeneration in experimental autoimmune encephalomyelitis. Brain Pathol. 14**,** 148-57.

Hoffmann, K., et al., 2008. Epileptic seizures and hippocampal damage after cuprizone-induced demyelination in C57BL/6 mice. Exp Neurol. 210**,** 308-21.

Hood, D.C., Odel, J.G., Winn, B.J., 2003. The multifocal visual evoked potential. J Neuroophthalmol. 23**,** 279-89.

Horstmann, L., et al., 2016. Microglia response in retina and optic nerve in chronic experimental autoimmune encephalomyelitis. Journal of Neuroimmunology. 298**,** 32-41.

Hu, P., et al., 2006. Microvascular and Cellular Responses in the Optic Nerve of Rats with Acute Experimental Allergic Encephalomyelitis (EAE). Brain Pathology. 8**,** 475-486.

Huang, W., et al., 1998. Contribution of supragranular layers to sensory processing and plasticity in adult rat barrel cortex. J Neurophysiol. 80**,** 3261-71.

Huang, X.R., Kong, W., Qiao, J., 2018. Response of the Retinal Nerve Fiber Layer Reflectance and Thickness to Optic Nerve Crush. Invest Ophthalmol Vis Sci. 59**,** 2094-2103.

Hubel, D.H., Wiesel, T.N., 1962. Receptive fields, binocular interaction and functional architecture in the cat's visual cortex. The Journal of physiology. 160**,** 106-154.

Hubel, D.H., Wiesel, T.N., 1974. Uniformity of monkey striate cortex: A parallel relationship between field size, scatter, and magnification factor. Journal of Comparative Neurology. 158**,** 295-305.

Humphrey, A.L., et al., 1985. Projection patterns of individual X- and Y-cell axons from the lateral geniculate nucleus to cortical area 17 in the cat. J Comp Neurol. 233**,** 159-89.

Hunter, S.F., 2016. Overview and diagnosis of multiple sclerosis. Am J Manag Care. 22**,** s141-50.

Imitola, J., Chitnis, T., Khoury, S.J., 2005. Cytokines in multiple sclerosis: from bench to bedside. Pharmacology & Therapeutics. 106**,** 163-177.

Ito, A., et al., 2001. Estrogen treatment down-regulates TNF-alpha production and reduces the severity of experimental autoimmune encephalomyelitis in cytokine knockout mice. J Immunol. 167**,** 542-52.

Jakobs, T.C., et al., 2005. Retinal ganglion cell degeneration is topological but not cell type specific in DBA/2J mice. J Cell Biol. 171**,** 313-25.

Janaky, M., et al., 2017. VEP and PERG in patients with multiple sclerosis, with and without a history of optic neuritis. Doc Ophthalmol. 134**,** 185-193.

Jasse, L., et al., 2013. Persistent visual impairment in multiple sclerosis: prevalence, mechanisms and resulting disability. Mult Scler. 19**,** 1618-26.

Jeon, C.J., Strettoi, E., Masland, R.H., 1998. The major cell populations of the mouse retina. J Neurosci. 18**,** 8936-46.

Jin, J., et al., 2019. Glial pathology and retinal neurotoxicity in the anterior visual pathway in experimental autoimmune encephalomyelitis. Acta Neuropathol Commun. 7**,** 125.

Jindahra, P., Petrie, A., Plant, G.T., 2012. The time course of retrograde trans-synaptic degeneration following occipital lobe damage in humans. Brain. 135**,** 534-541.

Jones, R.E., et al., 1983. Effects of 4-aminopyridine in patients with multiple sclerosis. Journal of the Neurological Sciences. 60**,** 353-362.

Jukkola, P., et al., 2013. Astrocytes differentially respond to inflammatory autoimmune insults and imbalances of neural activity. Acta neuropathologica communications. 1**,** 70-70.

Kanamori, A., et al., 2010a. Superoxide is an associated signal for apoptosis in axonal injury. Brain. 133**,** 2612-25.

Kanamori, A., et al., 2010b. In vivo imaging of retinal ganglion cell axons within the nerve fiber layer. Invest Ophthalmol Vis Sci. 51**,** 2011-8.

Kapoor, R., et al., 2018. Effect of natalizumab on disease progression in secondary progressive multiple sclerosis (ASCEND): a phase 3, randomised, double-blind, placebo-controlled trial with an open-label extension. Lancet Neurol. 17**,** 405-415.

Karim, H., et al., 2018a. Increase in chemokine CXCL1 by ERbeta ligand treatment is a key mediator in promoting axon myelination. Proc Natl Acad Sci U S A.

Karim, H., et al., 2018b. Increase in chemokine CXCL1 by ERbeta ligand treatment is a key mediator in promoting axon myelination. Proc Natl Acad Sci U S A. 115**,** 6291-6296.

Karim, H., et al., 2019a. Analogues of ERbeta ligand chloroindazole exert immunomodulatory and remyelinating effects in a mouse model of multiple sclerosis. Sci Rep. 9**,** 503.

Karim, H., et al., 2019b. Analogues of ERβ ligand chloroindazole exert immunomodulatory and remyelinating effects in a mouse model of multiple sclerosis. Scientific Reports. 9**,** 503.

Kels, B.D., Grzybowski, A., Grant-Kels, J.M., 2015. Human ocular anatomy. Clinics in Dermatology. 33**,** 140-146.

Kempen, G.I., et al., 2012. The impact of low vision on activities of daily living, symptoms of depression, feelings of anxiety and social support in community-living older adults seeking vision rehabilitation services. Qual Life Res. 21**,** 1405-11.

Kerrison, J.B., Flynn, T., Green, W.R., 1994. Retinal pathologic changes in multiple sclerosis. Retina. 14**,** 445-51.

Kerschensteiner, D., Guido, W., 2017. Organization of the dorsal lateral geniculate nucleus in the mouse. Visual neuroscience. 34**,** E008-E008.

Khalaj, A.J., et al., 2013. Estrogen receptor (ER) beta expression in oligodendrocytes is required for attenuation of clinical disease by an ERbeta ligand. Proc Natl Acad Sci U S A. 110**,** 19125-30.

Khalaj, A.J., et al., 2016. Nudging oligodendrocyte intrinsic signaling to remyelinate and repair: Estrogen receptor ligand effects. Journal of Steroid Biochemistry and Molecular Biology. 160**,** 43-52.

Kim, J.H., et al., 2006. Blood-neural barrier: intercellular communication at glio-vascular interface. J Biochem Mol Biol. 39**,** 339-45.

Kim, T.-W., Sung, Y.-H., 2017. Regular exercise promotes memory function and enhances hippocampal neuroplasticity in experimental autoimmune encephalomyelitis mice. Neuroscience. 346**,** 173-181.

Kipp, M., et al., 2007. Oestrogen and progesterone reduce lipopolysaccharide-induced expression of tumour necrosis factor-alpha and interleukin-18 in midbrain astrocytes. J Neuroendocrinol. 19**,** 819-22.

Kipp, M., et al., 2017. Multiple sclerosis animal models: a clinical and histopathological perspective. Brain Pathology. 27**,** 123-137.

Kolb, H., 1995. Simple Anatomy of the Retina. In: Webvision: The Organization of the Retina and Visual System. Vol., H. Kolb, E. Fernandez, R. Nelson, ed.^eds. University of Utah Health Sciences Center

Copyright: (c) 2019 Webvision., Salt Lake City (UT).

Kolb, H., 2003. How the Retina Works: Much of the construction of an image takes place in the retina itself through the use of specialized neural circuits. In: Scientific American. Vol. 91, ed.^eds. Sigma Xi, The Scientific Research Society, North Carolina, pp. 28-35.

Kondo, A., Nakano, T., Suzuki, K., 1987. Blood-brain barrier permeability to horseradish peroxidase in twitcher and cuprizone-intoxicated mice. Brain Res. 425**,** 186-90.

Koutsoudaki, P.N., et al., 2009. Demyelination of the hippocampus is prominent in the cuprizone model. Neurosci Lett. 451**,** 83-8.

Kuchling, J., et al., 2017. Diffusion tensor imaging for multilevel assessment of the visual pathway: possibilities for personalized outcome prediction in autoimmune disorders of the central nervous system. Epma j. 8**,** 279-294.

Kuffler, S.W., 1953. Discharge patterns and functional organization of mammalian retina. J Neurophysiol. 16**,** 37-68.

Kuhlmann, T., et al., 2017. An updated histological classification system for multiple sclerosis lesions. Acta Neuropathol. 133**,** 13-24.

Kumar, S., et al., 2013. Estrogen receptor β ligand therapy activates PI3K/Akt/mTOR signaling in oligodendrocytes and promotes remyelination in a mouse model of multiple sclerosis. Neurobiol Dis. 0**,** 131-44.

Kupfer, C., Chumbley, L., Downer, J.C., 1967. Quantitative histology of optic nerve, optic tract and lateral geniculate nucleus of man. J Anat. 101**,** 393-401.

Kwong, J.M., Caprioli, J., Piri, N., 2010. RNA binding protein with multiple splicing: a new marker for retinal ganglion cells. Invest Ophthalmol Vis Sci. 51**,** 1052-8.

Lambot, M.A., et al., 2005. Mapping labels in the human developing visual system and the evolution of binocular vision. J Neurosci. 25**,** 7232-7.

Lapato, A.S., et al., 2017. Chronic demyelination-induced seizures. Neuroscience. 346**,** 409-422.

Lapato, A.S., Tiwari-Woodruff, S.K., 2018. Connexins and pannexins: At the junction of neuro-glial homeostasis & disease. J Neurosci Res. 96**,** 31-44.

Larabee, C.M., et al., 2016. Loss of Nrf2 exacerbates the visual deficits and optic neuritis elicited by experimental autoimmune encephalomyelitis. Molecular vision. 22**,** 1503-1513.

Laron, M., et al., 2010. Comparison of multifocal visual evoked potential, standard automated perimetry and optical coherence tomography in assessing visual pathway in multiple sclerosis patients. Multiple Sclerosis Journal. 16**,** 412-426.

Li, H., et al., 2013. 17beta-estradiol impedes Bax-involved mitochondrial apoptosis of retinal nerve cells induced by oxidative damage via the phosphatidylinositol 3-kinase/Akt signal pathway. J Mol Neurosci. 50**,** 482-93.

Li, H., et al., 2016. 17beta-Estradiol Protects the Retinal Nerve Cells Suppressing TLR2 Mediated Immune-Inflammation and Apoptosis from Oxidative Stress Insult Independent of PI3K. J Mol Neurosci. 60**,** 195-204.

Lieven, C.J., et al., 2006. Retinal ganglion cell axotomy induces an increase in intracellular superoxide anion. Invest Ophthalmol Vis Sci. 47**,** 1477-85.

Lin, T.-H., et al., 2014. Diffusion fMRI detects white-matter dysfunction in mice with acute optic neuritis. Neurobiology of Disease. 67**,** 1-8.

Lin, T.H., et al., 2017. Diffusion MRI quantifies early axonal loss in the presence of nerve swelling. J Neuroinflammation. 14**,** 78.

Liscic, R.M., Brecelj, J., 2004. Visual evoked potentials in multiple sclerosis patients treated with interferon beta-1a. Croat Med J. 45**,** 323-7.

Livingstone, M., Hubel, D., 1988. SEGREGATION OF FORM, COLOR, MOVEMENT, AND DEPTH - ANATOMY, PHYSIOLOGY, AND PERCEPTION. Science. 240**,** 740-749.

Livingstone, M.S., Hubel, D.H., 1984. Anatomy and physiology of a color system in the primate visual cortex. J Neurosci. 4**,** 309-56.

Lopes Pinheiro, M.A., et al., 2016. Immune cell trafficking across the barriers of the central nervous system in multiple sclerosis and stroke. Biochimica et Biophysica Acta (BBA) - Molecular Basis of Disease. 1862**,** 461-471.

Mabuchi, F., et al., 2003. Optic nerve damage in experimental mouse ocular hypertension. Invest Ophthalmol Vis Sci. 44**,** 4321-30.

Major, Z., et al., 2013. Glatiramer Acetate Treatment-Related Effects on Visual EPs and P300 Wave in Patients Suffering from Multiple Sclerosis, Vol. 45.

Mallon, B.S., et al., 2002. Proteolipid promoter activity distinguishes two populations of NG2-positive cells throughout neonatal cortical development. J Neurosci. 22**,** 876-85.

Mangiardi, M., et al., 2011. An animal model of cortical and callosal pathology in multiple sclerosis. Brain Pathol. 21**,** 263-78.

Manogaran, P., et al., 2016. Optical Coherence Tomography and Magnetic Resonance Imaging in Multiple Sclerosis and Neuromyelitis Optica Spectrum Disorder. International journal of molecular sciences. 17**,** 1894.

Manogaran, P., et al., 2018. Exploring experimental autoimmune optic neuritis using multimodal imaging. NeuroImage. 175**,** 327-339.

Manogaran, P., et al., 2019. Retinal pathology in experimental optic neuritis is characterized by retrograde degeneration and gliosis. Acta Neuropathol Commun. 7**,** 116.

Martin, P.R., 1986. The projection of different retinal ganglion cell classes to the dorsal lateral geniculate nucleus in the hooded rat. Experimental Brain Research. 62**,** 77-88.

Martinez, L.M., Alonso, J.-M., 2003. Complex receptive fields in primary visual cortex. The Neuroscientist : a review journal bringing neurobiology, neurology and psychiatry. 9**,** 317-331.

Masland, R.H., 2011. Cell Populations of the Retina: The Proctor Lecture. Investigative Ophthalmology & Visual Science. 52**,** 4581-4591.

Masland, R.H., 2012. The neuronal organization of the retina. Neuron. 76**,** 266-80.

Matejuk, A., et al., 2001. 17 beta-estradiol inhibits cytokine, chemokine, and chemokine receptor mRNA expression in the central nervous system of female mice with experimental autoimmune encephalomyelitis. J Neurosci Res. 65**,** 529-42.

Matsushima, G.K., Morell, P., 2001. The neurotoxicant, cuprizone, as a model to study demyelination and remyelination in the central nervous system. Brain Pathol. 11**,** 107-16.

May, C.A., Mittag, T., 2006. Optic nerve degeneration in the DBA/2NNia mouse: is the lamina cribrosa important in the development of glaucomatous optic neuropathy? Acta Neuropathol. 111**,** 158-67.

Mazade, R., Alonso, J.M., 2017. Thalamocortical processing in vision. Visual neuroscience. 34**,** E007-E007.

McDonald, W.I., Perry, V.H., Anthony, D.C., 1999. Axon damage and repair in multiple sclerosis. Philosophical Transactions of the Royal Society of London. Series B: Biological Sciences. 354**,** 1641-1647.

McDonald, W.I., et al., 2001. Recommended diagnostic criteria for multiple sclerosis: guidelines from the International Panel on the diagnosis of multiple sclerosis. Ann Neurol. 50**,** 121-7.

Meuth, S.G., et al., 2011. Natalizumab restores evoked potential abnormalities in patients with relapsing-remitting multiple sclerosis. Mult Scler. 17**,** 198-203.

Mey, J., Thanos, S., 1993. Intravitreal injections of neurotrophic factors support the survival of axotomized retinal ganglion cells in adult rats in vivo. Brain Res. 602**,** 304-17.

Meyer, R., et al., 2001. Acute neuronal apoptosis in a rat model of multiple sclerosis. J Neurosci. 21**,** 6214-20.

Mhyre, A.J., Dorsa, D.M., 2006. Estrogen activates rapid signaling in the brain: Role of estrogen receptor α and estrogen receptor β in neurons and glia. Neuroscience. 138**,** 851-858.

Micheva, K.D., et al., 2016. A large fraction of neocortical myelin ensheathes axons of local inhibitory neurons. eLife. 5**,** e15784.

Miller, R.F., Dowling, J.E., 1970. Intracellular responses of the Muller (glial) cells of mudpuppy retina: their relation to b-wave of the electroretinogram. J Neurophysiol. 33**,** 323-41.

Miron, V.E., et al., 2010. Fingolimod (FTY720) enhances remyelination following demyelination of organotypic cerebellar slices. The American journal of pathology. 176**,** 2682-2694.

Miron, V.E., et al., 2013. M2 microglia and macrophages drive oligodendrocyte differentiation during CNS remyelination. Nature Neuroscience. 16**,** 1211.

Miron, V.E., 2017. Microglia-driven regulation of oligodendrocyte lineage cells, myelination, and remyelination. J Leukoc Biol. 101**,** 1103-1108.

Miyake, E., Imagawa, T., Uehara, M., 2004. Fine structure of the retino-optic nerve junction in dogs. J Vet Med Sci. 66**,** 1549-54.

Monsalve, P., et al., 2018. Retinal ganglion cell function in recovered optic neuritis: Faster is not better. Clin Neurophysiol. 129**,** 1813-1818.

Moore, S.M., et al., 2014a. Multiple functional therapeutic effects of the estrogen receptor beta agonist indazole-Cl in a mouse model of multiple sclerosis. Proc Natl Acad Sci U S A. 111**,** 18061-6.

Moore, S.M., et al., 2014b. Multiple functional therapeutic effects of the estrogen receptor beta agonist indazole-Cl in a mouse model of multiple sclerosis. Proceedings of the National Academy of Sciences of the United States of America. 111**,** 18061-18066.

Morell, P., et al., 1998. Gene expression in brain during cuprizone-induced demyelination and remyelination. Mol Cell Neurosci. 12**,** 220-7.

Morizawa, Y.M., et al., 2017. Reactive astrocytes function as phagocytes after brain ischemia via ABCA1-mediated pathway. Nat Commun. 8**,** 28.

Mowry, E.M., et al., 2009. Vision related quality of life in multiple sclerosis: correlation with new measures of low and high contrast letter acuity. J Neurol Neurosurg Psychiatry. 80**,** 767-72.

Munaut, C., et al., 2001. Presence of oestrogen receptor type beta in human retina. Br J Ophthalmol. 85**,** 877-82.

Nagata, A., et al., 2009. In vivo quantitative evaluation of the rat retinal nerve fiber layer with optical coherence tomography. Invest Ophthalmol Vis Sci. 50**,** 2809-15.

Nakazawa, T., Takahashi, H., Shimura, M., 2006. Estrogen has a neuroprotective effect on axotomized RGCs through ERK signal transduction pathway. Brain Res. 1093**,** 141-9.

Namekata, K., et al., 2014. Dock3 protects myelin in the cuprizone model for demyelination. Cell Death & Disease. 5**,** e1395.

National Academies of Sciences, E., et al., 2016. The Impact of Vision Loss. In: Making Eye Health a Population Health Imperative: Vision for Tomorrow. Vol., A. Welp, R.B. Woodbury, M.A. McCoy, S.M. Teutsch, ed.^eds. National Academies Press (US)

Copyright 2016 by the National Academy of Sciences. All rights reserved., Washington (DC), pp. 135-162.

Nerrant, E., Tilikete, C., 2017. Ocular Motor Manifestations of Multiple Sclerosis. J Neuroophthalmol. 37**,** 332-340.

Nikic, I., et al., 2011. A reversible form of axon damage in experimental autoimmune encephalomyelitis and multiple sclerosis. Nat Med. 17**,** 495-9.

Nilsson, S., Gustafsson, J.A., 2011. Estrogen receptors: therapies targeted to receptor subtypes. Clin Pharmacol Ther. 89**,** 44-55.

Nishioka, C., et al., 2017. Disease stage-dependent relationship between diffusion tensor imaging and electrophysiology of the visual system in a murine model of multiple sclerosis. Neuroradiology. 59**,** 1241-1250.

Nishioka, C., et al., 2019. Sequential phases of RGC axonal and somatic injury in EAE mice examined using DTI and OCT. Multiple Sclerosis and Related Disorders. 27**,** 315-323.

Njenga, M.K., et al., 2000. Short-term treatment with interferon-alpha/beta promotes remyelination, whereas long-term treatment aggravates demyelination in a murine model of multiple sclerosis. J Neurosci Res. 59**,** 661-70.

Norkute, A., et al., 2009. Cuprizone treatment induces demyelination and astrocytosis in the mouse hippocampus. J Neurosci Res. 87**,** 1343-55.

Oakden, W., et al., 2017. Early regional cuprizone-induced demyelination in a rat model revealed with MRI. NMR Biomed. 30.

Olabarria, M., Goldman, J.E., 2017. Disorders of Astrocytes: Alexander Disease as a Model. Annual Review of Pathology: Mechanisms of Disease. 12**,** 131-152.

Omari, K.M., et al., 2009. Neuroprotection and remyelination after autoimmune demyelination in mice that inducibly overexpress CXCL1. Am J Pathol. 174**,** 164-76.

Ontaneda, D., et al., 2017. Progressive multiple sclerosis: prospects for disease therapy, repair, and restoration of function. The Lancet. 389**,** 1357-1366.

Ortiz-Perez, S., et al., 2016. Visual field impairment captures disease burden in multiple sclerosis. J Neurol. 263**,** 695-702.

Ozaki, H., et al., 2000. Blockade of vascular endothelial cell growth factor receptor signaling is sufficient to completely prevent retinal neovascularization. Am J Pathol. 156**,** 697-707.

Pakrou, N., et al., 2006. Multifocal objective perimetry compared with Humphrey full-threshold perimetry in patients with optic neuritis. Clinical & Experimental Ophthalmology. 34**,** 562-567.

Pang, Y., et al., 2013. Differential roles of astrocyte and microglia in supporting oligodendrocyte development and myelination in vitro. Brain and behavior. 3**,** 503-514.

Panitch, H., et al., 2004. Interferon beta-1b in secondary progressive MS: results from a 3-year controlled study. Neurology. 63**,** 1788-95.

Papadopoulou, A., et al., 2019. Damage of the lateral geniculate nucleus in MS: Assessing the missing node of the visual pathway. Neurology. 92**,** e2240-e2249.

Papakostopoulos, D., et al., 1989. The electroretinogram in multiple sclerosis and demyelinating optic neuritis. Electroencephalogr Clin Neurophysiol. 74**,** 1-10.

Pastare, D., et al., 2013. Evaluation of axonal optic nerve damage using visual evoked potentials and optical coherence tomography in patients with multiple sclerosis. Medicina (Kaunas). 49**,** 474-8.

Paxinos, G., Franklin, K.B.J., 2013. Paxinos and Franklin's The Mouse Brain in Stereotaxic Coordinates, Vol., Elsevier, London, UK.

Penfold, P.L., et al., 2001. Immunological and Aetiological Aspects of Macular Degeneration. Progress in Retinal and Eye Research. 20**,** 385-414.

Perez de Sevilla Muller, L., et al., 2014. Melanopsin ganglion cells are the most resistant retinal ganglion cell type to axonal injury in the rat retina. PLoS One. 9**,** e93274.

Perlman, I., 1995. The Electroretinogram: ERG. In: Webvision: The Organization of the Retina and Visual System. Vol., H. Kolb, E. Fernandez, R. Nelson, ed.^eds. University of Utah Health Sciences Center

Copyright: (c) 2019 Webvision., Salt Lake City (UT).

Petracca, M., et al., 2017. Retinal degeneration in primary-progressive multiple sclerosis: A role for cortical lesions? Mult Scler. 23**,** 43-50.

Pfrieger, F.W., Barres, B.A., 1996. New views on synapse—glia interactions. Current Opinion in Neurobiology. 6**,** 615-621.

Pihl-Jensen, G., Schmidt, M.F., Frederiksen, J.L., 2017. Multifocal visual evoked potentials in optic neuritis and multiple sclerosis: A review. Clin Neurophysiol. 128**,** 1234-1245.

Porrero, C., et al., 2010. Mapping of fluorescent protein-expressing neurons and axon pathways in adult and developing Thy1-eYFP-H transgenic mice. Brain Research. 1345**,** 59-72.

Poser, C.M., Brinar, V.V., 2004. Diagnostic criteria for multiple sclerosis: an historical review. Clin Neurol Neurosurg. 106**,** 147-58.

Pott, F., et al., 2009. Cuprizone effect on myelination, astrogliosis and microglia attraction in the mouse basal ganglia. Brain Research. 1305**,** 137-149.

Potter, L.E., et al., 2016. Altered excitatory-inhibitory balance within somatosensory cortex is associated with enhanced plasticity and pain sensitivity in a mouse model of multiple sclerosis. J Neuroinflammation. 13**,** 142.

Prineas, J.W., et al., 2001. Immunopathology of secondary-progressive multiple sclerosis. Ann Neurol. 50**,** 646-57.

Prokai-Tatrai, K., et al., 2013. 17beta-estradiol eye drops protect the retinal ganglion cell layer and preserve visual function in an in vivo model of glaucoma. Mol Pharm. 10**,** 3253-61.

Pula, J.H., Reder, A.T., 2009. Multiple sclerosis. Part I: neuro-ophthalmic manifestations. Curr Opin Ophthalmol. 20**,** 467-75.

Quiquempoix, M., et al., 2018. Layer 2/3 Pyramidal Neurons Control the Gain of Cortical Output. Cell Reports. 24**,** 2799-2807.e4.

Ransohoff, R.M., Brown, M.A., 2012. Innate immunity in the central nervous system. The Journal of Clinical Investigation. 122**,** 1164-1171.

Rasmussen, S., et al., 2007. Persistent activation of microglia is associated with neuronal dysfunction of callosal projecting pathways and multiple sclerosis-like lesions in relapsing--remitting experimental autoimmune encephalomyelitis. Brain. 130**,** 2816-29.

Raymond, I.D., et al., 2008. Cyan fluorescent protein expression in ganglion and amacrine cells in a thy1-CFP transgenic mouse retina. Molecular Vision. 14**,** 1559-1574.

Reese, B.E., Jeffery, G., 1983. Crossed and uncrossed visual topography in dorsal lateral geniculate nucleus of the pigmented rat. J Neurophysiol. 49**,** 877-85.

Reichenbach, A., et al., 1988. Ultrastructure of rabbit retinal nerve fibre layer--neuro-glial relationships, myelination, and nerve fibre spectrum. J Hirnforsch. 29**,** 481-91.

Ridder Iii, W.H., Nusinowitz, S., 2006. The visual evoked potential in the mouse—Origins and response characteristics. Vision Research. 46**,** 902-913.

Rodriguez-Mena, D., et al., 2013. Electropysiologic Evaluation of the Visual Pathway in Patients With Multiple Sclerosis. Journal of Clinical Neurophysiology. 30.

Rodriguez, A.R., de Sevilla Muller, L.P., Brecha, N.C., 2014. The RNA binding protein RBPMS is a selective marker of ganglion cells in the mammalian retina. J Comp Neurol. 522**,** 1411-43.

Rompani, S.B., et al., 2017. Different Modes of Visual Integration in the Lateral Geniculate Nucleus Revealed by Single-Cell-Initiated Transsynaptic Tracing. Neuron. 93**,** 767-776.e6.

Roodhooft, J.M., 2009. Ocular problems in early stages of multiple sclerosis. Bull Soc Belge Ophtalmol. 65-8.

Ruck, T., et al., 2015. Alemtuzumab in Multiple Sclerosis: Mechanism of Action and Beyond. International journal of molecular sciences. 16**,** 16414-16439.

Russo, R., et al., 2008. 17Beta-estradiol prevents retinal ganglion cell loss induced by acute rise of intraocular pressure in rat. Prog Brain Res. 173**,** 583-90.

Saidha, S., et al., 2011a. Visual dysfunction in multiple sclerosis correlates better with optical coherence tomography derived estimates of macular ganglion cell layer thickness than peripapillary retinal nerve fiber layer thickness. Multiple Sclerosis Journal. 17**,** 1449-1463.

Saidha, S., et al., 2011b. Primary retinal pathology in multiple sclerosis as detected by optical coherence tomography. Brain. 134**,** 518-533.

Saijo, K., et al., 2011. An ADIOL-ERbeta-CtBP transrepression pathway negatively regulates microglia-mediated inflammation. Cell. 145**,** 584-95.

Sanes, J.R., Masland, R.H., 2015. The types of retinal ganglion cells: current status and implications for neuronal classification. Annu Rev Neurosci. 38**,** 221-46.

Schultz, V., et al., 2017. Acutely damaged axons are remyelinated in multiple sclerosis and experimental models of demyelination. Glia. 65**,** 1350-1360.

Schulz, J.M., et al., 2009. Short-latency activation of striatal spiny neurons via subcortical visual pathways. J Neurosci. 29**,** 6336-47.

Schwark, H.D., et al., 1986. Cat area 17. II. Response properties of infragranular layer neurons in the absence of supragranular layer activity. J Neurophysiol. 56**,** 1074-87.

Seabrook, T.A., et al., 2017. Architecture, Function, and Assembly of the Mouse Visual System. Annual Review of Neuroscience. 40**,** 499-538.

Seigo, M.A., et al., 2012. In vivo assessment of retinal neuronal layers in multiple sclerosis with manual and automated optical coherence tomography segmentation techniques. Journal of Neurology. 259**,** 2119-2130.

Sepulcre, J., et al., 2009. Contribution of white matter lesions to gray matter atrophy in multiple sclerosis: evidence from voxel-based analysis of T1 lesions in the visual pathway. Arch Neurol. 66**,** 173-9.

Shao, H., et al., 2004. Myelin/Oligodendrocyte Glycoprotein–Specific T-Cells Induce Severe Optic Neuritis in the C57Bl/6 Mouse. Investigative Ophthalmology & Visual Science. 45**,** 4060-4065.

Shen, T., et al., 2019. Differing Structural and Functional Patterns of Optic Nerve Damage in Multiple Sclerosis and Neuromyelitis Optica Spectrum Disorder. Ophthalmology. 126**,** 445-453.

Shindler, K.S., et al., 2006. Retinal ganglion cell loss induced by acute optic neuritis in a relapsing model of multiple sclerosis. Mult Scler. 12**,** 526-32.

Shindler, K.S., et al., 2008. Inflammatory demyelination induces axonal injury and retinal ganglion cell apoptosis in experimental optic neuritis. Exp Eye Res. 87**,** 208-13.

Shughrue, P.J., Lane, M.V., Merchenthaler, I., 1997. Comparative distribution of estrogen receptor-α and -β mRNA in the rat central nervous system. Journal of Comparative Neurology. 388**,** 507-525.

Silvestroff, L., et al., 2012. Cuprizone-induced demyelination in the rat cerebral cortex and thyroid hormone effects on cortical remyelination. Exp Neurol. 235**,** 357-67.

Skripuletz, T., et al., 2008. Cortical demyelination is prominent in the murine cuprizone model and is strain-dependent. The American journal of pathology. 172**,** 1053-1061.

Skripuletz, T., et al., 2010. Cerebellar Cortical Demyelination in the Murine Cuprizone Model. Brain Pathology. 20**,** 301-312.

Skripuletz, T., et al., 2013. Astrocytes regulate myelin clearance through recruitment of microglia during cuprizone-induced demyelination. Brain. 136**,** 147-67.

Smith, B.J., et al., 2014. Contribution of retinal ganglion cells to the mouse electroretinogram. Doc Ophthalmol. 128**,** 155-68.

Smith, J.A., et al., 2011. Estrogen or estrogen receptor agonist inhibits lipopolysaccharide induced microglial activation and death. Neurochem Res. 36**,** 1587-93.

Smith, K.J., McDonald, W.I., 1999. The pathophysiology of multiple sclerosis: the mechanisms underlying the production of symptoms and the natural history of the disease. Philos Trans R Soc Lond B Biol Sci. 354**,** 1649-73.

Smith, M.E., 1999. Phagocytosis of myelin in demyelinative disease: a review. Neurochem Res. 24**,** 261-8.

Smith, R., Studd, J.W., 1992. A pilot study of the effect upon multiple sclerosis of the menopause, hormone replacement therapy and the menstrual cycle. J R Soc Med. 85**,** 612-3.

Soares, R.M.G., et al., 2013. Optical neuritis induced by different concentrations of myelin oligodendrocyte glycoprotein presents different profiles of the inflammatory process. Autoimmunity. 46**,** 480-485.

Sofroniew, M.V., 2009. Molecular dissection of reactive astrogliosis and glial scar formation. Trends in neurosciences. 32**,** 638-647.

Solomon, A.J., Corboy, J.R., 2017. The tension between early diagnosis and misdiagnosis of multiple sclerosis. Nature Reviews Neurology. 13**,** 567.

Soto, I., et al., 2008. Retinal ganglion cells downregulate gene expression and lose their axons within the optic nerve head in a mouse glaucoma model. J Neurosci. 28**,** 548-61.

Spector, R.H. (Ed.) 1990. Chapter 116. Visual Fields. Butterworths, Boston.

Steelman, A.J., Thompson, J.P., Li, J., 2012. Demyelination and remyelination in anatomically distinct regions of the corpus callosum following cuprizone intoxication. Neurosci Res. 72**,** 32-42.

Stojic, A., et al., 2019. Preclinical stress originates in the rat optic nerve head during development of autoimmune optic neuritis. Glia. 67**,** 512-524.

Stone, J., et al., 1995. Development of retinal vasculature is mediated by hypoxia-induced vascular endothelial growth factor (VEGF) expression by neuroglia. J Neurosci. 15**,** 4738-47.

Strauss, O., 2005. The retinal pigment epithelium in visual function. Physiol Rev. 85**,** 845-81.

Subei, A.M., Eggenberger, E., 2012. Efferent manifestations of multiple sclerosis. Curr Opin Ophthalmol. 23**,** 506-9.

Sui, Y., et al., 2006. CXCL10-induced cell death in neurons: role of calcium dysregulation. Eur J Neurosci. 23**,** 957-64.

Sun, D., et al., 2009. The morphology and spatial arrangement of astrocytes in the optic nerve head of the mouse. The Journal of comparative neurology. 516**,** 1-19.

Tang, Y., Le, W., 2016. Differential Roles of M1 and M2 Microglia in Neurodegenerative Diseases. Molecular Neurobiology. 53**,** 1181-1194.

Tansey, E.M., Allen, T.G.J., Ikeda, H., 1986. ENHANCED RETINAL AND OPTIC NERVE EXCITABILITY ASSOCIATED WITH DEMYELINATION IN MICE INFECTED WITH SEMLIKI FOREST VIRUS. Brain. 109**,** 15-30.

Thomas, D.B., 1984. Do hormones cause breast cancer? Cancer. 53**,** 595-604.

Tirotta, E., Ransohoff, R.M., Lane, T.E., 2011. CXCR2 signaling protects oligodendrocyte progenitor cells from IFN-γ/CXCL10-mediated apoptosis. Glia. 59**,** 1518-1528.

Tiwari-Woodruff, S., Voskuhl, R.R., 2009. Neuroprotective and anti-inflammatory effects of estrogen receptor ligand treatment in mice. J Neurol Sci. 286**,** 81-5.

Tomassy, G.S., et al., 2014. Distinct profiles of myelin distribution along single axons of pyramidal neurons in the neocortex. Science. 344**,** 319-24.

Toosy, A.T., Mason, D.F., Miller, D.H., 2014. Optic neuritis. The Lancet Neurology. 13**,** 83-99.

Ts'o, D.Y., Zarella, M., Burkitt, G., 2009. Whither the hypercolumn? The Journal of Physiology. 587**,** 2791-2805.

Usrey, W.M., Alitto, H.J., 2015. Visual Functions of the Thalamus. Annual Review of Vision Science. 1**,** 351-371.

V. Kolesnikov, A., G. Kisselev, O., Kefalov, V., 2014. Signaling by Rod and Cone Photoreceptors: Opsin Properties, G-protein Assembly, and Mechanisms of Activation. Vol., ed.^eds., pp. 23-48.

Vecino, E., et al., 2016. Glia-neuron interactions in the mammalian retina. Prog Retin Eye Res. 51**,** 1-40.

Villoslada, P., et al., 2012. Color vision is strongly associated with retinal thinning in multiple sclerosis. Mult Scler. 18**,** 991-9.

Volpe, N.J., 2008. The Optic Neuritis Treatment Trial: A Definitive Answer and Profound Impact With Unexpected Results. JAMA Ophthalmology. 126**,** 996-999.

Vukusic, S., et al., 2004. Pregnancy and multiple sclerosis (the PRIMS study): clinical predictors of post-partum relapse. Brain. 127**,** 1353-60.

Walter, S.D., et al., 2012. Ganglion cell loss in relation to visual disability in multiple sclerosis. Ophthalmology. 119**,** 1250-7.

Wang, S., et al., 2015. 17beta-estradiol ameliorates light-induced retinal damage in Sprague-Dawley rats by reducing oxidative stress. J Mol Neurosci. 55**,** 141-151.

Whitacre, C.C., 2001. Sex differences in autoimmune disease. Nat Immunol. 2**,** 777-80.

Wilks, T.A., Harvey, A.R., Rodger, J., 2013. Seeing with Two Eyes: Integration of Binocular Retinal projections in the Brain. In: Functional Brain Mapping and the Endeavor to Understand the Working Brain. Vol., F. Signorelli, D. Chirchiglia, ed.^eds. IntechOpen.

Wolinsky, J.S., et al., 2007. Glatiramer acetate in primary progressive multiple sclerosis: results of a multinational, multicenter, double-blind, placebo-controlled trial. Ann Neurol. 61**,** 14-24.

Wood, K.C., Blackwell, J.M., Geffen, M.N., 2017. Cortical inhibitory interneurons control sensory processing. Current opinion in neurobiology. 46**,** 200-207.

Yamate-Morgan, H., et al., 2019. Functional Effects of Cuprizone-Induced Demyelination in the Presence of the mTOR-Inhibitor Rapamycin. Neuroscience. 406**,** 667-683.

You, Y., et al., 2011. Latency delay of visual evoked potential is a real measurement of demyelination in a rat model of optic neuritis. Invest Ophthalmol Vis Sci. 52**,** 6911-8.

You, Y., et al., 2012. Anterograde Degeneration along the Visual Pathway after Optic Nerve Injury. PLOS ONE. 7**,** e52061.

You, Y., et al., 2015. Visual Evoked Potential Recording in a Rat Model of Experimental Optic Nerve Demyelination. J Vis Exp. e52934.

You, Y., et al., 2019. Demyelination precedes axonal loss in the transneuronal spread of human neurodegenerative disease. Brain. 142**,** 426-442.

Young, B., Eggenberger, E., Kaufman, D., 2012. Current electrophysiology in ophthalmology: a review. Curr Opin Ophthalmol. 23**,** 497-505.

Yu, M., et al., 2011. Visual abnormalities associated with enhanced optic nerve myelination. Brain research. 1374**,** 36-42.

Yuan, L., Neufeld, A.H., 2001. Activated microglia in the human glaucomatous optic nerve head. J Neurosci Res. 64**,** 523-32.

Zhang, X., Cheng, M., Chintala, S.K., 2004. Kainic Acid–Mediated Upregulation of Matrix Metalloproteinase-9 Promotes Retinal Degeneration. Investigative Ophthalmology & Visual Science. 45**,** 2374-2383.

Zhu, Y., et al., 2015. Control of response reliability by parvalbumin-expressing interneurons in visual cortex. Nature Communications. 6**,** 6802.

Ziehn, M.O., et al., 2010. Hippocampal CA1 atrophy and synaptic loss during experimental autoimmune encephalomyelitis, EAE. Laboratory Investigation. 90**,** 774-786.